# Improved Dosimetry for $^{90}$Y Microsphere Treatments of Liver Malignancies

by

Adam B. Paxton

A dissertation submitted in partial fulfillment of
the requirements for the degree of

Doctor of Philosophy

(Medical Physics)

at the

University of Wisconsin-Madison

2012

Date of final oral examination: 06/01/12

This dissertation is approved by the following members of the Final Oral Committee:
Larry A. DeWerd, Professor, Medical Physics
Robert J. Nickles, Professor, Medical Physics
Bruce R. Thomadsen, Professor, Medical Physics
Robert Jeraj, Associate Professor, Medical Physics
Mark A. Ritter, Professor, Human Oncology

*To Mom and Dad.*

*Wow! Thanks for everything!*

# Abstract

Yttrium-90 ($^{90}$Y) microspheres are used for the treatment of non-resectable liver cancer. The treatment has shown promising results, including the potential to downgrade the disease state to resectable. However, there is presently no U.S. national standard measurement device used for the determination of $^{90}$Y microsphere activity.

A coincidence detection system (CDS) was developed to spectroscopically assay the activity of $^{90}$Y microspheres by detecting the coincident 511 keV annihilation photons present in a $^{90}$Y photon spectrum due to the internal pair production component of $^{90}$Y decay. The CDS paired a HPGe detector with a large NaI detector. A method for correcting for counting losses that utilized a series of pulse generators was implemented into the CDS and validated. The geometric sensitivity of the CDS was characterized, and the system was shown to be able to accurately determine the activity of $^{90}$Y sources. The system was used to determine the activity of a sample of resin $^{90}$Y microspheres.

Two well-type ionization chambers were characterized for their response to $^{90}$Y sources to investigate their use for the clinical determination of $^{90}$Y microspheres activity. The activity preparation methods used with the resin $^{90}$Y microspheres were investigated, and the effects of the volume dependencies of the ionization chambers on the activity delivered were analyzed. Based the results of the analysis, recommendations for measurement geometries that provided more accurate activity determinations were suggested.

The effects of the microsphere and surrounding material on the $^{90}$Y dose kernel were studied with Monte Carlo transport codes MCNP5 and EGSnrc. The microsphere material was found to have little effect on the dose kernel, but the density of the surrounding material was found to greatly affect the calculated dose kernel.

The developed CDS was shown to be a possible standard activity measurement device for $^{90}$Y microspheres. This work determined that well-type ionization chambers could be calibrated using sources whose activities had been determined with the CDS, for the accurate determination of $^{90}$Y microsphere activity in a clinical setting. Establishing a calibration service based on this work would help reduce the uncertainty in the dosimetry associated with the $^{90}$Y microsphere treatment.

# Acknowledgements

There are so many people who have contributed to this project as well as my life during my time here in Madison. I want to take this opportunity to thank as many as I can who have helped me along the way. It seems fitting that I first thank my advisor Larry DeWerd, who started me on this journey when he offered me a position as his student in the Cal Lab. Larry provides all of his students with encouragement, encyclopedic knowledge of the field of metrology, and an open door, but also challenges his students to think for themselves and learn how to become effective researchers. For me, Larry has been source of invaluable guidance. I want to thank Larry for giving me the opportunity to be a part of an amazing group of people from whom I have learned an immense amount.

I can honestly say that every staff member of the Cal Lab has helped me in some fashion. I can literally count the fingers (10) I owe to Ben Palmer's guidance in the machining of research equipment, and he has also been instrumental in the annual organization of the lab's March Madness bracket contest. Denise Roche has always been extremely helpful when making purchases for the lab and organizing travel arrangements. The logistics of the lab run much smoother with her help. I want to thank Keith Kunugi for all of the computing support and for handling the various business dealings with the $^{90}$Y microsphere manufacturers, a headache I am glad I did not have to endure. Wendy Kennan helped immensely in acquiring various sources that were required for my research and protected me from said sources (and occasionally myself) by dressing me from head to toe in PPE. Anna Barber has been

amazing at making sure I promptly receive any ordered equipment or sources. Thanks to the other Ben (Rosen) for the various discussions about the details of electrometer land. Also, thanks to the king of electrometer land, Frank Grenzow, for help troubleshooting all things electronic and demonstrating the correct method for making cables, which was shown to be more effective than the Paxton method. I have enjoyed a number of morning conversations with Steve Bazan about any random topic ranging from the weather to family dynamics. I owe a lot to Dan Anderson's construction, administration, and troubleshooting of the student computing resources. I think we sometimes took for granted how good we had it in this regard, and I learned a lot being a disseminator of computing information to fellow students. Thanks to Cliff Hammer for placing my numerous orders for liquid nitrogen and for the great conversations that always seemed to verge on solving the world's problems, but inevitably degraded into talking about our favorite television shows. Last, but not least, thanks to John Micka for the technical guidance, humor, and passion for the lab. I very much appreciated his advocacy for the students and his insight on all research topics.

This project would not have been possible without the support of Jerry Nickles and the UW Cyclotron gang, who essentially gave me a library card to check out any number of NIM electronics from their vast collection as well as providing the NaI detector for coincidence detection system. I appreciate Jerry letting me run with his original idea for the coincidence detection system and for all of the technical guidance with getting the system up and running.

Paul DeLuca also provided a number of key pieces of equipment that became part of the coincidence detection system, for which I am very appreciative. Whether he remembers me borrowing this equipment or not, he should be comforted to know that all borrowed equipment remains intact and operational. I took it upon myself to replace the "DeLuca"

that was originally on his equipment with "UW Cyclotron", so should he ever need his equipment back, he will know where to find it.

Many thanks to Reed Selwyn for springboarding me into this project with his great initial work with $^{90}$Y microspheres, including the development of an image-based dosimetry for the treatment. The discussions with Reed over the course of this project have been invaluable and enabled me to see the big picture with regard to the $^{90}$Y microsphere treatment.

I want to thank Bruce Thomadsen for allowing me to tag along to a number of $^{90}$Y microsphere procedures. After spending so much time working in the lab and reading papers, it was nice to put everything into perspective and see the realities of the procedure.

Thanks to the first author of the AAPM Task Group 144 report, Andy Dezarn, for letting me be a fly-on-the-wall during the revision process of the group's manuscript. Being able to witness the process taught me a lot about group dynamics and the revision process, as well as gave me the opportunity to further my knowledge on all aspects of $^{90}$Y microsphere treatments.

Thank you to Scott Knishka from the UW Hospital Nuclear Medicine department for help in ordering the SIR-Spheres sample used in this work and for letting me have extra vials from his collection for my research. Thank you also to Scott's student Joe Vande Burgt, who pestered Sirtex repeatedly for information on my behalf.

Steve Davis is a Monte Carlo guru. I thank him for many insightful discussions regarding both Monte Carlo and medical physics in general. His attention to detail is unparalleled, and I appreciate him helping me become a better researcher.

Outside of research, I also want to thank the physicists from Turville Bay, Sean Frigo and Frank Goodin, for allowing me to complete a clinical internship with them. The experience cemented my desire to pursue a career as a clinical medical physicist, but also helped give perspective to the research I was conducting.

Thanks to all of the Cal Lab students throughout my time here. I am so happy that I had the opportunity to join a lab with an amazing group of peers. Special thanks to the students in my same year: Julie Raffi, Tina Pike, and Jackie Moga. Thanks for all of the support and encouragement during our time together. You three have been great friends and confidants. I appreciate everything except the attempt to forcibly apply makeup on me. Additional thanks to Jessie Snow, Regina Fulkerson, Stephanie Junell, Laura Bartol, Qing Liang, Tina Pike, and Martha Malin for providing comments and edits on this thesis.

During my time in Madison, I have had the opportunity to be involved in groups of medical physics students in non-medical physics activities. These included the softball team, Annihilation in Flight, the pub trivia team, Betty White Lightning, and the social club, the Wolf Pack. Thanks to friends: Matt Nyflot, Charlie Wallace, Dave Barbee, Dave Westerly, Benny Titz, Ryan Flynn, Pat Hill, Ted Fisher, Jalalieh Morrow, Jessica Klaers, Karl Rasmussen, Leah Schubert, Alonso Gutierrez, Liz Zakszewski, Bill Andrews, Adam Uselmann, Stephanie Junell, Laura Bartol, Jessie Snow, Kibo Nam, Lindsay Jones, Jess Fagerstrom, Steve Davis, Todd Meyers, Katie and Cyrus Naheedy, and everyone else (sorry if I missed you). It has been great.

I can honestly say I would not be here without my parents, Brent and Patti Paxton. Their constant emotional support has helped me get through a lot and their great senses of humor have always kept me amused. I appreciate them letting me find my own way, but always being willing to offer advice when asked. You two are awesome, thank you so much. Also thanks to my brother Ben for always keeping me entertained with his adventures and being a great compadre.

During my time in Madison, I was lucky enough to meet my amazing lady friend, Julie Page. It has been incredible to share the grad school adventure with someone who has a different perspective (as she is studying piano performance), a passion for what she does,

and is genuinely a wonderful person. I have loved all of the exciting (and non-exciting) time we have spent together and I look forward to many more adventures with you in the future.

# Contents

# List of Figures

# List of Tables

# Chapter 1

# Introduction

## 1.1 Overview

The use of yttrium-90 ($^{90}$Y) microspheres for the treatment of non-resectable liver cancer has shown promising results. These include an improved survival rate [Gray et al., 2001, Sharma et al., 2007, Sato et al., 2008], improved quality of life [Steel et al., 2004], and the potential to downgrade the disease state to resectable [Lau et al., 1998]. The treatment takes advantage of the unique blood supply of liver tumors, which receive 80 % of their blood from the hepatic artery and 20 % of their blood from the portal vein, by injecting the $^{90}$Y microsphere directly into the hepatic artery. Since normal liver tissue receives 80 % of its blood from the portal vein and 20 % from the hepatic artery [Breedis and Young, 1954], this treatment preferentially delivers the dose from the $^{90}$Y to liver tumors.

A primary activity standard for $^{90}$Y microspheres has not been developed in the U.S. This lack of standard and non-standardized clinical measurement techniques can lead to errors of up to 50 % in the clinically-measured activity of $^{90}$Y sources [Wastiel et al., 2005]. Present dosimetry methods used to evaluate the dose delivered by $^{90}$Y microspheres either assume a uniform activity distribution of the microspheres within the liver [Sarfaraz et al., 2003], which has been shown to be inaccurate [Campbell et al., 2000], or use pre-treatment

imaging surrogates to estimate the distribution of the $^{90}$Y microspheres within the patient [Sarfaraz et al., 2004]. It has been suggested, however, that these surrogates poorly mimic the actual distribution of the microspheres within the patient [Selwyn et al., 2007b]. The combination of the lack of a standardized $^{90}$Y microsphere activity determination and the inaccurate evaluation of the distribution of microspheres within the patient's liver results in large uncertainties in the dosimetry of $^{90}$Y microspheres. These uncertainties have lead to the inability to correlate the dose delivered with the clinical outcome of patients. In turn, the $^{90}$Y microsphere treatment remains largely unoptimized and is primarily used as a last-resort treatment with the end goal of palliation.

The report of the American Association of Physicists in Medicine (AAPM) Task Group 144 provides an overview of the present procedures and the current best-practice treatment methods for the $^{90}$Y microspheres [Dezarn et al., 2011]. The report also provides a list of recommendations for future improvements of the $^{90}$Y microsphere treatment. These include: development a National Institute of Standards and Technology (NIST)-traceable activity standard, development of a well-type ionization chamber calibration protocol that provides users with the ability to accurately determine $^{90}$Y microsphere activity in the clinic, and implementation of an image-based, three-dimensional dosimetry to provide patient-specific dose distributions resulting from the treatment.

This dissertation work created a non-destructive activity assay for $^{90}$Y microspheres that could be used as a primary measurement. This was accomplished by developing a coincidence detection spectrometry system that consisted of a large sodium iodide (NaI) detector and a high-purity germanium (HPGe) detector. This coincidence detection system (CDS) detected coincident 511 keV annihilation photons emitted from $^{90}$Y due to internal pair production. A newly-determined branching ratio for $^{90}$Y internal pair production [Selwyn et al., 2007a] was used to determine the activity of the sample from the spectra measurements. In addition, this work established the ability to transfer this activity measurement to

well-type ionization chambers. Characterization of these chambers enabled more accurate clinical determinations of activity of $^{90}$Y microsphere samples. Implementing a calibration service with this traceability to a single measurement device would help to reduce uncertainties in inter-institutional comparisons and help to improve patient-specific dosimetry. Additionally, the effects of the microsphere material on dose kernels used in image-based dosimetry were investigated. The results of this dissertation work serve to improve the dosimetry for $^{90}$Y microsphere treatments of liver malignancies.

## 1.2 Description of upcoming chapters

Chapter 2 provides a general description of liver cancer treatments as well as specific information on the $^{90}$Y microsphere treatment. The physical properties of $^{90}$Y and the present measurement methods used to determine $^{90}$Y activity are discussed. This includes a discussion on the calibration protocols used with well-type ionization chambers for the clinical determination of $^{90}$Y activity. Background information is provided on the development of an image-based dosimetry for $^{90}$Y microspheres, and the final section of the chapter focuses on the the motivations and goals for this thesis work.

Chapter 3 describes the development and characterization of the CDS that was created for assaying the activity of $^{90}$Y. The construction of the system is described; including the selection of the detectors, methods used to align the detectors, and the tuning of the signal-processing electronics. The advantages provided by the CDS over a single detector are demonstrated. The implementation and validation of a method for correcting for counting losses using a series of pulse generators is described. The results of a geometric sensitivity characterization of the CDS are presented. This analysis provided the ability to select the optimal source location for measurements.

Chapter 4 focuses on the use of the CDS to assay the activity of $^{90}$Y sources. The corrections required for an accurate assay of $^{90}$Y activity from measurements with the

CDS are discussed, such as the corrections for radioactive decay and the correction for attenuation differences between efficiency calibration and source-of-interest measurement geometries. The measurement methods and results of activity assays of a $^{90}YCl_3$ standard activity solution and a $^{90}Y$ microspheres sample are described. The uncertainties associated with the $^{90}Y$ activity assays are presented.

Chapter 5 presents the characterization of two well-type ionization chambers for the clinical activity determination of $^{90}Y$ microspheres that was completed with both measurements and Monte Carlo simulations. The well-type ionization chambers were calibrated for the measurement of both a $^{90}YCl_3$ solution and resin $^{90}Y$ microspheres in multiple source vials. The volume dependencies of the chambers were determined, and the effects of these dependencies on the measured activity were evaluated. Additionally, the effects of vial wall thickness and positioning within the well of the chamber were analyzed.

Chapter 6 describes the effects of the microsphere and surrounding material composition on the $^{90}Y$ dose kernel used for calculating the dose distribution from $^{90}Y$ microsphere treatments with an image-based dosimetry. These $^{90}Y$ dose kernels were calculated using two Monte Carlo transport codes for both glass and resin $^{90}Y$ microspheres. The differences between performing simulations in water or liver were evaluated, and a comparison of the two investigated transport codes is provided.

Chapter 7 presents the overall conclusions and implications of the research presented in the preceding chapters. Potential future work to continue to improve the $^{90}Y$ microsphere treatment is also presented.

# Chapter 2

# Background

## 2.1 Liver cancer treatment

Liver cancer can present as a primary cancer that originates in the liver or as a secondary cancer that has metastasized to the liver from a number of primary locations such as the colon, lungs, breast, pancreas, stomach, or ovary [Thomson and Shaffer, 2005]. According to the American Cancer Society, there will be an estimated 28 720 new cases of primary liver cancer in the U.S. in 2012 with 20 550 deaths due to the disease [American Cancer Society, 2012]. Additionally, each year more than 50 000 patients in the U.S. will present with liver metastases secondary to colorectal cancer [Fong et al., 1997]. The only potentially curative treatments of liver malignancies currently available are liver transplants or partial liver resections. However, few opportunities for liver transplants exist with an average of only about 6000 performed in the U.S. each year. Additionally, only about 10 % of these transplant livers go to patients with hepatic malignancies since transplants are often preferentially given to patients with more curable diseases [American Cancer Society, 2011]. Resectability rates are also low with only $10-20$ % of liver cancer patients being candidates for surgical resection. This is due to a combination of factors including tumor size, poor underlying liver function, and the presence of metastatic disease [Johnson, 1995]. Often

treatment of non-resectable liver cancer is considered palliative with an end goal of increasing the survival time, reducing pain, and improving quality of life. Several modalities are clinically available for the treatment of non-resectable liver cancer including: chemotherapy, tumor ablation, and radiation therapy.

Chemotherapy uses pharmaceutical agents that typically target rapidly-dividing cells (i.e., cells undergoing mitosis). Cancerous cells typically exhibit an accelerated rate of mitosis, thus chemotherapy agents preferentially affect these cells. Systemic chemotherapy drugs are injected intravenously and reach all areas of the body via the blood stream. This can be effective in treating cancer that has spread to distant organs; however, liver malignancies are resistant to most systemic chemotherapy. New methods for the delivery of chemotherapy agents have been developed to attempt to combat this resistivity. Hepatic artery infusion (HAI) is a technique in which chemotherapy drugs are delivered directly into the hepatic artery. Studies have shown this technique is more effective than traditional systemic chemotherapy [Lygidakis et al., 2001]. Another novel chemotherapy delivery technique is trans-arterial chemoembolization (TACE). TACE involves injecting drug-eluting embolizing material into the hepatic artery. Embolization reduces the blood flow to the tumor while also helping to localize the chemotherapy agent within the liver. Studies have shown that this technique helps improve patient survival [Llovet and Bruix, 2003].

Ablation refers to the localized destruction of tissues and can be accomplished by a number of methods. These techniques can be used to destroy a few number of small non-resectable tumors within the liver. One technique called radiofrequency ablation (RFA) involves placing a needle-like probe through the skin and into the liver at the tumor site. The tip of the probe has the ability to heat the surrounding tissues to lethal temperatures, killing the cells surrounding it. Another ablative method is cryosurgery. This technique is similar to RFA in that a probe is placed within the tumor. However, cryosurgery uses liquid

nitrogen within the probe to freeze and destroy the tumor. Both of these techniques can also be used to supplement surgical resection [Liu et al., 2003].

External beam radiation therapy is limited in its ability to treat liver malignancies due to the radiosensitive nature of normal liver tissue, which is limited to a total dose of approximately 30 Gy before radiation hepatitis may occur [Emami et al., 1991, Marks et al., 2010]. Studies have shown that by limiting the dose to healthy tissue and using advanced techniques such as stereotactic body radiation therapy (SBRT), the delivery of tumor doses of up to 60 Gy can be achieved with limited toxicities [Rusthoven et al., 2009, Katz et al., 2007]. However, Ho et al. [1997] suggested that the tumorcidal dose for hepatic tumors is 120 Gy. An alternative radiation therapy technique that is capable of delivering doses to this tumorcidal level is microbrachytherapy. Microbrachytherapy for the treatment of liver malignancies involves injecting microspheres with embedded or attached beta-emitting radionuclides [most commonly yttrium-90 ($^{90}$Y)] directly into the hepatic artery. The approximately 30-$\mu$m-diameter spheres are trapped in the arterioles of the liver where the $^{90}$Y can deliver a high average dose of 200-300 Gy to liver tumors. Microbrachytherapy has been shown to be effective with limited complications and has the potential to convert non-resectable tumors to resectable ones [Lau et al., 1998].

## 2.2 $^{90}$Y microspheres for the treatment of liver malignancies

The underlying rationale for the microsphere treatment was established in work completed by Breedis and Young [1954] in which it was shown that liver malignancies receive approximately 80 % of their blood supply via the hepatic artery and 20 % from the portal vein, whereas normal liver tissue receives 80 % of its blood supply from the portal vein and 20 % from the hepatic artery. The microsphere treatment takes advantage of this disproportionate dual blood supply by injecting $^{90}$Y microspheres directly into the hepatic artery, thereby preferentially delivering the resulting dose to the cancerous tissue within the liver. This is

Table 2.1: Comparison of SIR-Spheres and TheraSphere properties.

| Property | SIR-Spheres | TheraSphere |
|---|---|---|
| Manufacturer | Sirtex Medical | MDS Nordion |
| Material | Resin | Glass |
| Diameter ($\mu$m) | 20-60 | 20-30 |
| Activity per sphere (Bq) | 50 | 2500 |
| Location of $^{90}$Y | Uniform on surface | Uniform within volume |

accomplished by placing a catheter percutaneously into the patient's femoral artery and guiding it to the hepatic artery using fluoroscopic imaging.

There are currently two commercially available $^{90}$Y microsphere products: TheraSphere® (MDS Nordion, Ottawa, Canada) consists of $^{90}$Y embedded in a glass matrix, and SIR-Spheres® (Sirtex Medical, North Sydney, Australia) are composed of resin loaded with $^{90}$Y. Table 2.1 compares the properties of these two products. Both are classified as medical devices by the U.S. Food and Drug Administration (FDA).

SIR-Spheres are approved for the treatment of non-resectable metastatic liver cancer from primary colorectal cancer with adjuvant Floxuridine chemotherapy delivered via HAI. They are provided by the manufacturer in a glass shipping vial with an activity of 3 GBq in a 5 mL solution of sterile water. TheraSphere are approved for the treatment of non-resectable hepatocellular carcinoma. They are supplied by the manufacturer in a 1.0 mL v-vial. The v-vial is surrounded by a non-removable 12 mm polymethyl methacrylate (PMMA) shield. The spheres are in a 0.6 mL solution of sterile water within the v-vial. TheraSphere can be ordered from the manufacturer at six activity levels: 3, 5, 7, 10, 15, and 20 GBq. The off-label use of these products, such as using one of the products for the treatment of a disease it is not approved for, is discussed by Thomadsen et al. [2010]. It is recommended that off-label use of either of the $^{90}$Y microsphere products be conducted under the supervision of an institutional review board [Dezarn et al., 2011].

Indications for the $^{90}$Y microsphere procedure include: non-resectable liver cancer, a liver-dominant tumor burden, and a life expectancy of at least 3 months [Kennedy et al.,

2007]. Two absolute contraindications are: excessive hepatopulmonary shunting and excessive gastrointestinal shunting. These contraindications can result in pneumonitis or gastric ulceration, respectively. The presence of these contraindications are determined prior to treatment with a technetium-99m macro aggregate albumin ($^{99m}$Tc-MAA) imaging study [Murphy et al., 2006]. The $^{99m}$Tc-MAA acts as a surrogate to the $^{90}$Y microspheres to determine their potential distribution within the patient. The relative lung and gastrointestinal shunting can be determined from these scans.

Both products follow the same dosimetry model which is based on the schema developed by the Medical Internal Radiation Dose (MIRD) Committee [Howell et al., 1999]. In this schema, the liver dose for a given injected activity and liver mass is given by the equation,

$$\text{Dose (Gy)} = \frac{[\text{Injected activity (GBq)}] \cdot [49.38\,\text{Gy} \cdot \text{kg/GBq}]}{\text{Liver mass (kg)}}. \tag{2.1}$$

The 49.38 Gy·kg/GBq constant is specific to $^{90}$Y. It assumes that all of the beta emissions are absorbed in the given tissue and that the average energy absorbed per emission is 0.93 MeV from $^{90}$Y. It also takes into account the radioactive decay of $^{90}$Y from the initial injected activity. The derivation of this constant is given by Dezarn et al. [2011]. Equation 2.1 assumes that the microspheres are uniformly distributed within the liver, but it has been shown from explanted livers that this assumption is not valid [Kennedy et al., 2004].

Activity prescription methods differ between the two $^{90}$Y microsphere products [Kennedy et al., 2007]. For TheraSphere, a dose prescription is given by the physician and is typically between 100 and 120 Gy [Dezarn et al., 2011]. Then Equation 2.1 is solved for activity, $A$, as given by,

$$A = \frac{D \cdot m}{49.38}, \tag{2.2}$$

Table 2.2: Multiplicative factors for determining the prescribed activity with the Empiric method for the SIR-Spheres.

| Extent of tumor by percent of liver mass (%) | Baseline activity (GBq) |
|---|---|
| $> 50$ | 3.0 |
| $25 - 50$ | 2.5 |
| $< 25$ | 2.0 |
| **Lung shunting (%)** | **Lung shunt modifier** |
| $< 10$ | 1.0 |
| $10 - 15$ | 0.8 |
| $15 - 20$ | 0.6 |
| $> 20$ | Do not proceed |
| **Portion of liver** | **Liver portion modifier** |
| Whole liver | 1.0 |
| Right lobe | 0.7 |
| Left lobe | 0.3 |

where $D$ is the prescription dose and $m$ is the mass of the liver. Once $A$ has been determined and the treatment time scheduled, the appropriate activity level can be ordered from the manufacturer.

For SIR-Spheres, there are three activity prescription methods. The first is the Empiric method. This method prescribes a standard baseline activity based on the the extent of the disease and then modifies this baseline value based on the amount of lung shunting and portion of the liver being treated (e.g., whole liver versus the right lobe). Table 2.2 provides the multiplicative factors for calculating the prescription activity using the Empiric method. The appropriate values are then used in the equation,

$$A = \text{Baseline activity} \times \text{Lung shunt modifier} \times \text{Liver portion modifier}, \tag{2.3}$$

to determine the prescribed activity, $A$, in units of GBq. This method was used in the clinical trials associated with the SIR-Spheres product [Gray et al., 2001], but is no longer recommended by the manufacturer since it does not account for the actual size of the liver and has a less favorable toxicity profile compared to the other prescription methods

[Kennedy et al., 2007]. The second method used for SIR-Spheres is the Body Surface Area (BSA) method. This method uses the equation,

$$A = BSA - 0.2 + \frac{V_{\text{Tumor}}}{V_{\text{Liver}}}, \tag{2.4}$$

to calculate the prescription activity, $A$, where $V_{\text{Tumor}}$ is the volume of the tumor and $V_{\text{Liver}}$ is the total volume of the liver. The BSA (in units $\text{m}^2$) is calculated using the equation,

$$BSA = 0.20247 \cdot h^{0.725} \cdot w^{0.425}, \tag{2.5}$$

where $h$ is the height of the patient in meters and $w$ is the weight of the patient in kilograms. The third method is the Partition Model. To determined the total activity, $A_{\text{Total}}$, to be delivered, this method uses the equation,

$$A_{\text{Total}} = \frac{D_{\text{Tumor}}(\frac{m_{\text{Normal liver}}}{T:N} + m_{\text{Tumor}})}{49.38(1-L)} \tag{2.6}$$

which is a modification of Equation 2.1, where $D_{\text{Tumor}}$ is the dose to the tumor, $m_{\text{Normal liver}}$ is the mass of the normal liver tissue, $m_{\text{Tumor}}$ is the mass of the tumor, $L$ is the fractional lung shunting, and $T : N$ is the tumor-to-normal-liver activity uptake ratio and is defined by the equation,

$$T : N = \frac{A_{\text{Tumor}}/m_{\text{Tumor}}}{A_{\text{Normal liver}}/m_{\text{Normal liver}}}. \tag{2.7}$$

The $T : N$ is determined from the $^{99\text{m}}$Tc-MAA pretreatment imaging studies [Ho et al., 1997] and can be used to determine the dose to the normal liver tissue, $D_{\text{Normal liver}}$, based on $D_{\text{Tumor}}$ using the equation,

$$D_{\text{Normal liver}} = \frac{D_{\text{Tumor}}}{T : N}. \tag{2.8}$$

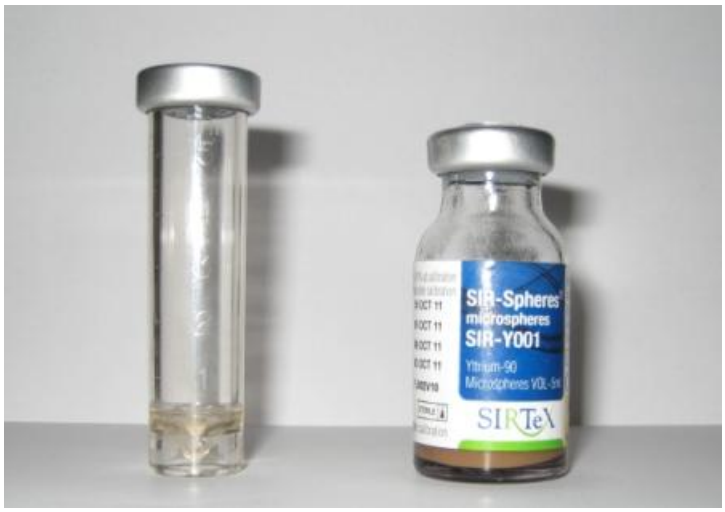


Figure 2.1: Photograph of the SIR-Spheres v-vial (left) and shipping vial (right).

Once the prescription activity has been determined for the SIR-Spheres treatment, the desired activity is drawn out of the glass shipping vial and placed in a polycarbonate v-vial for delivery to the patient (see Figure 2.1). This activity preparation process is described in detail in Section 5.1.1.

The AAPM recently published their recommendations for the best practices and procedures for using $^{90}$Y microspheres for the treatment of liver malignancies [Dezarn et al., 2011]. The report lists potential future improvements for the $^{90}$Y microsphere treatments including: development of a National Institute of Standards and Technology (NIST)-traceable activity standard for $^{90}$Y microspheres, development of a calibration service for clinical measurement devices that could be provided by Accredited Dosimetry Calibration Laboratories (ADCLs), and development of three-dimensional (3D) image-based dosimetry techniques for the calculation of dose-volume histograms. These improvements would provide the means to complete meaningful patient-response studies and develop radiobiological models to help optimize $^{90}$Y microsphere treatments.

## 2.3 Physical properties of $^{90}$Y

$^{90}$Y is a beta emitter with an end-point energy of 2.28 MeV and an average energy of 0.93 MeV, giving the beta particles a maximum range of approximately 11 mm in water. Figure 2.2 shows the $^{90}$Y beta energy spectrum from the International Commission of Radiation Units and Measurements (ICRU) report 72 [2004]. $X_{90}$, the radial distance in which 90 % of the emitted energy is absorbed, is 5.43 mm for $^{90}$Y in water [Mainegra-Hing et al., 2005]. $^{90}$Y is typically produced in reactors through neutron bombardment of $^{89}$Y or through chemical separation from $^{90}$Sr. It decays predominantly to the ground state of $^{90}$Zr with a half-life of $(64.053 \pm 0.020)$ h [Kossert and Schrader, 2004], though it also decays to the $0^+$ first excited state of $^{90}$Zr with a branching ratio of $1.15 \times 10^{-4}$. This is demonstrated in the $^{90}$Y decay scheme shown in Figure 2.3. This excited state of $^{90}$Zr subsequently decays via internal conversion, two-photon de-excitation, or internal pair production (IPP) [Ryde et al., 1961]. A previous study [Langhoff and Hennies, 1961] had reported an IPP branching ratio of $(3.4 \pm 0.4) \times 10^{-5}$, but recent work by Selwyn et al. [2007a] determined the branching ratio of the IPP to be $(3.186 \pm 0.047) \times 10^{-5}$. The decreased uncertainty of this recently-determined branching ratio over the previously reported one makes an accurate non-destructive spectroscopic activity assay of $^{90}$Y possible.

## 2.4 Measurement methods used to determine $^{90}$Y activity

### 2.4.1 Liquid scintillation counting

For liquid scintillation (LS) counting, the radioactive sample is dissolved in a scintillation solution prior to counting. The prepared solution is placed in a liquid scintillation counter, which consists of a light-tight chamber centered between opposed photomultiplier tubes (PMTs). As beta emissions from the sample are absorbed by the scintillation solution, light is emitted isotropically and with an intensity proportional to the energy absorbed.

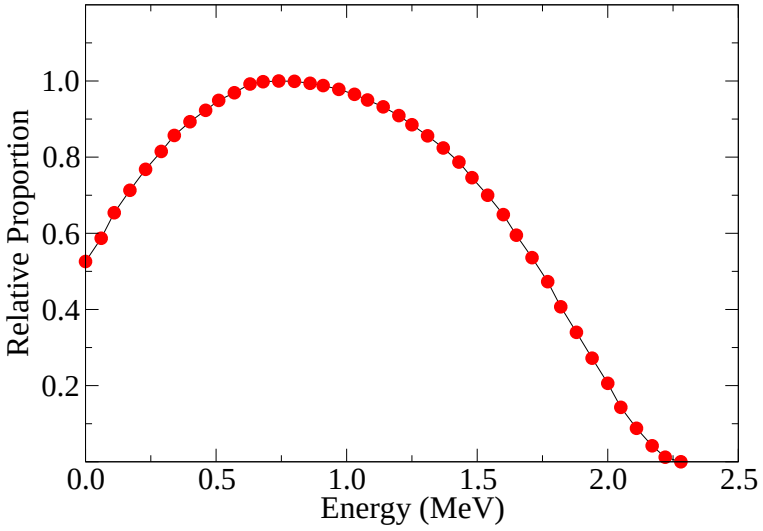


Figure 2.2: The $^{90}$Y beta-energy spectrum from ICRU 72.

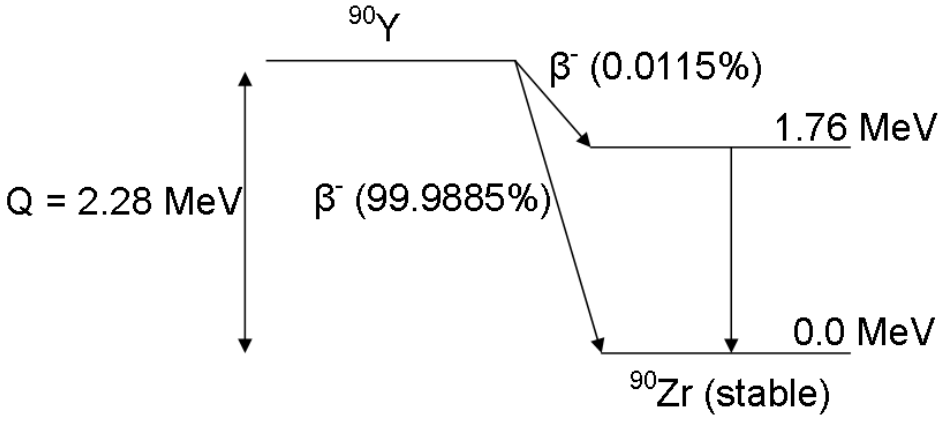


Figure 2.3: $^{90}$Y decay scheme diagram.

The emitted light is detected by the PMTs. The signals from the PMTs are sent to a coincidence circuit in order to reduce the noise associated with the detection system. The output of the coincidence circuit is sent to an amplifier to increase the signal and then to a multichannel analyzer (MCA) to create a pulse-height spectrum. The spectrum can then be analyzed to determine the sample's activity [Cherry et al., 2003].

NIST uses high-efficiency LS counting to standardize solutions of beta-emitters. For $^{90}$Y, activity standardization has been completed [Kossert and Schrader, 2004, Coursey et al., 1993] using the Centro de Investigaciones Energeticas, Medioambientales y Technologicas (CIEMAT)/NIST method of LS efficiency tracing with $^{3}$H [Coursey et al., 1986]. This method is able to achieve activity assays of $^{90}$Y with expanded uncertainties ($k = 2$) of less than 1 %. However, this destructive assay method requires large dilutions of clinically-relevant $^{90}$Y solutions to bring activity levels down to those acceptable for LS counting. NIST provides a standard $^{90}YCl_3$ radioactivity solution annually through its Standard Reference Materials (SRM) program.

Mo et al. [2005] calibrated a well ionization chamber at the Australian Nuclear Science and Technology Organisation (ANSTO) for the measurement of $^{90}$Y activity using a stock $^{90}$Y solution whose activity concentration had been determined by NIST using the CIEMAT/NIST techniques described above. Activities of 1 mL chemically-digested $^{90}$Y microsphere samples were determined using this calibration. These activity measurements were then related to clinically-relevant 5 mL undigested microsphere samples to determine well-type ionization chamber calibration coefficients. The stated uncertainties associated with these determined calibration coefficients were approximately 2.5 %.

### 2.4.2 Spectroscopic assay using a HPGe detector

As mentioned in Section 2.3, Selwyn et al. [2007a] determined a new branching ratio of $(3.186 \pm 0.047) \times 10^{-5}$ for the IPP component of $^{90}$Y decay. Selwyn et al. [2008] then

used the newly-determined branching ratio to spectroscopically determine the activity of a sample of $^{90}$Y microspheres. This was accomplished by measuring the resulting 511 keV peak with a high-purity germanium (HPGe) spectrometer. A $^{22}$Na reference source was used to determine the efficiency of the detector to 511 keV photons. Measurements of the $^{90}$Y microspheres were taken in the same geometry as the measurements of the $^{22}$Na reference source. The equation,

$$A = \frac{\dot{N}}{r \cdot \varepsilon} \prod k_i, \tag{2.9}$$

was used to determine the activity, $A$, where $\dot{N}$ is the net count rate of the 511 keV peak area, $r$ is the branching ratio of the IPP, $\varepsilon$ is the efficiency of the the detector, and $k_i$ is a series of corrections described in detail by Selwyn et al. [2007a]. After 167 h of detection, this method determined the sample activity to be 3.807 GBq $\pm$ 1.8 %. However, this determined activity was 26 % higher than the 3.0 GBq $\pm$ 10 % activity stated by the manufacturer [Selwyn et al., 2008].

Due to the long detection times required for satisfactory statistics, Selwyn et al. [2007a] suggested that this technique could be improved by using coincidence detection methods to reduce the bremsstrahlung continuum in the measured spectrum. However, they also stated that a coincidence detection system would have a greater geometric dependence than a single detector system. This dissertation aimed to develop a coincidence detection system that paired a large NaI detector with a HPGe detector. The geometric dependence of the system was characterized such that it can be accounted for during measurements. The construction and characterization of this system is discussed in Chapter 3.

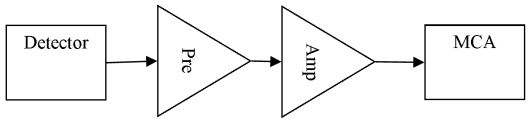


Figure 2.4: Electronics block diagram of a typical spectrometry system.

## 2.5 Gamma-ray spectrometry

Gamma-ray spectrometry systems are able to provide energy distribution information about the radiation emitted from a source-of-interest. This information can be used to identify an unknown radionuclide or determine the activity of a particular radionuclide in a sample. In order to provide this information, the detector must have an output signal that is proportional to the absorbed gamma-ray energy, have a mechanism for collecting this signal, have good efficiency (i.e., high absorption coefficient), and remain stable over time [Gilmore, 2008]. These requirements are met in different ways depending on the detection material used. The most common detector material types for gamma-ray spectrometry are semiconductors and scintillators. The specifics of each of these detector types are described in the subsequent sections; however, the electronics used to process the output signal for both detector types are very similar. The typical electronics chain consists of a preamplifier to match the impedance of the detector and subsequent electronics and shape the signal pulse, an amplifier to amplify the signal pulse, and a MCA to digitize the input pulse into a bin based on its amplitude [Cherry et al., 2003]. An electronics block diagram of a typical spectrometry system is shown in Figure 2.4. This process creates a pulse-height spectrum.

### 2.5.1 Semiconductor detectors

In semiconductor detectors, a fully-absorbed gamma ray creates a number of electron-hole pairs that is proportional to the initial energy of the gamma ray. This charge is collected by placing a voltage across the sensitive semiconductor material. There are a number of semiconductor materials that are used for gamma-ray detectors, the most popular are silicon ($Z = 14$) and germanium ($Z = 32$). Due to its lower atomic number and resulting poorer absorption coefficient, silicon is typically only used for the measurement of low-energy photons. With its higher atomic number and excellent energy resolution (approximately 0.2 % at 662 keV), germanium has become the most common gamma-ray spectrometer material. However, due to the small band gap of germanium (approximately 0.7 eV) and the resulting thermally-induced leakage, germanium detectors cannot be operated at room temperature. Liquid nitrogen, with a boiling temperature of 77 K, is typically used to cool germanium detectors [Gilmore, 2008].

### 2.5.2 Scintillator detectors

In scintillation detectors, an absorbed gamma ray excites electrons to a higher energy level. Upon the prompt de-excitation of these electrons, visible light is emitted that is proportional to the initial energy of the gamma ray [Gilmore, 2008]. This visible light is detected by a PMT, where it it is converted into an electrical signal. NaI is the most commonly used scintillator material. NaI has a worse energy resolution (approximately 4 % at 662 keV) compared to HPGe, but is available in large sizes. This availability of large sizes and the relatively high $Z$ of iodine give NaI a relatively high interaction probability.

### 2.5.3 Timing methods

In a number of spectrometry applications, information on the arrival time of gamma rays within a detector is desired in addition to the energy information. Positron emission tomog-

raphy (PET) and Compton suppression systems (CSSs) are two examples of applications that use time-correlated events occurring within multiple detectors to perform a function. PET systems detect annihilation photons in coincidence in order to localize a positron-emitting radionuclide within a patient. CSSs reject coincident events in order to reduce the Compton continuum in the measured spectrum. The ability to obtain precise timing information depends on the properties of the detectors being used as well as on the electronics used to process the signals. A detector's timing properties depend on the time the detector takes to process a signal (i.e., how quickly the detector can collect the signal charge). The electronics of a detection system employ time pick-off methods to indicate the time-of-occurrence of an input pulse. Knoll [2000] describes a number of these methods including: leading edge triggering, crossover timing, and constant fraction timing. Each of these methods have their advantages and disadvantages depending on the needs of the detection system.

To determine the uncertainty in the timing properties of a coincidence detection system, the timing spectrum can be measured. The timing spectrum is a plot of the difference in arrival time of the signals from the two detectors in a coincidence detection system due to a truly-coincident event. This information helps the user determine the size of the timing window needed to accept truly-coincident detected events. It is important to optimize the timing of the system (i.e., minimize the width of the timing peak) to help reduce the random coincidence count rate, $R_{\text{random}}$, given by Equation 2.10, where $2\tau$ is the coincidence timing window and $R_1$ and $R_2$ are the individual count rates of each detector.

$$R_{\text{random}} = 2\tau \cdot R_1 \cdot R_2 \tag{2.10}$$

The CDS investigated in this work detected the annihilation photons from the IPP component of $^{90}$Y decay in coincidence and then used this coincidence signal to gate the input energy signal from the HPGe detector. This reduced the bremsstrahlung continuum

that surrounded the 511 keV peak. The bremsstrahlung continuum that remained in the gated spectrum was proportional to the random coincidence count rate. This system used the same mechanism of annihilation coincidence detection as PET, but had the same end goal of a CSS of reducing the continuum surrounding the region of interest in the energy spectrum.

## 2.6 Well-type ionization chamber calibrations and measurements

Well-type ionization chambers are known by a number of names including: re-entrant chambers, dose calibrators, or well chambers. Regardless of name, all well-type ionization chambers operate in a similar manner. They are able to measure the ionizations created in the gas of the sensitive volume of the chamber due to the radiation emitted from the sample placed in the well of the chamber. This measurement is accomplished by placing a voltage across the gas volume of the chamber and measuring the resulting ionization current with an electrometer. These chambers are used for their maximized geometric sensitivity (nearly $4\pi$). Figure 2.5 shows a schematic of a well-type ionization chamber, including the electric field lines resulting from the applied voltage.

The name used for a well-type ionization chamber is usually indicative of the department where it is being used. The term "dose calibrator" typically refers to a well-type ionization chamber used by nuclear medicine departments to determine the activity of radioactive tracers used for imaging studies. These chambers are typically sealed and filled with a pressurized gas (usually argon) [Cherry et al., 2003]. This serves to increase the sensitivity of the chamber, but can also result in a decreased response of the chamber by approximately 1 % per year as the pressurized gas leaks from the chamber [DeWerd et al., 2009a]. It is recommended that a constancy check be performed daily on dose calibrators to check their operation and quantify any drift in their response [IAEA, 2006]. Dose calibrators also

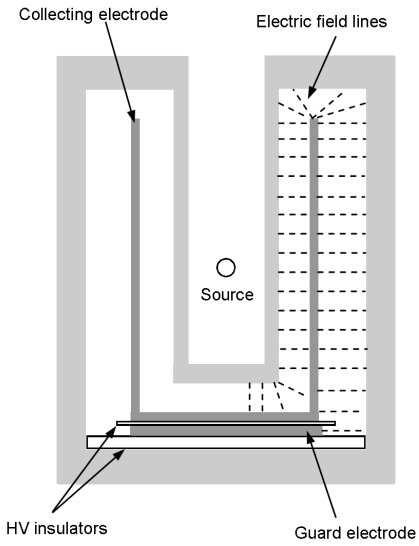


Figure 2.5: Schematic of a well-type ionization chamber with electric field lines.

typically have a non-removable electrometer that has dial settings for different radionuclides, and the readout of the electrometer is usually in units of activity (e.g., mCi or MBq).

The term "well chamber" typically refers to a well-type ionization chamber used in a radiation oncology department to determine the strengths of brachytherapy sources that are used for the treatment of cancer [DeWerd et al., 2009b]. These chambers are usually open to the atmosphere (i.e., not sealed). This means that measurement results must be corrected back to standard temperature and pressure (in the U.S., 22°C and 101.3 kPa, respectively) using multiplicative correction, $k_{\mathrm{TP}}$, defined by the equation,

$$k_{\mathrm{TP}} = \frac{273.2 + T}{273.2 + 22} \cdot \frac{101.3}{P}, \tag{2.11}$$

where $T$ is the measured temperature in °C and $P$ is the measured pressure in kPa. Well chambers ionization current measurements are typically performed using a separate electrometer.

### 2.6.1 Calibration

To determine a quantity-of-interest (e.g., activity) from ionization current measurements, well-type ionization chambers must be calibrated. The calibration methodology for well-type ionization chambers differs between nuclear medicine and radiation oncology departments. Typically, the dial setting of a dose calibrator for a particular radionuclide is determined during its calibration. Calibration of dose calibrators is performed by the manufacturer of the device through the use of standard sources, such as those distributed through the radiopharmaceutical SRM program of NIST. These liquid sources have a standard geometry. The standard NIST geometry is a 5 mL flame-sealed, thin-walled glass ampoule. However, Zimmerman and Cessna [2000] noted that these calibrations are only valid for the NIST geometry, and deviations from this geometry (such as volume, container, solution composition, or solution density) must be taken into account for the accurate determination of activity.

Well chambers used to determine the source strength of many of the brachytherapy sources in radiation oncology are sent to an Accredited Dosimetry Calibration Laboratory (ADCL) for calibration. In this methodology, the quantity-of-interest of the source is determined using a primary measurement device. For example, the source strengths (air-kerma strength, $S_{\mathrm{K}}$) of low-dose rate (LDR) brachytherapy sources (such as those utilizing $^{125}$I or $^{103}$Pd) are determined using the NIST Wide-Angle Free-Air chamber (WAFAC) [Seltzer et al., 2003]. NIST or an ADCL then calibrates the user's well chamber with the same measurement geometry that will be used clinically using the source that has been measured with the primary measurement device (i.e., it has a known quantity-of-interest). This eliminates the uncertainties associated with calibration measurement geometry differing from the clinical measurement geometry. The ratio of the known quantity-of-interest and the measured ionization current from the well chamber is provided to the user from NIST or the ADCL as a calibration coefficient, $N_X$. The user can then use the equation,

$$X = M_{\text{raw}} N_X \prod k_i, \tag{2.12}$$

to clinically determine the quantity-of-interest, $X$, where $M_{\text{raw}}$ is the uncorrected current reading from the well chamber and $k_i$ is a series of correction factors (e.g., $k_{\text{TP}}$).

For this thesis work, the quantity-of-interest was the activity of a $^{90}$Y microsphere sample. Dezarn [2008] noted that the creation of a NIST-traceable $^{90}$Y microsphere calibration standard is difficult due to the nature of the microsphere procedure being between current methods used in radiation oncology and those used in nuclear medicine. Presently, the activity of a sample of $^{90}$Y microspheres is determined using dose calibrators based on an activity provided by the manufacturer [Dezarn and Kennedy, 2007]. This work investigated using a coincidence detection system as the primary measurement of $^{90}$Y microsphere activity for the calibration of well-type ionization chambers. Both a well chamber and a dose calibrator were investigated for the clinical determination of the activity of a $^{90}$Y microsphere sample. These results are presented in Chapter 5.

### 2.6.2 Measurement of $^{90}$Y sources

For beta emitters such as $^{90}$Y, dose calibrators typically do not measure ionizations due directly to the beta particles, but rather measure the ionizations due to the continuous bremsstrahlung spectrum produced by the beta particles [Coursey et al., 1993]. The emitted bremsstrahlung spectrum depends strongly on source holder material and geometry. Thus, calibrations that have been performed using a geometry different from the measurement geometry are not valid and can lead to large discrepancies. Wastiel et al. [2005] and Zimmerman and Cessna [2000] found that using the manufacturer's recommended dose calibrator dial settings could result in differences from the actual $^{90}$Y activity as large as 50 % due to differences in the measurement geometry from the calibration geometry. Likewise, Dezarn and Kennedy [2007] investigated activity measurements of $^{90}$Y microspheres and

found that measurements with a polycarbonate v-vial were 20 % higher than those taken with the glass shipping vial for the same dial setting. Additionally, some of these chambers have sample-volume dependent responses [Zimmerman et al., 2004, Kryeziu et al., 2007]. This work has investigated these effects on the clinical measurements in well-type ionization chambers used for the determination of $^{90}$Y microsphere sample activity.

## 2.7 Image-based dosimetry

Presently, three-dimensional (3D) image-based dosimetry is not typically performed for $^{90}$Y microsphere treatments, but it has been noted as a potential improvement for the treatment [Dezarn et al., 2011]. Many of the clinical studies associated with $^{90}$Y microsphere treatments simply assume a uniform activity distribution within the liver [Sarfaraz et al., 2004]. However, it has been shown from explanted livers that this assumption is not correct [Campbell et al., 2000, Kennedy et al., 2004]. Instead, microspheres are typically distributed non-uniformly in clusters around the periphery of tumors [Pillai et al., 1991]. The partition model, as discussed in Section 2.2, can be used to account for the different activity uptakes of tumor and normal liver [Sarfaraz et al., 2003]. This method has been shown to be effective in predicting outcome [Campbell et al., 2009]. However, this method still assumes the activity within each partition to be uniform. Williams et al. [2008] also concluded that improving patient-specific dosimetry associated with targeted therapies, such as $^{90}$Y microspheres, would lead to improved clinical outcome with better controlled toxicities.

Zaidi [1999] explained that the three requirements for 3D image-based dosimetry are the 3D activity concentration within the patient, the 3D anatomical data of the patient, and the Monte Carlo-calculated dose kernel. Patient-specific, 3D absorbed doses from beta-emitting sources have been calculated for radioimmunotherapy (RIT) treatments by convolving the nonuniform radionuclide activity concentrations with the dose kernel of the radionuclide

in use [Kolbert et al., 1997, Erdi et al., 1998, Sgouros et al., 2003]. This is given by the equation,

$$D(r) = \int_V \tilde{A}(r') \cdot k(r - r')\, dV', \tag{2.13}$$

where $D(r)$ is the absorbed dose at $r$, $\tilde{A}(r')$ is the accumulated activity at $r'$, and $k(r - r')$ is the spatially invariant dose kernel between $r$ and $r'$. The dose kernel describes the dose deposited as a function of distance from an ideal isotropically-emitting point-like source in water. Due to the difficulty of accurately measuring the high-dose gradient from a beta-emitting source, Monte Carlo methods have been used to calculate the dose kernels for therapeutic radionuclides (such as $^{90}$Y or $^{32}$P) [Prestwich et al., 1989, Simpkin and Mackie, 1990]. Sarfaraz et al. [2004] applied the discussed convolution dose calculation method to $^{90}$Y microsphere treatments.

Sarfaraz et al. [2004] used single-photon emission computed tomography (SPECT) images from pretreatment $^{99m}$Tc-MAA hepatic infusion studies as a surrogate for the activity distribution of $^{90}$Y microspheres. The dose distribution within the liver was determined and dose-volume histograms were calculated for both the tumor and the normal liver tissue. It has been suggested that positron-emitting surrogates (such as $^{18}$F doped microspheres) imaged with PET may provide a better representation of the actual distribution of microspheres within the liver and with a higher spatial resolution than $^{99m}$Tc-MAA SPECT images [Avila-Rodriguez et al., 2007, Selwyn et al., 2007b]. Thesis work completed by Selwyn [2007] investigated the development of a image-based dosimetry using PET imaging. Most recently, it has been shown that PET images of injected $^{90}$Y microspheres may be obtained directly [Lhommel et al., 2009, Gates et al., 2011] by taking advantage of the internal pair production component of $^{90}$Y decay [Nickles et al., 2004, Selwyn et al., 2007a]. The PET scanner characteristics needed to achieve quantitative imaging of $^{90}$Y have also been studied [van Elmbt et al., 2011]. These advances in imaging contribute to the increased

feasibility and accuracy of patient-specific, 3D image-based dosimetry for $^{90}$Y microsphere treatments using the convolution dose calculation method.

## 2.8 Project motivations and goals

As presented in this chapter, there are large uncertainties associated with the clinical determination of activity for $^{90}$Y microspheres. This leads to a large uncertainties in the dose delivered to the patient. In turn, these large uncertainties result in the inability to correlate patient outcome with treatment technique. Though there are a number of studies that have shown positive results for $^{90}$Y microsphere treatments, little work has been done to optimize the treatment due to these large dosimetric uncertainties. Additionally, no primary activity standard exists for either of the commercially available $^{90}$Y microsphere products. Thus, clinical measurements are not traceable to a primary standard, which prevents any meaningful comparisons between institutions.

The overall goal of this project was to improve the dosimetry associated with $^{90}$Y microsphere treatments. This project extended the work of Selwyn et al. [2007a, 2007, 2008] by developing a coincidence detection spectrometry system to assay the activity of $^{90}$Y microsphere samples. This system has the potential to be a primary measurement device that could be used in the calibration of well-type ionization chambers for the clinical determination of $^{90}$Y microsphere activity. The response of well-type ionization chambers (both those typically used in radiation oncology and in nuclear medicine) were investigated in this work. The present clinical measurement methods were evaluated and the chambers were characterized to determine more optimal measurement procedures for use in the clinic. Additionally, the effects of the microsphere and surrounding material on the calculation of $^{90}$Y dose kernels were investigated. These dose kernels can be used in an image-based dosimetry for $^{90}$Y microspheres. Implementing the results of this work would serve to reduce the uncertainty in the dosimetry associated with $^{90}$Y microsphere treatments.

# Chapter 3

# Construction and characterization of the coincidence detection system

## 3.1 Introduction

Selwyn et al. [2007a] discussed the increased geometric sensitivity that results from using a coincidence detection system versus a single detector for detection of 511 keV annihilation photons. For this work, it was therefore necessary to construct an experimental setup that had the ability to limit and characterize this geometric sensitivity. Additional requirements of the setup included safely and reproducibly positioning the selected detectors and sources as well as accommodating the necessary Nuclear Instrumentation Module (NIM) electronics. This chapter describes the construction and the characterization of the coincidence detection system (CDS) used in this research. This includes the development of a counting losses correction and characterization of the geometric sensitivity of the system to determine the optimal source location for measurements.

Table 3.1: List of available detectors that were not selected for use in this research and reasoning.

| Detector | Material Type | Reason for omission |
|---|---|---|
| CdTe | Semiconductor | Too small |
| Si(Li) | Semiconductor | Too small |
| NaI (gamma camera) | Scintillator | Too thin |
| La-Halides | Scintillator | Too small |
| BGO (PET blocks) | Scintillator | Complexity |

## 3.2 Construction of experimental setup

### 3.2.1 Detectors

A number of semiconductor and scintillator detectors were available for potential use in this work. Several factors were considered prior to the final selection of the high-purity germanium (HPGe) and sodium iodide (NaI) detectors. These included the need for excellent energy resolution, excellent efficiency, and a geometry that would accommodate the size of the source (e.g., a vial containing $^{90}$Y microspheres). To reduce cost, the selection of the detectors was also limited to those accessible by the University of Wisconsin Medical Radiation Research Center (UWMRRC). Table 3.1 lists the potential detectors that were not used and the reasons for their omission.

Cadmium telluride (CdTe) has the advantage over HPGe detectors of being operated at room temperature. However, CdTe, along with lithium-drifted silicon [Si(Li)] detectors, are not available in large sizes and are only practical for use with photon energies up to about 200 keV [Perez-Andujar and Pibida, 2004]. This is well below the 511 keV energy-of-interest. Additionally, it was desirable to detect emissions from potential contaminants such as $^{88}$Y. $^{88}$Y is a positron emitter, and would contribute to the 511 keV peak in the coincidence-gated spectrum. Since $^{88}$Y also has gamma emissions at 898 keV and 1836 keV, the detection of these higher-energy emissions could be used to assay the potential contaminants and correct

for them. The excellent energy resolution and efficiency of the HPGe detector enabled it to accomplish this.

To accommodate the size of the potential sources (e.g., a vial containing $^{90}$Y microspheres), it was necessary to have an opposing detector with a large enough diameter that the source being measured was contained within the field-of-view (FOV) of the detection system. Ideally, this detector would have an intrinsic efficiency that approached 100 % so the detection system was only limited by the efficiency of the HPGe detector. A gamma camera with the collimator removed would fulfill the need for a large diameter. However, NaI crystals in gamma cameras are typically no thicker than 2.54 cm (1 in), which would result in a poor intrinsic efficiency for 511 keV photons. Lanthanum-halide detectors, such as $LaCl_3$ and $LaBr_3$, have higher cross sections to 511 keV photons than NaI, but are not available in large sizes. BGO detectors also have a higher cross section to 511 keV photons than NaI. BGO block detectors from a decommissioned PET machine were available. These detectors could have been mounted together to create a large detector with the necessary area. However, the potential benefits were greatly outweighed by the extensive machining and wiring that would have been required. Due to these associated complexities, this option was omitted in favor of the selected NaI detector.

The HPGe detector used in this research was a reverse electrode coaxial detector model GR2519 manufactured by CANBERRA (Meriden, CT). The detector was coupled with a transistor-reset preamplifier model 2101NSL, also manufactured by CANBERRA. The germanium crystal had a 52 mm diameter and a 51 mm thickness and had a 25 % relative efficiency. The detector had a 0.5 mm thick beryllium entrance window. The NaI detector used in this research was a Packard model 3216. The NaI crystal had a 20.3 cm (8 in) nominal diameter and a 10.2 cm (4 in) nominal thickness. It was held in an aluminum cover and was coupled to three PMTs. A Keithley (Cleveland, Ohio) model 247 high voltage supply was used to apply a +1000 V potential across the PMTs.

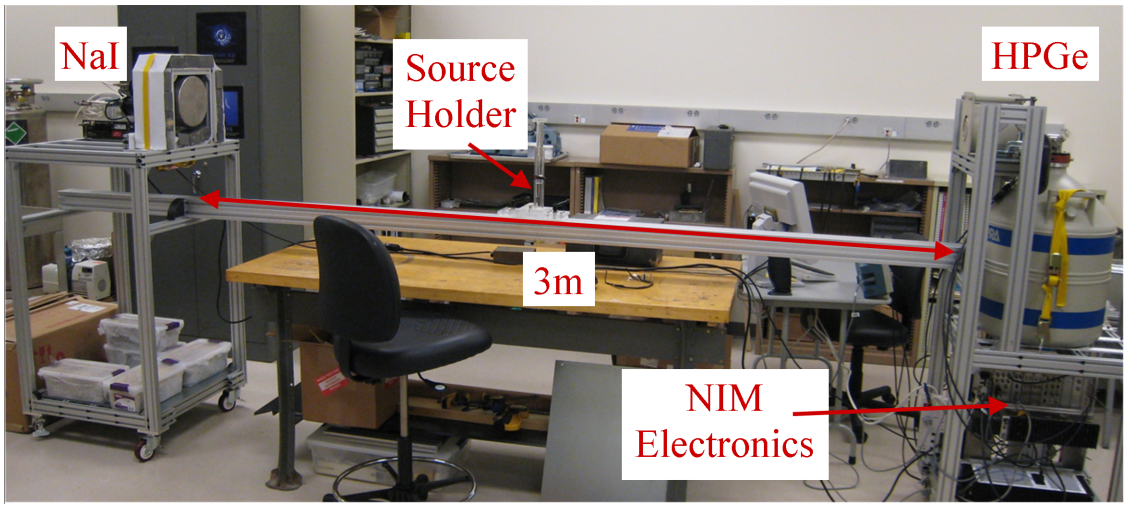


Figure 3.1: Photograph of the experimental setup of the coincidence detection system.

### 3.2.2 Detector mounts and stands

As noted in Section 3.1, the experimental setup needed to be able to reproducibly position the detectors, as well as accommodate detector shielding and the NIM electronics needed for signal processing. The detector mounts for the NaI and HPGe detectors were constructed from aluminum extrusion (30 mm profile series) manufactured by Bosch Rexroth Corporation (Charlotte, North Carolina). Figure 3.1 shows a photograph of the experimental setup. The setup was designed to limit the number of scattered and bremsstrahlung photons reaching each of the detectors. Each detector was surrounded by lead shielding. Lead blocks were stacked around the NaI detector on a constructed aluminum frame. Each block was approximately 5 cm (2 in) thick. The blocks were held to the frame with a ratchet tie-down strap. A CANBERRA model 717 shield was used with the HPGe detector. This shield provided approximately 2.5 cm (1 in) of lead shielding and had a brass-lined internal cylinder to prevent lead fluorescence x-rays from reaching the detector. The 717 shield was held on a shelf of the aluminum detector stand. There was a 3 m separation between the detectors that was spanned by an 80 mm x 80 mm aluminum beam. This beam provided a track for the source holder to position a source between the detectors.

### 3.2.3 Source holder

The source holder for the CDS needed to be able to reproducibly position the source, translate the source in three dimensions, and limit the bremsstrahlung production from beta-emitting sources (such as $^{90}$Y). Figure 3.2 shows the source holder that was designed and constructed to meet these requirements. It was made of polymethyl methacrylate (PMMA) because PMMA is relatively inexpensive, very machinable, and has a low average atomic number ($Z$). The low $Z$ of PMMA achieved the requirement of limiting the bremsstrahlung production, which is proportional to $Z^2$ [Attix, 2004]. The source holder was able to be moved along the aluminum beam's channels on nylon slides and be locked into place by tightening two adjustable handles that were attached to Bosch Rexroth T-blocks in the channel of the aluminum beam. Lateral movement of the source was accomplished by moving the base of the holder along a milled channel. This channel had a length of approximately 22.8 cm (9 in), thus the source could be translated through the entire FOV of the detection system. The base of the source holder was held in place by tightening the bolt that passes through the base. Vertical movement was accomplished by translating the PMMA rod through the PMMA tube. The rod was held in place with a set screw that could be moved along the milled channel of the vertical tube. The rod was removable so the source holder could be modified to accommodate various source geometries. Figure 3.2 shows the rod with a platform attached to the top.

### 3.2.4 Alignment of the detectors and the source

The detector mounts were designed to place the central axis of the detectors at approximately the same height. A water level was used to confirm the height of the detectors, and shims were used to finely adjust of the height of the HPGe detector central axis to match that of the NaI detector's central axis. A digital protractor was used to confirm that the outer housings of both detectors were level. Next, the central axes of the detectors

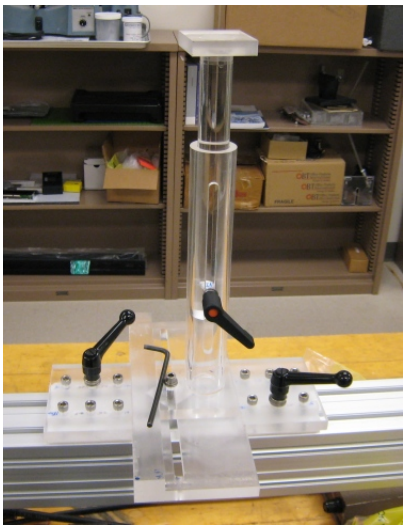

Figure 3.2: The constructed source holder for the CDS with the platform holder.

were aligned to be collinear and parallel to the long axis of the spanning beam. This was completed using a Robotoolz (Mountain View, CA) model RT-7610-5 self-leveling laser. A mount was constructed so the self-leveling laser could be held in the source holder (see Figure 3.3). The laser marks were adjusted to point at the center of each detector face. The source holder was then translated along the beam from one detector to the other. The positions of the detectors were adjusted until there was less than $\pm 2\,\mathrm{mm}$ of offset in the position of the laser marks on the front faces of the detectors as the laser was translated across the aluminum spanning beam.

In order to correctly position a source in the source holder at the height of the central axes of the detectors, a fan laser was mounted on the HPGe detector stand at the height of the central axes of the detectors. A water level was used to confirm the height of the fan beam and adjust the tilt. For future consistency checks of the position of the fan beam, a scribe line was placed on the HPGe detector shielding. Additionally, bolts were attached to the NaI detector mount such that a jig could be placed on the bolts and across the NaI detector face to confirm the height and tilt of the fan beam. Figure 3.4 shows a photograph of the fan laser used for vertical positioning of sources.

Figure 3.3: The Robotoolz self-leveling laser (in source holder mount) used to position the detectors.

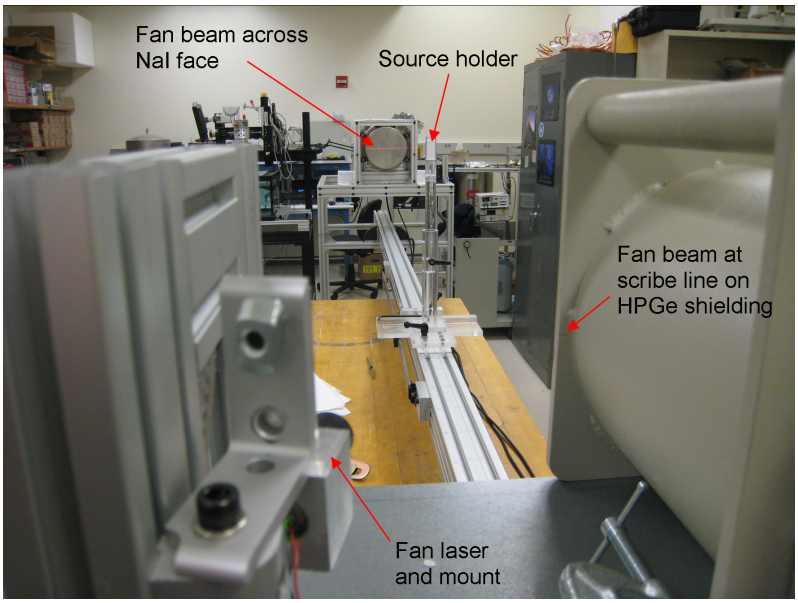


Figure 3.4: The fan laser mounted on the HPGe detector stand and the fan beam through the CDS FOV.

Since the detectors were aligned to be parallel to the aluminum spanning beam, lateral alignment of a source was achieved by default as long as the post of the source holder was centered in the source holder base. A scribe line marked this location for accurate placement of the source holder post. For positioning the source holder at different locations along the spanning beam, scribe marks were placed every 10 cm on the beam starting at the front face of the HPGe detector.

### 3.2.5 Tuning NIM electronics

For the measurement of energy and timing spectra, a series of NIM electronics was set up as shown in the electronics block diagram in Figure 3.5. Each detector was followed by the typical electronics series of a preamplifier followed by an amplifier. The gain for the HPGe amplifier (CANBERRA model 2024 Fast Spectroscopy Amplifier) was adjusted such that the collected spectra energy ranged from approximately 0 keV to 2000 keV. The gain for the NaI amplifier (ORTEC model 460 Delay Line Amplifier) was adjusted such that the collected spectra energy ranged from approximately 0 keV to 1500 keV. Following each detector's respective amplifier, the electronics chain was split into two separate series. One of the these series processed the timing information and the other processed the energy information. These are described separately in the subsequent sections. All of the NIM electronics settings are provided in Appendix A for reference.

#### 3.2.5.1 Timing signal

Following each detector's amplifier, an ORTEC model 551 Timing Single-Channel Analyzer (TSCA) was used to pick off the timing information from the bipolar output of the amplifier. For the initial tuning of the timing of the electronics, a $^{22}$Na calibration source was placed 1.5 m from both detectors (i.e., centered between the detectors). The resulting true-coincident signal was viewed using an oscilloscope and was used to adjust the timing

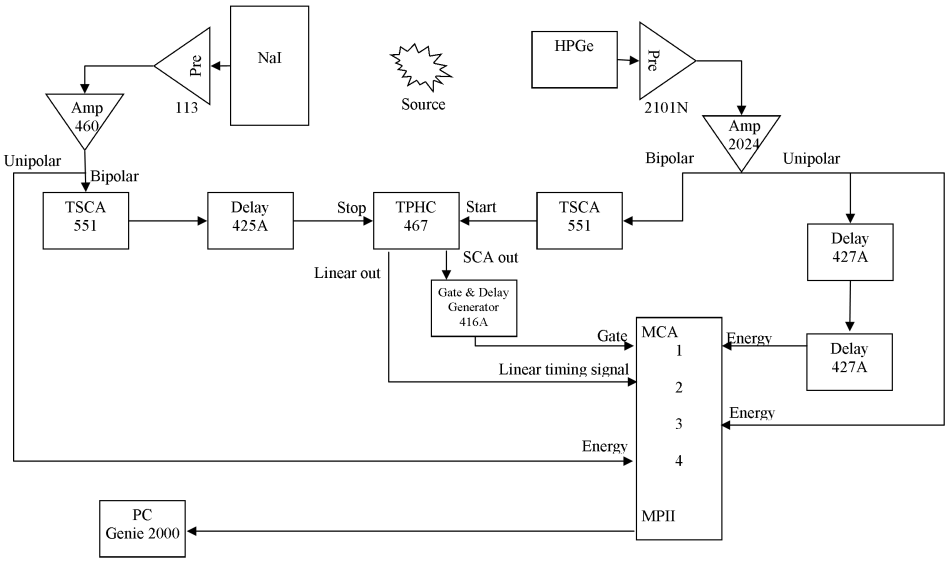


Figure 3.5: The electronics block diagram of the coincidence detection system.

delay of the NaI electronics series. The delay was adjusted so the NaI timing signal from the TSCA arrived at the stop input of the ORTEC Time-to-Pulse-Height Converter (TPHC) approximately 250 ns after the HPGe signal arrived at the start input. The height of the linear output pulse from the TPHC was proportional to the time difference between the start and stop inputs. The linear timing signal was sent to the CANBERRA Multiport II (MPII) multichannel analyzer (MCA) to bin the signal into the timing spectrum. The timing spectrum was collected and analyzed with CANBERRA Genie$^{TM}$ 2000 software. To minimize the random coincidence count rate, as defined in Equation 2.10, it was important to optimize the timing resolution of the CDS (i.e., to minimize the width of the timing spectrum). The full-width at half-maximum (FWHM) of the timing spectrum peak was minimized by adjusting the pole-zero potentiometer on each amplifier and the timing walk potentiometer on each TSCA. The measured timing spectrum of the CDS is shown in Figure 3.6. The non-symmetric shape of the peak was due to the difference in the timing properties of the HPGe and NaI detectors. The FWHM of the timing peak was approximately 90 ns and the full width is approximately 250 ns. The timing window was set with the SCA func-

tion of the TPHC to encompass the timing peak. The TPHC SCA output was sent to an ORTEC model 416A Gate and Delay Generator. The coincidence gate signal was then sent to an input on the MPII MCA to gate the incoming energy signal from the HPGe detector.

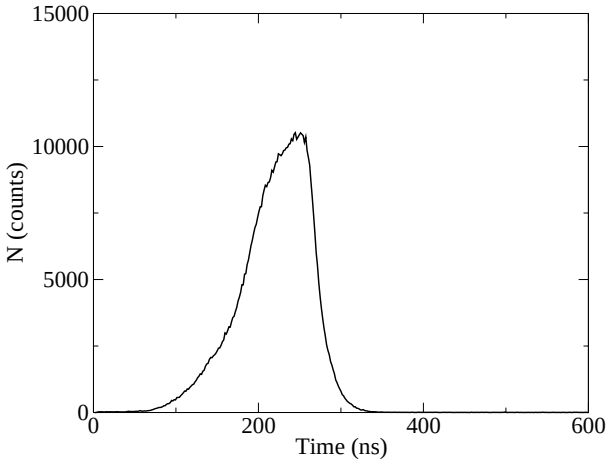


Figure 3.6: The timing spectrum obtained with the coincidence detection system using a $^{22}$Na source. The timing resolution (FWHM) was found to be 90 ns.

#### 3.2.5.2 Energy signal

The ungated signals from both the HPGe detector and the NaI detector were able to be collected simply by connecting the unipolar outputs of the respective amplifiers to inputs on the MPII MCA (as seen in Figure 3.5). However, to gate the HPGe energy signal by the coincidence-gated signal, the energy signal had to be delayed such that it arrived at the MPII MCA at the same time as the gate signal. Following adjustment of the coincidence gate signal (i.e., the timing signal), delays of the energy signal were set such that the energy signal could be gated by the coincidence signal. This was completed using the same $^{22}$Na source setup. Energy windows were set at the respective TSCAs for each of the detectors. The energy window set for the HPGe TSCA was from 100 keV to 615 keV. The energy window set for the NaI TSCA was from 100 keV to 720 keV. Because of the use of the MPII MCA, which has six inputs, this experimental setup allowed for the simultaneous collection

of the coincidence-gated HPGe energy spectrum, the ungated HPGe energy spectrum, the NaI energy spectrum, and timing spectrum. The MPII MCA had an ADC conversion gain of 8192 for energy inputs from the HPGe detector, 4096 for the energy input from the NaI, and 512 for the timing input from the TPHC. An energy calibration was required to correlate the channel number in the Genie 2000 software with the photon energy.

### 3.2.6 Energy calibration

An energy calibration was completed for each energy input of the MPII MCA. Inputs from the HPGe and NaI detectors were calibrated using different methods. Inputs from the HPGe detector were calibrated with a multinuclide source from Eckert and Ziegler (Valencia, CA) using energy lines from the following isotopes: $^{210}$Pb (47 keV), $^{241}$Am (60 keV), $^{109}$Cd (88 keV), $^{57}$Co (122 keV), $^{137}$Cs (662 keV), $^{60}$Co (1173 keV and 1333 keV), and $^{88}$Y (898 keV and 1836 keV). Additionally, a $^{22}$Na source was used to obtain peaks at 511 keV and 1275 keV. The NaI detector did not have the energy resolution needed to resolve many of the adjacent peaks present with the multinuclide source. Also for this work, the only peak-of-interest from the NaI detector was at 511 keV. So a $^{22}$Na source (511 keV and 1275 keV) was used for the energy calibration of the NaI detector input. A peak locate analysis (described in detail in Section 3.2.7.1) was completed on the resulting spectra using Genie 2000 software to determine the centroids of the peaks. The channel numbers at the centroids were entered into Genie 2000 with corresponding photon energies. Genie 2000 then fit a second-order polynomial to the data points to determine the energy for each channel number.

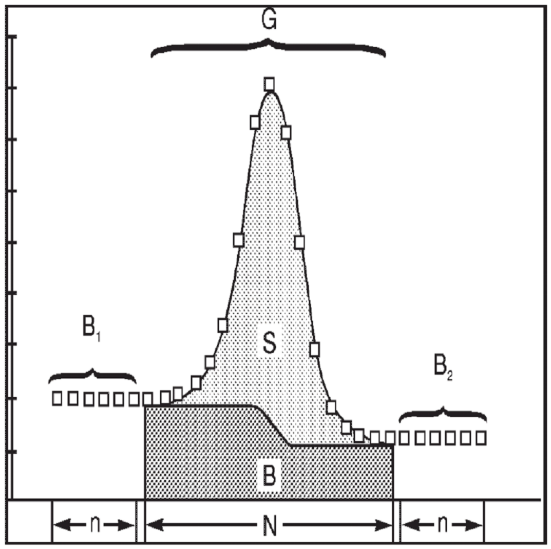


Figure 3.7: The parameters used in the step continuum calculation of peak area. Reprinted with permission from Canberra [2006].

### 3.2.7 Spectra data analysis

#### 3.2.7.1 Peak locate

Genie 2000 software from CANBERRA was used for all spectra data analysis. Prior to determining the peak area, Genie 2000 software first required determining the peak centroid location and region-of-interest (ROI). Genie 2000 accomplished this by using a generalized second difference method [Canberra, 2006]. This method was originally proposed by Mariscotti [1967]. The Genie 2000 algorithm uses a slightly modified version of the SAMPO80 version [Koskelo et al., 1981].

#### 3.2.7.2 Peak area

Genie 2000 uses a Sum/Non-Linear Squares Fit Peak Area algorithm for determining the peak area. The ROI for this algorithm is defined prior to its execution by locating the peaks present in the spectrum using the methods discussed in the previous section. The user has

the option of selecting either a linear or step continuum for this peak area analysis. Figure 3.7 shows the parameters for the step continuum calculation, which was used in this work. The net peak area, $S$, is defined by the equation,

$$S = G - B, \tag{3.1}$$

where $G$ is the number of gross counts in the ROI and $B$ is the number of counts in the continuum. $B$ is calculated using the equation,

$$B = \sum_{i=1}^{N} \left[ \frac{B_1}{n} + \frac{(B_2 - B_1)}{nG} \sum_{j=1}^{i} y_j \right], \tag{3.2}$$

where $y_j$ is the gross number of counts in channel $j$, $N$ is the number of channels in the peak ROI, $n$ is the number of continuum channels on each side of the ROI, $B_1$ is the sum of the counts in the continuum region to the left of the peak, and $B_2$ is the sum of the counts in the continuum region to the right of the peak. Equation 3.2 can be rewritten as,

$$B = \frac{N}{n} B_1 + \frac{(B_2 - B_1)}{nG} \sum_{i=1}^{N} P_i, \tag{3.3}$$

where,

$$P_i = \sum_{j=1}^{i} y_j. \tag{3.4}$$

The standard deviation of $S$ ($1\sigma$) is defined by the equation,

$$\sigma_S = \sqrt{\sigma_G^2 + \sigma_B^2}, \tag{3.5}$$

where $\sigma_G^2$ is the variance of $G$ and $\sigma_B^2$ is the variance of $B$. Since $G$ is Poisson-distributed, by definition,

$$\sigma_G^2 = G. \tag{3.6}$$

For determining $\sigma_B^2$, the components of $B$ from Equation 3.3 are considered in the equation,

$$\sigma_B^2 = (\frac{\partial B}{\partial B_1})^2\sigma_{B_1}^2 + (\frac{\partial B}{\partial B_2})^2\sigma_{B_2}^2 + (\frac{\partial B}{\partial G})^2\sigma_G^2 + \sum_{i=1}^{N}(\frac{\partial B}{\partial P_i})^2\sigma_{P_i}^2. \tag{3.7}$$

Again taking advantage of Poisson statistics, Equation 3.7 reduces to,

$$\sigma_B^2 = \frac{1}{(nG)^2}\left[(NG - \sum P_i)^2 B_1 + (\sum P_i)^2 B_2 + (B_2 - B_1)^2(\sum P_i)^2(\frac{1}{G} + \frac{1}{\sum P_i})\right], \tag{3.8}$$

so $\sigma_S$ is given by the equation,

$$\sigma_S = \sqrt{G + \frac{1}{(nG)^2}\left[(NG - \sum P_i)^2 B_1 + (\sum P_i)^2 B_2 + (B_2 - B_1)^2(\sum P_i)^2(\frac{1}{G} + \frac{1}{\sum P_i})\right]}. \tag{3.9}$$

Debertin and Helmer [1988] noted that using different peak area evaluation methods can result in different peak area values, but the quality of an analysis method depends on its reproducibility since the detector efficiency is determined using the same method. Selwyn [2007] evaluated multiple peak area analysis methods in Genie 2000 and determined that the uncertainty associated with using the various methods was 0.15 % ($k = 1$).

### 3.2.8 Confirmation of improvement over single-detector counting

Following the completion of the construction and initial setup of the CDS, it was necessary to demonstrate the ability of this newly-developed system to reduce the bremsstrahlung continuum surrounding the 511 keV peak area in a $^{90}$Y gamma spectrum to achieve reduced measurement uncertainties compared to measurements with a single HPGe detector. To test this, a $^{90}$Sr/$^{90}$Y pellet contained within an acrylic shield was placed on the source holder 1.5 m from either detector (i.e., centered between the detectors). Coincidence-gated

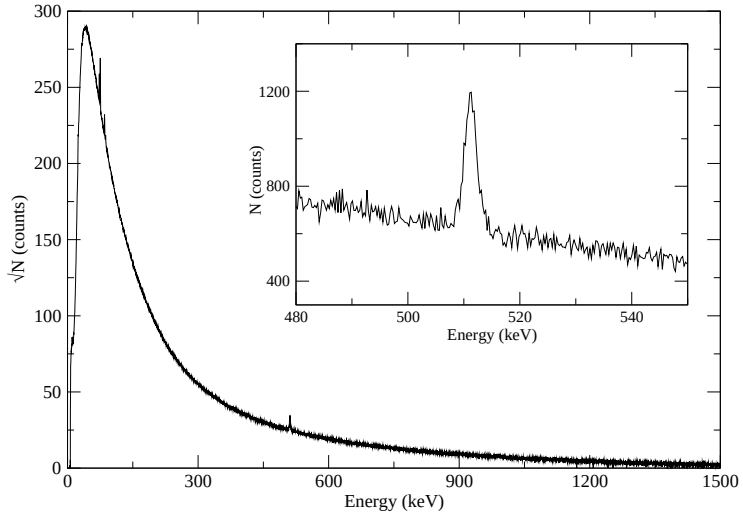


Figure 3.8: Plot of the ungated $^{90}$Sr/$^{90}$Y spectrum.

and ungated energy spectra were measured for 4 h, followed by measurement of the environmental background (EBG) (i.e., no source present) for 12 h. Annihilation photons were present in the EBG due to pair production interactions of cosmic rays [Debertin and Helmer, 1988]. All of the data were analyzed using Genie 2000 software using the analysis methods described in the Section 3.2.7.

Figure 3.8 shows the measured ungated $^{90}$Sr/$^{90}$Y spectrum after EBG subtraction. Note that the y-axis is $\sqrt{N}$. This suppression was applied for easier viewing of the spectrum. The inset (which is not suppressed) shows an enlarged view of the 511 keV peak. The peak area uncertainty was 7.9 % after EBG subtraction. The 511 keV peak area uncertainty in the EBG was 1.2 %. Figure 3.9 shows the coincidence-gated spectrum. Note that the bremsstrahlung continuum was greatly reduced. The peak area uncertainty was 1.7 %. The EBG for the coincidence-gated spectrum was found to be negligible with no counts within

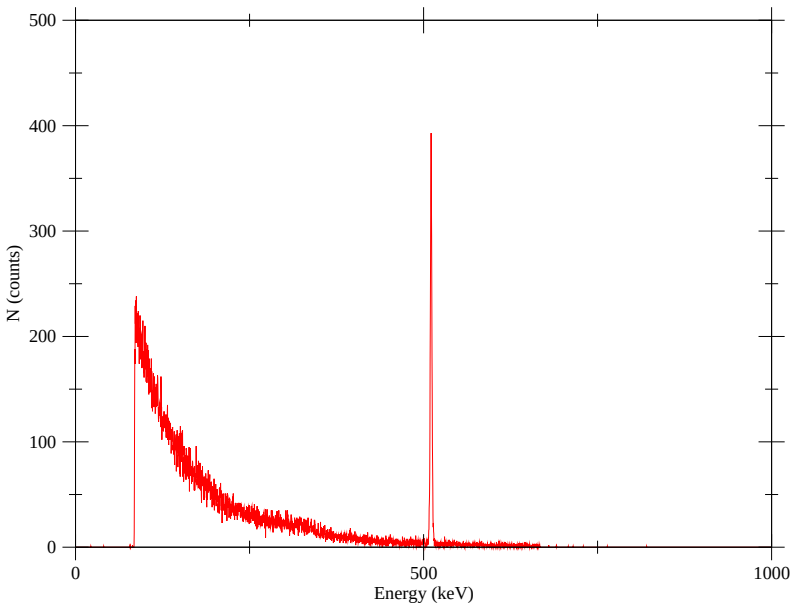


Figure 3.9: Plot of the coincidence-gated $^{90}$Sr/$^{90}$Y spectrum.

the 511 keV peak area. Due to the presence of the EBG for the ungated spectrum, Equation 3.1 for the calculation of the net peak area becomes,

$$S = G - B - E, \tag{3.10}$$

where $E$ is the number of counts above the continuum, $B$, due to the EBG. This increases the uncertainty associate with $S$ as the standard deviation of $S$ from Equation 3.5 becomes,

$$\sigma_S = \sqrt{\sigma_G^2 + \sigma_B^2 + \sigma_E^2}, \tag{3.11}$$

where $\sigma_E^2$ is the variance of $E$.

These results demonstrate the ability of the CDS to reduce the bremsstrahlung continuum present in the ungated spectrum, as well as demonstrate that the CDS does not require EBG subtraction. These factors resulted in a reduced peak area uncertainty when

compared to measurement with a single detector. Further work was required in order to use the CDS to accurately assay the activity of a $^{90}$Y or $^{90}$Sr/$^{90}$Y source. This included implementing and validating a counting losses correction and characterizing the geometric sensitivity of the system such that the optimal measurement location could be selected for a source of a given size. These requirements are described in the next sections.

## 3.3 Counting-losses correction

Counting losses can occur in photon spectrometry due to dead time and pulse pile-up. Dead time is the time after an event has occurred during which another event cannot be recorded [Knoll, 2000]. Essentially, this is a signal processing time. A common source of dead time in a photon spectrometry system is the analog-to-digital converter (ADC) of the MCA, which has a set conversion time needed to process each incoming pulse [Lindstrom and Fleming, 1995]. Pulse pile-up (or random summing) occurs when two consecutive pulses overlap when being processed by the amplifier of the detection system. Both of the signals are processed (one is not lost, as with the dead time effect), but they are combined into a single distorted pulse with a larger pulse height. This results in a single higher-energy pulse, rather than two lower-energy pulses [Gilmore, 2008]. Both dead time and pulse pile-up effects are count-rate dependent, i.e., there are more losses due to each effect with higher count rates. If the losses from either of these effects is significant, a correction must be applied to accurately quantify the results.

There are a number of methods that have been used to account for counting losses. These include: use of a live time clock, loss-free counting, pile-up rejection circuits, and use of a pulser. The concept behind a live time clock is to not include the dead time (or pulse processing time) in the calculation of the count rate of the peak-of-interest, but rather to only consider the time in which the MCA is available to receive and process a pulse (i.e., the live time) [Debertin and Helmer, 1988]. Loss-free counting refers to measurement systems

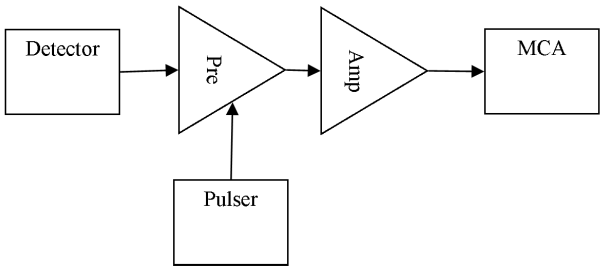


Figure 3.10: An electronics block diagram of a pulser included in a typical detector series.

that use techniques so there are no dead time losses. These include the Harms procedure in which pulses received during the dead time are still processed [Gilmore, 2008] and the virtual pulse generator technique in which the system sends virtual queries essentially asking 'if a pulse were injected at a particular time, would it be detected?' [Westphal, 1982]. Pile-up rejection circuits analyze the shape of input pulses to the amplifier. If the pulse is determined to be affected by pile-up, an off (i.e., rejection) gate is sent to the MCA to prevent the signal from being accepted. The off time of the MCA is then accounted for in the calculation of the counting losses. Live time counting and the Harms procedure work adequately for correcting for dead time, but do not account for pulse pile-up effects. The virtual pulse generator technique can account for both counting loss effects, but the peak area uncertainty can no longer be evaluated using Poisson statistics. Pile-up rejection circuits require anti-coincidence gating to reject piled-up pulses; however, the CDS requires coincidence gating at the MCA to accept coincident pulses.

The pulser method was used in this work for correcting for counting losses. This method simultaneously corrects for both dead-time and pile-up losses. The concept behind the method is relatively simple. A pulse generator is connected to the test input of a preamplifier in a typical detector-electronics series, as shown in Figure 3.10. The pulser signal is

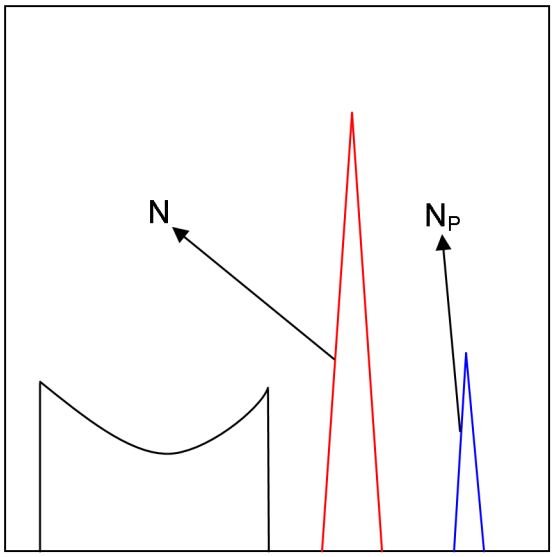


Figure 3.11: Diagram depicting a spectrum with a peak-of-interest (red) and a pulser peak (blue).

processed through the same series of electronics as the detector signal. This results in a pulser peak being present in the measured spectrum, along with the peak-of-interest. This is depicted in Figure 3.11. The assumption behind this technique is that the number of counts that are lost from the pulser peak will be proportional to the number of counts lost from the peak-of-interest. The corrected (or true) number of counts in a peak-of-interest, $N_0$, is given by the equation,

$$N_0 = N\frac{f \cdot t}{N_{\mathrm{P}}}, \tag{3.12}$$

where $N$ is the number of counts in the peak-of-interest, $f$ is the frequency of the pulser, $t$ is the counting time, and $N_{\mathrm{P}}$ is the number of counts in the pulser peak. Note that $f \cdot t$ is simply the number of injected pulses for the measurement cycle, so the multiplicative correction is simply the ratio of the number of injected pulses over the number of detected pulses. An International Atomic Energy Agency (IAEA) intercomparison [Houtermans et al., 1983] found the pulser technique to be superior to other corrections for dead time and pulse pile-

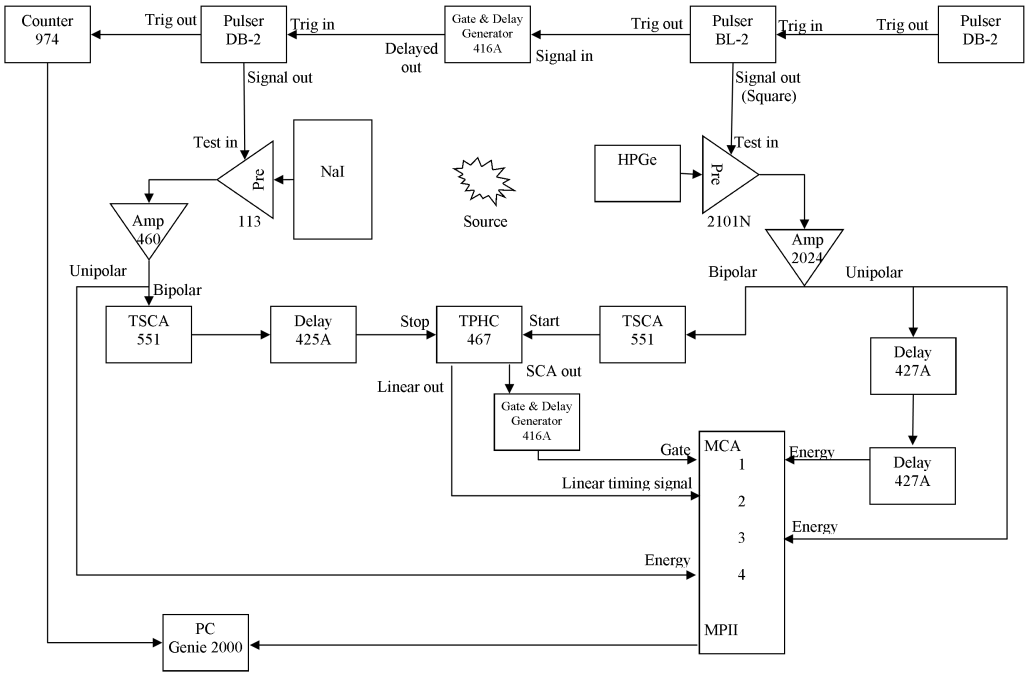


Figure 3.12: The electronics block diagram of the CDS including the series of pulsers.

up. However, the technique does have some limitations. It requires that the pulse from the pulser mimic the detector pulses as closely as possible, otherwise the pulses from the pulser will not be processed in the same manner by the pulse-shaping electronics. Additionally, the assumption that the pulser peak and peak-of-interest suffer equal fractional losses may not be valid for a pulser with a constant frequency. For a pulser with a constant frequency, the pulses from the pulser can pile-up with pulses from the detector, but will never pile-up with another pulser pulse [Gilmore, 2008]. This can result in systematic errors in the counting losses correction, but this issue can be resolved by using a random pulser [Wiernik, 1971].

### 3.3.1 Pulser series

The pulsers used in this work were two model DB-2 Random Pulser Generators and one model BL-2 Fast Tail Pulse Generator all manufactured by Berkeley Nucleonics Corporation (San Rafael, California). Because the HPGe detector pulses and the NaI detector pulses have

different shapes, each detector had a separate pulser. The model BL-2 pulser was attached to the test input of the HPGe detector's model 2101N preamplifier. Because the model 2101N is a transistor reset preamplifier, a square-like wave was used for the input pulse [Gilmore, 2008]. One of the model DB-2 pulsers was attached to the test input of the NaI detector's model 113 preamplifier. The methodology for incorporating a pulse generator described by Gilmore [2008] was used to match the pulser signal to the detector signal. This included adjusting the decay time of the pulser until the output from the amplifier (viewed using an oscilloscope) had a good return of the pulser pulses to baseline. Following matching of the pulser signals to the detector signals, a separate model DB-2 random pulser was implemented in the electronics series to trigger the other two pulsers. This allowed the injection of the pulses into the respective detectors to be correlated in time. A delay was used to adjust the difference in time between the injected pulses such that this difference was within the true-coincidence timing window. Figure 3.12 is an updated version of Figure 3.5 that includes the series of pulsers. Figure 3.12 also shows the computer-controlled counter that is discussed in the next section. A photograph of the NIM electronics used in this work is shown in Figure 3.13.

### 3.3.2 Computer-controlled counter

Because a random pulser was used to trigger the other pulsers rather than a constant frequency pulser, the number of pulses injected into the system had be counted. This was accomplished using an ORTEC model 974 computer-controlled Quad Counter/Timer. As seen in Figure 3.12, the output from the last pulser in the series was connected to one of the inputs of the 974 counter.

Consecutive, repeated measurements of a source were often completed with the CDS. Genie 2000 software had the capability of acquiring consecutive measurements in which the user could set the counting time and the number of measurements to be completed. However,

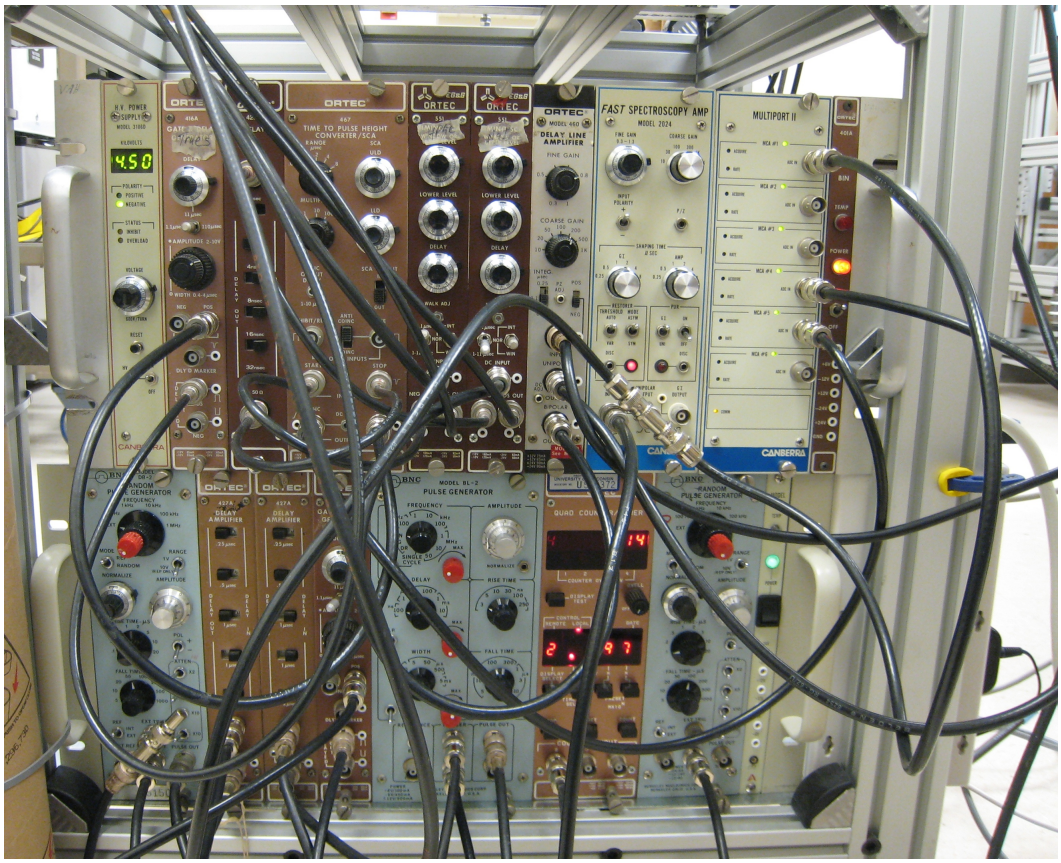


Figure 3.13: Photograph of the NIM electronics used in this work.

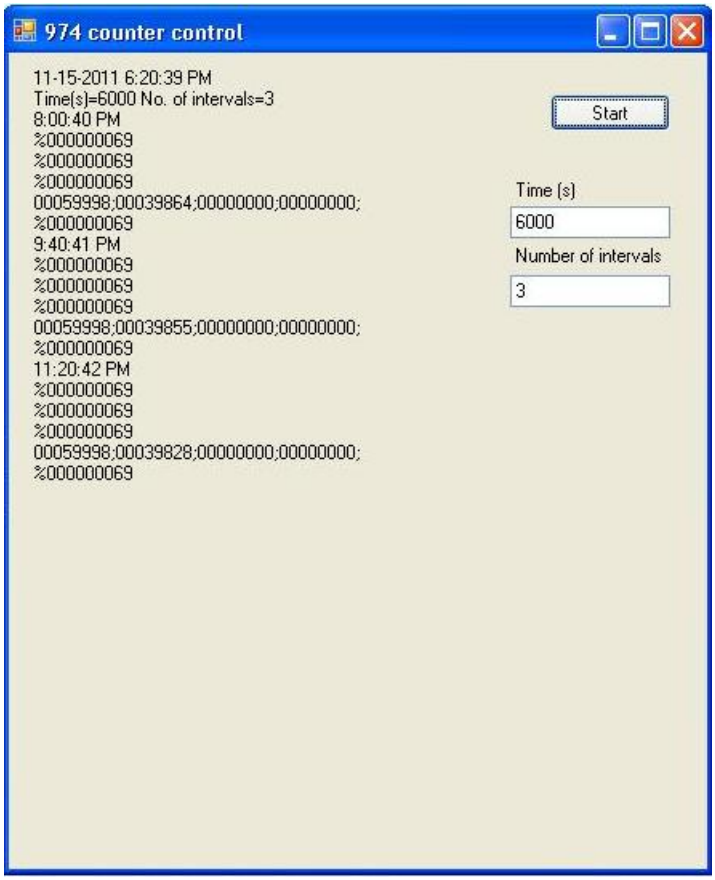


Figure 3.14: A screenshot of the 974 counter control window.

this ability was not inherent to the 974 counter, but was developed through its computer-controlled functionality. The 974 counter was connected to the control computer via an RS-232 serial cable. A program was developed in Visual Basic Express 2008 (Microsoft, Redmond, Washington) to allow the user to set the counting time and the number of measurement intervals for the 974 counter. The program output provided the start time for each measurement and the number of counts recorded by the 974 counter for that measurement. A text file report of this information was also created. A screenshot of the program window is shown in Figure 3.14 and the program code is provided in Appendix B.1.

### 3.3.3 Correction validation

Two studies were completed to test the validity of the counting-losses correction. Both involved using a beta-emitting source to increase the count rate while a $^{22}$Na source was being measured. These setups mimicked the measurement conditions with a $^{90}$Y microsphere source, in which a high-energy bremsstrahlung continuum would be present. Two $^{22}$Na calibration sources with respective reference activities of 2.543 MBq $\pm 0.41\,\%$ ($k = 1$) and 254.7 kBq $\pm 0.41\,\%$ ($k = 1$) were used in these validation studies. The first beta-emitting source was a $^{90}$Sr/$^{90}$Y pellet and the second was a $^{90}YCl_3$ solution.

#### $^{90}$Sr/$^{90}$Y pellet

For this study, the higher activity $^{22}$Na source was used to complete an efficiency calibration of the CDS. From this calibration, the activity of the other $^{22}$Na source was determined from measurements with the $^{90}$Sr/$^{90}$Y pellet present. The cylindrical $^{90}$Sr/$^{90}$Y pellet had a length of 2.3 mm and a diameter of 0.4 mm. The pellet was contained in a stainless steel capsule and had an approximate activity of 400 MBq. For measurements, the lower activity $^{22}$Na source was placed in the source holder of the CDS. The $^{90}$Sr/$^{90}$Y pellet was contained

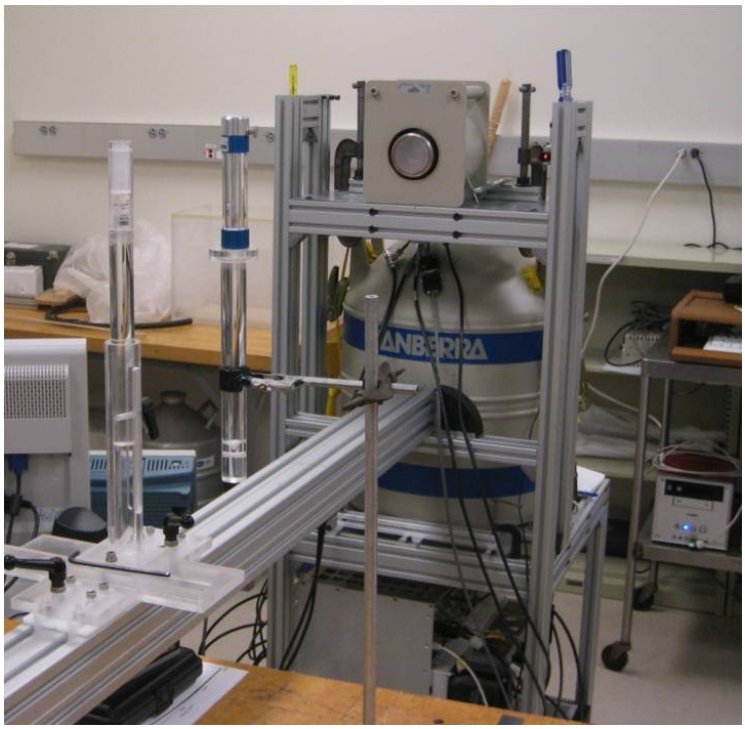

Figure 3.15: Photograph of the experimental setup used in the validation of the pulser correction for counting losses.

in a PMMA shield and placed on a holder that was laterally offset from the $^{22}$Na source by approximately 13 cm, as seen in Figure 3.15. This offset ensured the $^{90}$Sr/$^{90}$Y source was outside the FOV of the CDS so the IPP component of $^{90}$Y decay could not contribute to the gated coincidence signal. Three consecutive 8 h measurements were completed with this experimental setup at distances of 60 cm, 100 cm, 120 cm, 150 cm, and 200 cm from the HPGe detector. Dead time and pulse pile-up are independent of source-to-detector distance [Debertin and Helmer, 1988], but repeating these measurements at the various distances from the HPGe detector provided different count rates. For the efficiency calibration, three consecutive 6000 s measurements were completed of the higher activity $^{22}$Na source at each of the measurement distances. Equation 2.9 was then used to determine the activity of the lower activity $^{22}$Na source.

### $^{90}YCl_3$ solution

For this study, a base-line count rate was determined with the higher activity $^{22}$Na source along. This value was then compared to counting-loss-corrected count rates of the same source determined from repeated measurements with a $^{90}YCl_3$ solution present. The $^{90}YCl_3$ solution from Perkin Elmer (Waltham, Massachusetts) had a starting activity of approximately 3.0 GBq. The measurement setup was similar to the setup with the $^{90}$Sr/$^{90}$Y pellet, with the $^{90}YCl_3$ solution placed on a stand laterally offset from the $^{22}$Na source by 13 cm and outside the FOV of the CDS. All measurements with this setup were performed at 120 cm from the HPGe detector. The base-line count rate was determined by taking ten 6000 s measurements of the higher activity $^{22}$Na source. Six of these measurements were completed prior to measurements with the $^{90}YCl_3$ solution and four were completed after. Sixty-five consecutive 6000 s measurements were completed with the $^{22}$Na and the $^{90}YCl_3$ solution present. The measured count rates were corrected for counting losses using the pulser method.

Table 3.2: Determined activity of a $^{22}$Na calibration source while a $^{90}$Sr/$^{90}$Y source was present during measurement compared to the known activity of 254.7 kBq.

| Distance (cm) | Activity (kBq) | Diff. from Ref. (%) | Average counting loss correction |
|---|---|---|---|
| 60 | 252.9 | -0.71 | 1.097 |
| 100 | 255.3 | 0.23 | 1.058 |
| 120 | 254.4 | -0.12 | 1.057 |
| 150 | 256.6 | 0.76 | 1.061 |
| 200 | 253.8 | -0.34 | 1.110 |

### 3.3.4 Results

#### $^{90}$Sr/$^{90}$Y pellet

The determined activities of the lower activity $^{22}$Na source at the various locations from the HPGe in the CDS are shown in Table 3.2. Percent differences from the known activity of 254.7 kBq are also given. All of the determined activities were within 0.76 % of the known activity, and all percent differences were within the uncertainty associated with the measurements. Table 3.2 also provides the average counting-losses correction that was applied for each measurement location. These corrections ranged from 5.7 % to 11 %. This demonstrates the ability of the implemented series of pulsers to accurately correct for counting losses with the CDS.

#### $^{90}YCl_3$ solution

Figure 3.16 shows a plot of the counting-loss-corrected count rates determined from consecutive measurements of the $^{22}$Na source with the $^{90}YCl_3$ solution present. Note that the plot is initially not flat, as the corrected count rate decreases with measurement number. This indicates that the counting-losses correction was initially over-correcting the count rate and that the over correction was reduced as the count rate decreased due to the $^{90}YCl_3$ source decay. The reasons for this effect are not entirely understood, but are most likely due to the pulser pulses not being processed in the same fashion as the detector pulses at these higher count rates. This seems to result in a greater number of lost pulser pulses, which

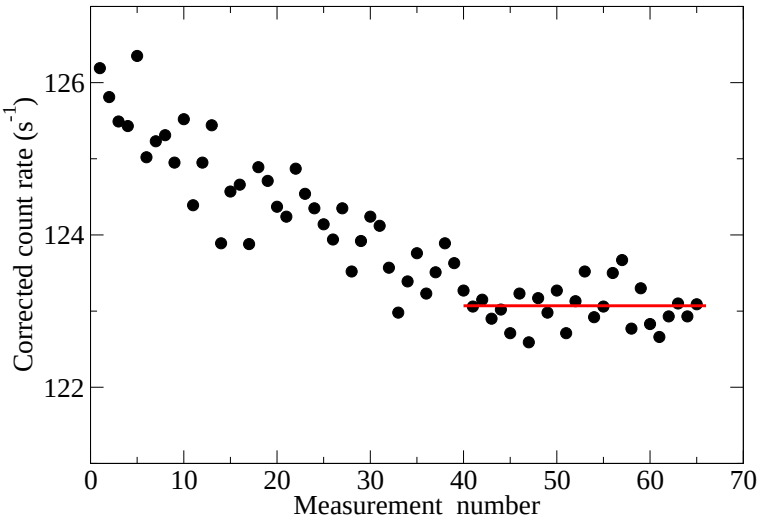


Figure 3.16: Sequential plot of corrected count rate for each measurement completed with the $^{22}$Na standard source and the Perkin Elmer $^{90}YCl_3$ solution. The red line represents a linear fit to the flat region of the data.

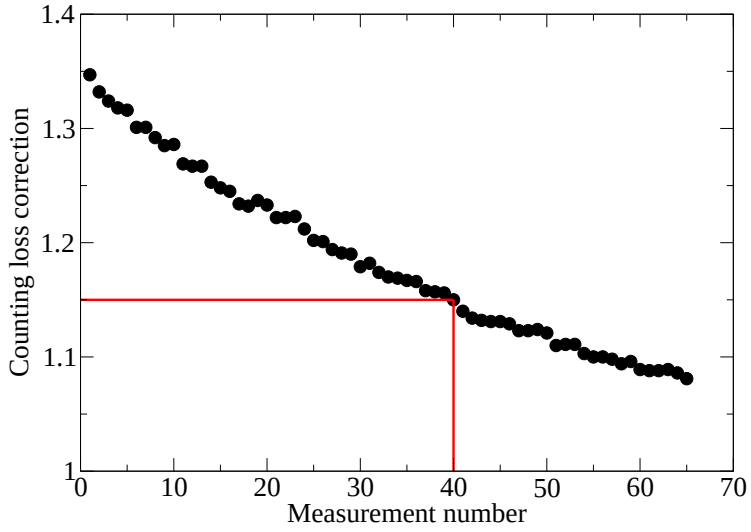


Figure 3.17: Sequential plot of the applied multiplicative counting-losses correction for each measurement with the $^{22}$Na standard source and the Perkin Elmer $^{90}YCl_3$ solution. The red line shows that measurement 40 (the beginning of the flat region) corresponds to a counting loss correction of 1.15.

results in the over correction. Near measurement number 40, the plot appears to flatten. A linear trendline was fit to the data after measurement number 40. This line had a slope of $-0.0005$, which validated that this region had a flat response. This flat response indicated that the counting-losses correction for each measurement was correcting the count rate to a common value, which is desired. The average corrected count rate in this flat region was $123.1\,\mathrm{s}^{-1}$, which is within 0.98 % of the calculated base-line value of $121.9\,\mathrm{s}^{-1}$.

Figure 3.17 shows a plot of the applied counting-losses correction factor for each consecutive measurement. Due to over-correction seen in Figure 3.16, it was necessary to create a cut-off value for the counting-losses correction, above which data will be rejected due to the observed over-correction effect. As the linear region started at measurement number 40, the associated counting losses correction was selected as the cut-off value. As indicated by the red line in Figure 3.17, this counting-losses correction is 1.15. Future measurements with counting losses determined to be higher than 15 % will be rejected.

## 3.4 Characterization of geometric sensitivity

Cherry et al. [2003] and Paans et al. [1978] discussed the loss of spatial resolution in a two-detector annihilation coincidence detection system (see Figure 3.18(a)) as a point source is moved from the midplane of the detectors toward the face of one of the detectors. This effect is illustrated in Figure 3.18(b), where the FWHM is increased as the source is moved closer to one of the detectors. This effect is undesirable in positron emission tomography (PET), where the loss in spatial resolution leads to the inability to localize the positron emitter within the patient. However for this work, this loss of geometry sensitivity is desirable in the circumstance that source-of-interest and the efficiency calibration source do not have the same geometry. For example, if the calibration source is more line-like and the source-of-interest is more point-like, this could lead to an inaccurate determination of the the source-of-interest's activity if the measurement location has a high geometric

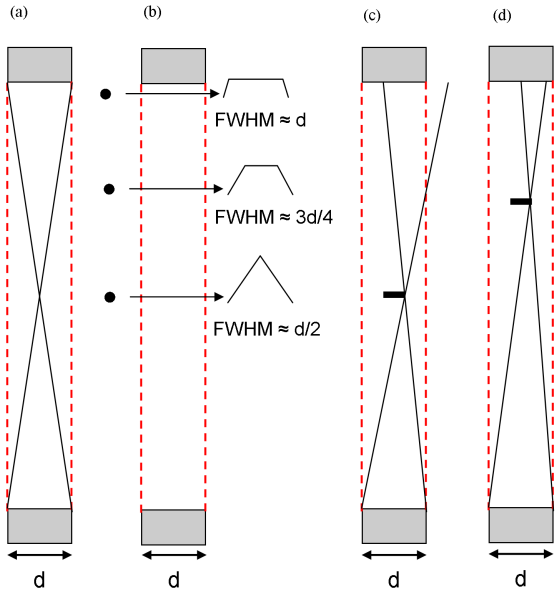


Figure 3.18: Schematic of the geometry associated with a two-detector annihilation coincidence detection system.

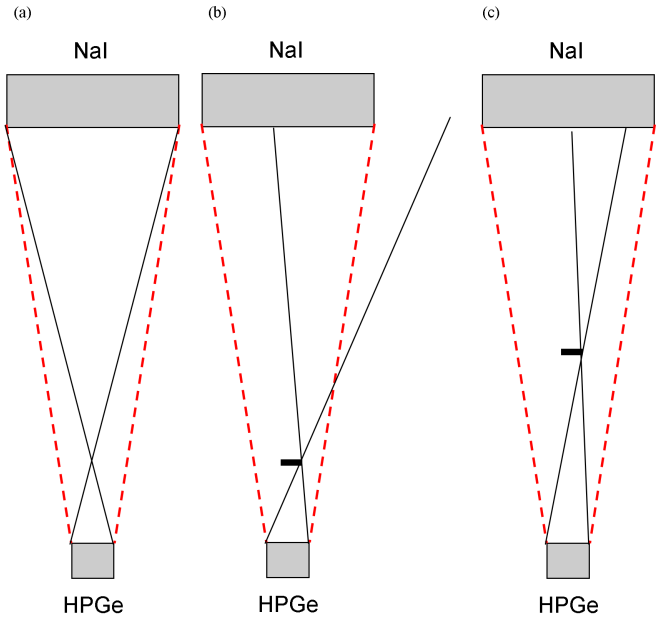


Figure 3.19: Schematic of the geometry associated with the CDS.

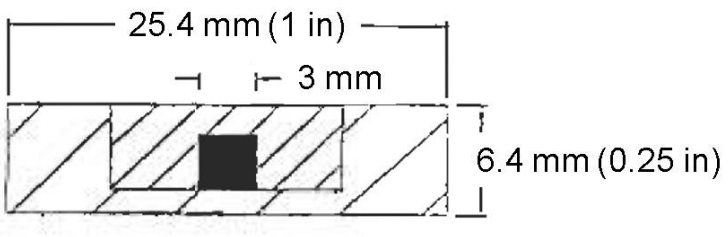


Figure 3.20: Schematic of a typical spot marker with dimensions.

sensitivity due to the detection efficiency fall-off across the length of the elongated source. This is illustrated in Figure 3.18(c). The optimal source location for measurements with sources with different geometries is one that is insensitive to these differences, as shown in Figure 3.18(d), where measurement positions offset from the midplane have less geometric sensitivity. Note also from Figure 3.18(d), that the loss of geometric sensitivity also results in a loss of detection efficiency.

Figure 3.19 shows a schematic depicting the geometry of the CDS. Due to the unmatched size of detectors in the CDS, the point of the highest geometric sensitivity (and detection efficiency) is closer to the HPGe rather than at the midplane of the detectors (Figure 3.19(a)). As the source position is moved away from the point of maximal response (Figure 3.19(b)), the geometric sensitivity is reduced (Figure 3.19(c)). This section describes the geometric characterization of the CDS. This characterization will provide the ability to select the optimal source location for measurements with the CDS.

### 3.4.1 Spot markers

The ideal source for performing the geometric characterization of the CDS was a point-like, positron-emitting source. Spot markers are point-like sources used in nuclear medicine departments as fiducial markers during imaging scans. The construction of a spot marker consists of a central active cylindrical core within two larger PMMA cylinders. Adhesive is used to hold the two larger cylinders together and seal the source. A typical constructed spot

Table 3.3: Comparison of the physical properties of $^{22}$Na and $^{68}$Ge/$^{68}$Ga for their use in the geometric characterization of the CDS.

| | Radionuclide | |
|---|---|---|
| Physical property | $^{22}$Na | $^{68}$Ge/$^{68}$Ga |
| Half-life | 2.6 y | 271 d |
| Positron branching ratio | 90 % | 89 % |
| Energy$_{\beta^+\text{max}}$ | 550 keV | 1900 keV |
| Maximum positron range in PMMA | 1.7 mm | 8.0 mm |
| Major $\gamma$ emissions (branching ratio) | 1.275 MeV (99.9 %) | 1.077 MeV (3.3 %) |

marker has a nominal diameter of 25.4 mm (1 in) and a nominal height of 6.4 mm (0.25 in). The active core typically has a nominal diameter and height of 3 mm. A schematic of a spot marker with dimensions is shown in Figure 3.20. The most common positron-emitting radionuclides available in spot markers are $^{22}$Na and $^{68}$Ge. Technically, $^{68}$Ge is not a positron emitter. It decays via electron capture to $^{68}$Ga, which is a positron emitter. Due to the much longer half-life of $^{68}$Ge compared to $^{68}$Ga (271 d versus 68 min, respectively), $^{68}$Ge and $^{68}$Ga are present in secular equilibrium. For the purposes of discussion, this work will refer to $^{68}$Ge/$^{68}$Ga simply as $^{68}$Ge.

These radionuclides have physical properties that provide both advantages and disadvantages for this work. Table 3.3 compares the relevant physical properties of $^{22}$Na and $^{68}$Ge. Both radionuclides have half-lives that are adequately long to be useful. The positron branching ratios are essentially the same, and so provide no advantage for either radionuclide. However, the maximum positron energy for $^{68}$Ge is higher than that of $^{22}$Na (1900 keV versus 550 keV, respectively). This results in the maximum positron range in PMMA for $^{68}$Ge being more than four times greater than that for $^{22}$Na. This results in a $^{68}$Ge spot marker being less point-like compared to a $^{22}$Na spot marker. Both $^{68}$Ge and $^{22}$Na also have gamma emissions at 1.077 MeV and 1.275 MeV, respectively, but the branching ratio for the gamma emission from $^{22}$Na is much higher at 99.9 % compared to 3.3 % for $^{68}$Ge. These gamma emissions can result in true coincidence summing of the gamma emission and

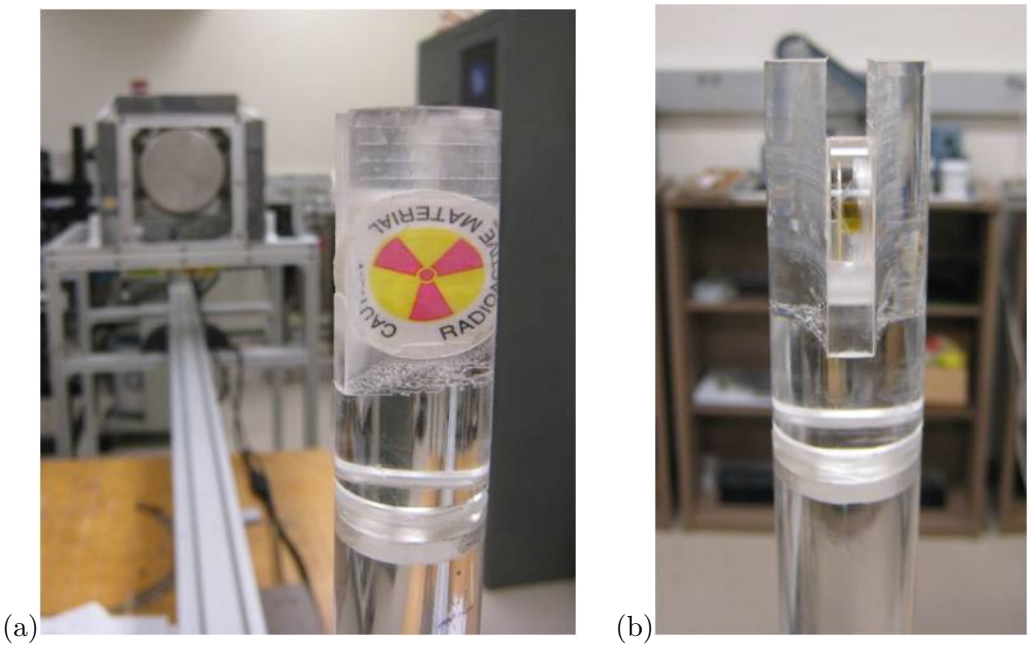


Figure 3.21: Photographs from the front (a) and side (b) of the source holder constructed for the spot marker source.

one of the 511 keV annihilation photons when the source is near one of the detectors. This results in counting losses from the peak-of-interest.

For this work, both a $^{22}$Na and a $^{68}$Ge spot marker were used. The $^{22}$Na spot marker (model BM03-22L) and the $^{68}$Ge spot marker (model BM03-68L) were both manufactured by RadQual, LLC (Weare, New Hampshire). For both of these spot markers, the active core was constructed of PMMA. Because the $^{22}$Na spot marker was more point-like due to its lower positron energy, it was used for the majority of the geometric characterization. Measurements of the $^{22}$Na spot marker that were completed near the HPGe detector were compared to measurements with the $^{68}$Ge spot marker to assess the losses with the $^{22}$Na source due to true coincidence summing.

### 3.4.2 Source holder

As described in Section 3.2.3, a source holder was created to reproducibly hold and translate a source throughout the FOV of the detection system. An attachment specifically for the spot markers was designed and constructed. Photographs of the constructed holder are shown in Figure 3.21. The holder consisted of a 25.4 mm (1 in) diameter PMMA rod with a 6.4 mm (0.25 in) thick channel. A cradle with a cutout arc [radius = 12.7 mm (0.5 in)] was placed at the bottom of the channel. The arced cradle served to center the spot marker in the holder. The PMMA surrounding the spot marker in this holder provided enough material to stop all emitted positrons and allow them to annihilate.

### 3.4.3 Measurements

For measurements of the lateral geometric sensitivity, the $^{22}$Na spot marker was placed in the holder and stepped across the FOV of the CDS. At each location, the coincidence-gated spectrum was collected three times for 500 s each. The spectra were analyzed with Genie 2000 using the techniques described in Section 3.2.7, and the average count rate was calculated for that location. This count rate was corrected to a common reference date and corrected for counting losses using the pulser method described in Section 3.3. The process of stepping the source across the FOV of the CDS was completed at distances of 50 cm, 60 cm, 80 cm, 100 cm, 120 cm, 150 cm, and 200 cm from the HPGe detector. This process was repeated at 60 cm and 120 cm from the HPGe detector with the source stepped vertically through the FOV to confirm that the lateral and vertical geometric sensitivities were symmetric. Additional measurements were completed with no lateral or vertical offset at 20 cm, 30 cm, 40 cm, 70 cm, 90 cm, 110 cm, and 250 cm from the HPGe detector. Measurements with the $^{68}$Ge source were completed at 20 cm, 30 cm, 40 cm, 50 cm, 60 cm, 70 cm, 80 cm, 100 cm, 120 cm, 150 cm, 200 cm, and 250 cm from the HPGe detector with no vertical or lateral offsets.

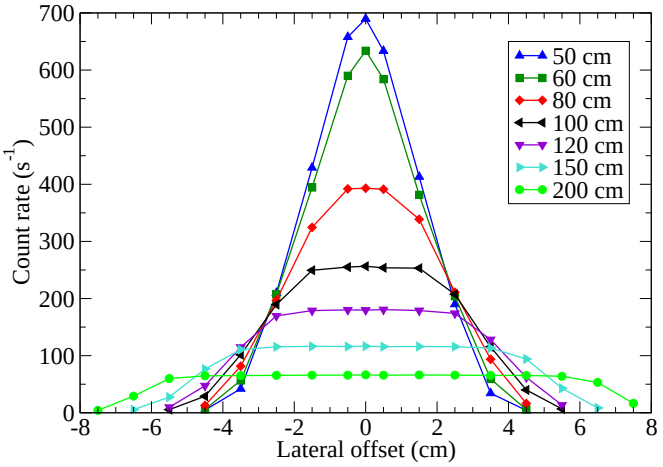


Figure 3.22: Lateral geometric sensitivity of the CDS for a number of distances from the HPGe detector.

### 3.4.4 Results

Figure 3.22 shows a plot of the lateral geometric sensitivity of the CDS at various distances from the HPGe. The point of maximal response was found to occur at 50 cm from the HPGe detector. For greater distances from the HPGe detector, the count rate decreases as does the geometric sensitivity. From this plot, the optimal source location can be selected based on the geometry of the source to be measured.

Figure 3.23 shows the geometric sensitivity of the CDS as a function of distance from the HPGe detector determined with both the $^{68}$Ge and $^{22}$Na spot markers. The data were normalized to the values at 100 cm. This distance was selected as the normalization point because the effects of true coincidence summing with $^{22}$Na and the less point-like nature due to a higher positron energy with $^{68}$Ge were negligible. There was good agreement between the $^{68}$Ge and $^{22}$Na data, except at the point closest to the HPGe detector (20 cm). At this point the $^{22}$Na data was 5.1 % less than the $^{68}$Ge data. As previously discussed, this was due to counting losses from true coincidence summing. A sum peak was visible

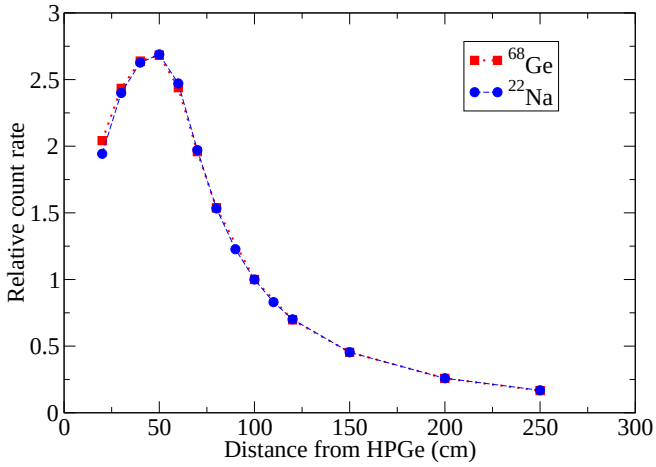


Figure 3.23: Geometric sensitivity of the CDS as a function of distance from the HPGe detector as measured with the $^{68}$Ge and $^{22}$Na spot markers.

at 1786 keV (511 keV + 1275 keV) in the ungated spectrum. However, there is no need for a careful geometric characterization in this region of the FOV of the CDS as the optimal measurement locations will be at distances greater than 50 cm from the HPGe, depending on the geometry of the source.

Figure 3.24 compares the vertical and lateral geometric sensitivities at 60 and 120 cm from the HPGe detector. There was good agreement between the lateral and vertical geometric sensitivities at both distances. This demonstrates the symmetry of the geometric sensitivity for offsets in either dimension. This allowed Figure 3.22 to be used to determine the optimal source location for a particular source geometry regardless of whether the source was elongated in the lateral or vertical dimension. This agreement also confirmed the geometric alignment of the components of the CDS (i.e., the alignment of the detectors and the source), as discussed in Section 3.2.4.

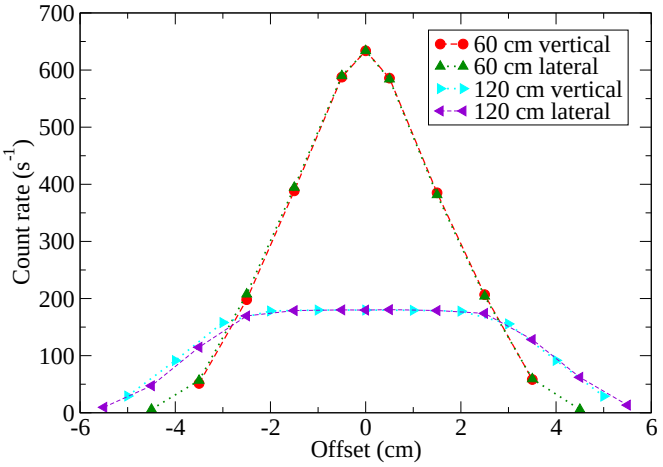


Figure 3.24: Comparison of the lateral and vertical geometric sensitivity of the CDS at 60 and 120 cm from the HPGe detector.

## 3.5 Conclusions

The goal of the work presented in this chapter was to develop and characterize a CDS that could be used to determine the activity of a $^{90}$Y source, specifically a sample of $^{90}$Y microspheres. The CDS was constructed with the necessary abilities of aligning the detectors and the source while limiting the bremsstrahlung that would be produced from a beta-emitting source and reach the detectors of the system. The source holder that was designed and constructed had the ability to be easily modified to accommodate any size source that was used in this work. The pulse-processing NIM electronics were tuned to allow the energy signal from the HPGe detector to be gated by the coincidence signal from the detector pair. The system allowed for concurrent measurement of the ungated signal to detect possible impurities, such as $^{88}$Y, that may be present in the measured samples. The advantages of using the CDS over a single HPGe detector were presented. These included a reduced peak area uncertainty for the same counting time due to a reduction in the bremsstrahlung

continuum in the gated spectrum and the elimination of the need to correct for 511 keV photons present in the EBG.

Accurate, quantifiable data are not able to be obtained with a counting system such as the CDS if counting losses due to dead time and pulse pile-up are not corrected for. A pulser method for correcting for counting losses was implemented and validated for the CDS. This method consisted of sending a known number of time-correlated pulser pulses into the respective detectors of the CDS and evaluating the number of the pulser pulses that were detected. The multiplicative correction is the ratio of the number of injected pulses with the number that were detected. Validation studies found that as long as counting losses were under 15 %, the method was able to correct to within 0.98 % of a base-line count rate. Above the 15 % loss rate, it was found that the pulser method over-corrects the count rate. Therefore, this 15 % cut-off will be used in all future measurements, and any measurement data with higher than 15 % losses will be rejected.

One disadvantage of the CDS compared to a single HPGe detector was the higher geometric sensitivity of the system. The geometric sensitivity of the CDS was characterized such that an optimal measurement location could be selected based on the geometry of the source-of-interest and the source used for the efficiency calibration. This ensured that measurements were independent of the source geometry. The geometric characterization of the CDS was completed with $^{22}$Na and $^{68}$Ge spot markers. The results provided plots to aid in selecting a measurement position that is independent of the source geometry.

The CDS was constructed and the necessary characterizations were completed. The measurement device should allow for the accurate activity assay of a $^{90}$Y source. The following chapter investigates the use of the CDS for this purpose.

# Chapter 4

# Spectroscopic assay of $^{90}$Y activity with the coincidence detection system

## 4.1 Introduction

Chapter 3 described the geometric sensitivity characterization and the counting losses correction that was implemented and validated for the coincidence detection system (CDS). This chapter extends the use of the CDS to spectroscopically assay the activity of $^{90}$Y sources. Efficiency calibrations of the CDS were completed with $^{22}$Na calibration sources to relate the coincidence-gated 511 keV peak count rate to a known activity. Corrections for differences between the attenuation properties of the sources used for efficiency calibrations and the $^{90}$Y sources were determined and applied to the measurement results. Additionally, corrections for radioactive decay were applied to ensure accurate activity assays.

The first $^{90}$Y activity assay completed with the CDS was on $^{90}$Y calibration source. This served to validate the ability of the CDS to accurately determine $^{90}$Y activity by

comparing the CDS-determined activity of the source to its known activity. The CDS was then used to determine the activity of a $^{90}$Y microsphere sample. The $^{90}$Y microspheres assayed were SIR-Spheres from Sirtex Medical. Sirtex Medical provides each sample of SIR-Spheres with an activity of 3 GBq $\pm$ 10 %. A spectroscopic assay of a SIR-Spheres sample that was completed by Selwyn et al. [2008] determined an activity 26 % higher than the 3 GBq activity provided by Sirtex Medical. In this work, the determined activity for the SIR-Spheres sample was also compared to the 3 GBq activity given by the manufacturer.

All spectra data were analyzed using the techniques described in Section 3.2.7. The statistical uncertainty associated with each individual measurement was accounted for when combining measurement results. The methods for combining the results of individual measurements are described in Section 4.6.

This work focused on the SIR-Spheres product. However, the methodologies established in this chapter could be extended to the TheraSphere product.

## 4.2 Validation of activity assay accuracy

The ability of the CDS to accurately determine the activity of a $^{22}$Na source with a $^{90}$Sr/$^{90}$Y source present was demonstrated as part of the work to validate the pulser counting losses correction in Section 3.3.4. These conditions mimicked the measurement conditions of a $^{90}$Y source. A validation study of the CDS's ability to determine the activity of a $^{90}$Y source was completed by comparing the CDS-determined activity of a $^{90}YCl_3$ standard activity solution to the known activity of the source.

### 4.2.1 $^{90}YCl_3$ standard activity solution

The National Institute of Standards and Technology (NIST) distributes a $^{90}$Y radioactivity standard solution annually through the Standard Reference Material (SRM) program. The standard solution (SRM no. 4427L) is intended for the calibration of instruments that are

Figure 4.1: Photograph of the $^{90}YCl_3$ radioactivity standard solution from the NIST SRM program in a flame-sealed ampoule.

used to determine radioactivity, such as dose calibrators. The source consists of $^{90}YCl_3$ in a solution of $1.0\,\text{mol}\cdot\text{L}^{-1}$ HCl. The 5 mL solution is contained within a borosilicate-glass flame-sealed ampoule (FSA). The solution has a typical uncertainty in massic activity (with units $\text{MBq}\cdot\text{g}^{-1}$) less than 1 % ($k = 2$), as determined with liquid-scintillation counting methods described in Section 2.4.1. The source measured in this work is shown in Figure 4.1. Based on the information given in the calibration certificate provided by NIST, this source had an activity of $15.20\,\text{MBq} \pm 0.31$ % ($k = 1$) on its reference date. The calibration certificate also stated that the $^{90}YCl_3$ solution had a 3.2 Bq $^{90}Sr$ impurity present on the reference date. The presence of $^{90}Sr$ as an impurity can affect the activity determination of $^{90}Y$ as $^{90}Y$ is the daughter of $^{90}Sr$. However, this relatively small amount of $^{90}Sr$ did not affect the spectroscopic determination of the $^{90}Y$ activity, as the $^{90}Sr$ activity was within the uncertainty of the $^{90}Y$ activity provided by NIST while the measurements were conducted.

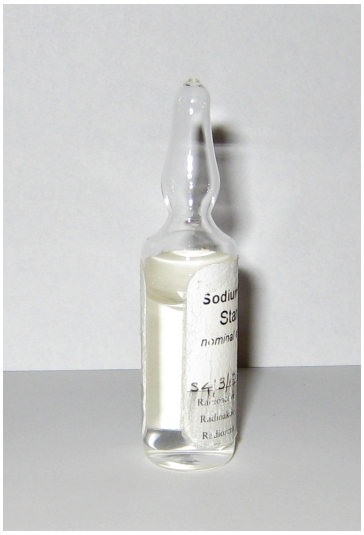

Figure 4.2: Photograph of the $^{22}$Na source in a flame-sealed ampoule. This source was used for the efficiency calibration of the CDS.

### 4.2.2 Efficiency calibration

The efficiency calibration of the CDS used for the determination of the $^{90}YCl_3$ solution's activity was completed with measurements of a $^{22}$Na calibration source in a FSA. The $^{22}$Na source had an activity of 254.7 kBq $\pm$ 0.41 % ($k = 1$) on its reference date. Figure 4.2 shows a photograph of the $^{22}$Na source.

The efficiency, $\varepsilon$, of the CDS was determined from measurements with the $^{22}$Na source using the equation,

$$\varepsilon = \frac{\dot{N}}{r \cdot A} \prod k_i, \tag{4.1}$$

where $\dot{N}$ is the net count rate of the 511 keV peak area, $r$ is the branching ratio of positron emissions of $^{22}$Na, $A$ is the activity of the $^{22}$Na source on its reference date, and $k_i$ is a series of corrections for counting losses and the radioactive decay of the source. These corrections are discussed in Sections 3.3 and 4.4, respectively.

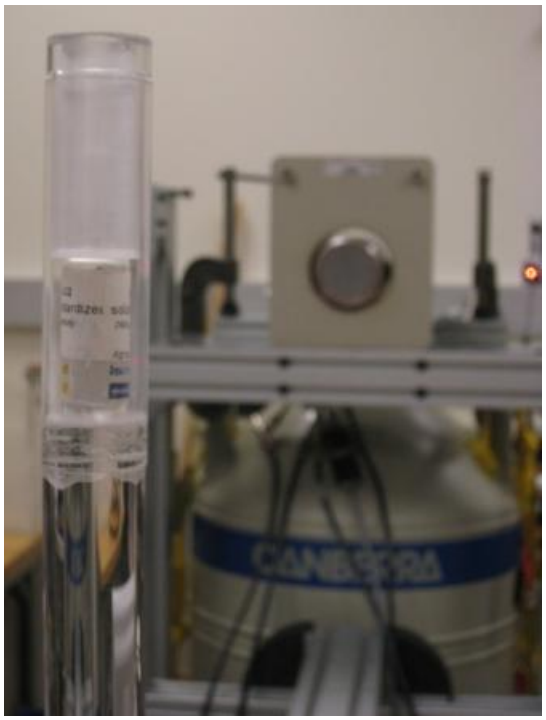

Figure 4.3: Photograph of the source holder constructed and used for measurements to determine the activity of the $^{90}$Y SRM source.

### 4.2.3 Source holder

The source holder used for measurements to determine the activity of the $^{90}YCl_3$ SRM source consisted of a 2.54 cm (1 in) diameter polymethyl methacrylate (PMMA) rod with a PMMA tube attached at the top. The tube had an outer diameter of 2.54 cm (1 in) and a nominal wall thickness of 0.16 cm ($\frac{1}{16}$ in). During measurements, the source vial was placed inside the tube and rested on top of the rod. To ensure reproducible positioning, a jig consisting of a PMMA rod with a centered, drilled hole was used to center the source vial inside of the source holder tube. Because the $^{22}$Na efficiency calibration source and the $^{90}YCl_3$ SRM source had very similar geometries (both contained in FSAs), the same positioning jig was used for both sources. A photograph of the source holder with the $^{22}$Na efficiency calibration source is shown in Figure 4.3. During the $^{90}YCl_3$ solution measurements (Section 4.2.4), water was placed in the source holder to provide additional shielding from the beta

particles emitted from $^{90}$Y. This was also completed during efficiency calibration measurements with the $^{22}$Na source so that the attenuation differences of the 511 keV annihilation photons would be minimized between the measurement setups.

### 4.2.4 Measurements

The $^{22}$Na source used for the efficiency calibration and the $^{90}YCl_3$ SRM source both had an active solution height of approximately 3 cm. Based on the geometric characterization of the CDS described in Section 3.4, a measurement location at 120 cm from the HPGe detector was selected. This location was independent of the geometry of the sources. All measurements were completed with the source at 120 cm from the HPGe detector with the center of the source solution aligned with the central axis of the detectors.

During the initial measurements of the $^{90}YCl_3$ SRM source, the pulser series used for calculating counting loss corrections began behaving anomalously. This resulted in the 511 keV peak-of-interest widening from a typical full-width at half-maximum (FWHM) of 2.5 keV to more than 12.5 keV and the pulser peak changing position randomly within the collected pulse-height spectrum. Due to this behavior, the pulser series was disconnected from the electronics series. This resolved the issue with the peak width. Measurements were continued without the pulsers and all measurements used in the determination of the activity of the $^{90}YCl_3$ SRM source were completed without the pulser series.

The $^{90}YCl_3$ SRM source had a lower starting activity of 15.20 MBq compared to the $\sim$ 400 MBq $^{90}$Sr/$^{90}$Y source investigated in Section 3.3. The counting losses experienced by the CDS with the $^{90}$Sr/$^{90}$Y source at 120 cm were 5.7 %. These results are given in Section 3.3.4. With the much lower count rates that were present with the $^{90}YCl_3$ SRM source, the counting losses were expected to be smaller and perhaps negligible. To evaluate the potential losses experienced by the CDS with the $^{90}YCl_3$ SRM source, a comparison of the determined activity both with and without the live time clock was completed.

For the efficiency calibration of the CDS, the coincidence-gated spectrum of the $^{22}$Na calibration source was collected for 6000 s a total of 16 times at various time points during the measurement of the $^{90}YCl_3$ SRM source. Coincidence-gated spectra of the $^{90}YCl_3$ SRM source were collected 15 times with a total counting time of 220 h. Concurrent ungated spectra were also collected to check for any potential impurities, such as $^{88}$Y.

The activity, $A$, of the $^{90}YCl_3$ SRM source was determined from measurement results using Equation 2.9, which is given again here:

$$A = \frac{\dot{N}}{r \cdot \varepsilon} \prod k_i. \tag{4.2}$$

In this equation, $\dot{N}$ is the net count rate of the 511 keV peak area, $r$ is the branching ratio of the IPP, $\varepsilon$ is the efficiency of the the detector (given in Equation 4.1), and $k_i$ is a series of corrections for counting losses, the radioactive decay of the source, and attenuation differences between the efficiency calibration source and the source-of-interest. These corrections are discussed in Sections 3.3, 4.4, and 4.5, respectively.

## 4.3 Activity assay of SIR-Spheres

SIR-Spheres are supplied in a glass shipping vial with a total volume of 5 mL of microspheres and water. Spectroscopic measurements were performed to determine the activity of the SIR-Spheres in both the glass shipping vial and the plastic v-vial. This was done to provide an activity for each vial configuration for the well-type ionization chamber measurements that are discussed in Chapter 5.

### 4.3.1 Efficiency calibration

The efficiency calibration of the CDS for determining the activity of the SIR-Spheres samples was completed with two $^{22}$Na calibration sources. The first source was the same $^{22}$Na

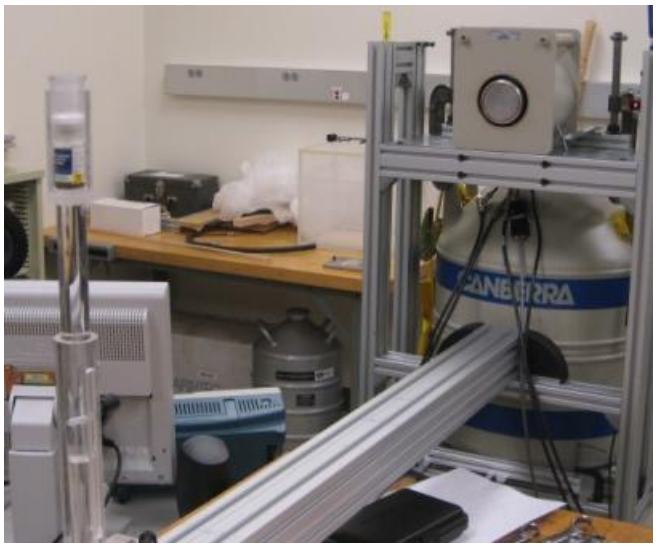

Figure 4.4: Photograph of the experimental setup and source holder used for measurements of the SIR-Spheres sources with the CDS.

source contained in a FSA that was used for the efficiency calibration for the $^{90}YCl_3$ SRM source activity determination. The second $^{22}Na$ source consisted of a $^{22}Na$ solution that was placed in a SIR-Spheres shipping vial. The $^{22}Na$ solution (Eckert and Ziegler, Valencia, CA) consisted of NaCl in water and had a massic activity uncertainty of 1.0 %. The solution was transferred to the shipping vial with a syringe and a stainless steel needle. The mass of the solution in the shipping vial was gravimetrically determined with a Sartorius (Goettingen, Germany) balance that had 0.1 mg resolution. Using the massic activity and mass of the solution, the $^{22}Na$ activity contained within the shipping vial was determined to be 1.68 MBq $\pm$ 1.0 % ($k = 1$) on the reference date. Water was added to the solution to increase the contained liquid volume to 5 mL to match the volume in a SIR-Spheres sample. Equation 4.1 was used to determine the efficiency of the CDS from measurements of the $^{22}Na$ sources.

### 4.3.2 Source holder

The glass shipping vial that the SIR-Spheres were provided in was too large to fit in the existing source holder that was used for measurements of the $^{90}YCl_3$ solution. Another

holder was constructed to accommodate the shipping vial and v-vial. Again the holder consisted of a 2.54 cm (1 in) diameter PMMA rod with a PMMA tube attached at the top, but the tube had an outer diameter of 3.81 cm (1.5 in) and a nominal wall thickness of 0.32 cm ($\frac{1}{8}$ in). During measurements, the source vial was place inside the tube and rested on top of the rod. A positioning jig consisting of a PMMA rod with a centered, drilled hole was used to center the source inside of the tube, ensuring reproducible positioning of the source vial. Because of the difference in the geometry of the FSA and the SIR-Spheres vials, separate positioning jigs were created for each source container. Because of the greater wall thickness of both the constructed holder and the vials containing the microspheres, the source holder was not filled with water. This also limited the magnitude of the attenuation correction (discussed in Section 4.5) that accounts for the difference in the attenuation of the 511 keV annihilation photons between the efficiency calibration and SIR-Spheres measurement geometries. Figure 4.4 shows a photograph of the experimental measurement setup of the CDS with the shipping vial in the constructed holder.

### 4.3.3 Measurements

Like the measurements with the $^{90}YCl_3$ SRM solution, all measurements used in the determination of the SIR-Spheres activity were performed at 120 cm from the face of the HPGe detector with the center of the active source material height aligned with the central axis of the detectors. The pulser method for correcting for counting losses described in Section 3.3 was used for all measurements.

For the efficiency calibration of the CDS, the coincidence-gated spectra of the $^{22}Na$ calibration sources were collected. The $^{22}Na$ source in the FSA was measured for 6000 s a total of ten times at various time points during the measurement of the $^{90}Y$ microsphere sources, and the $^{22}Na$ source in the shipping vial was measured for 6000 s a total of six

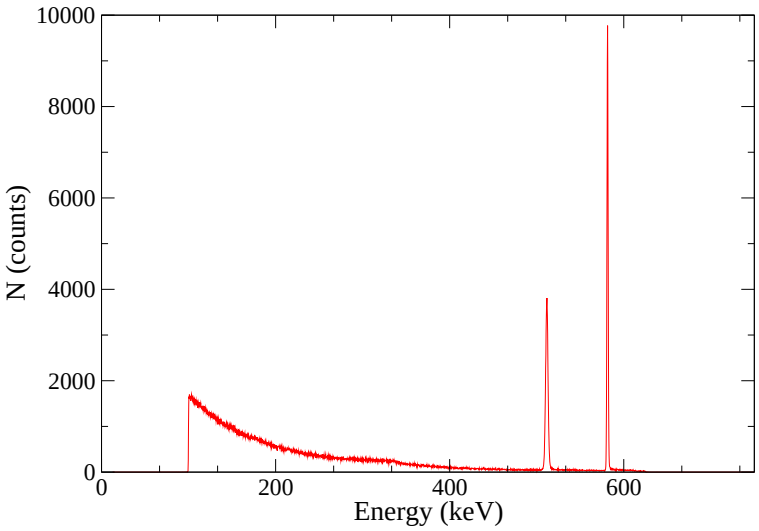


Figure 4.5: Plot of a typical coincidence-gated $^{90}$Y spectrum measured in this work. The pulser peak is shown at approximately 580 keV.

times. The efficiency of the CDS for both sources was calculated from these measurements using Equation 4.1.

Coincidence-gated spectra were collected for the SIR-Spheres in the shipping vial 17 times for a total counting time of 68 h. The microspheres were then transferred from the shipping vial to a v-vial. Coincidence-gated spectra were collected for the SIR-Spheres in the v-vial 20 times for a total counting time of 186 h. The activity of the $^{90}$Y microspheres in each vial was calculated from measurements using Equation 4.2. From the results described in Section 3.3.4, only measurements with less than 15 % counting losses were included in these calculations. An example of a typical coincidence-gated $^{90}$Y spectrum is shown in Figure 4.5. This spectrum features the reduced bremsstrahlung continuum and 511 keV peak seen previously in Figure 3.9, in addition to the pulser peak that is present at approximately 580 keV. This example was from a measurement of the SIR-Spheres in the shipping vial.

Ungated spectra were collected concurrently with the gated measurements for the detection of contaminants that may have been present in the $^{90}$Y microspheres, such as $^{88}$Y. As mentioned in Section 3.2.1, $^{88}$Y is a positron-emitter and has a 106.6 d half-life. Its presence as a contaminant could affect the determination of the activity of the $^{90}$Y microspheres with the CDS by contributing to the counts in the 511 keV peak in the coincidence-gated spectrum. $^{88}$Y also has gamma emissions at 898 keV and 1836 keV that would be present in the ungated spectra. These emissions could be used to assay the activity of $^{88}$Y present as an impurity such that corrections could be applied to the determined $^{90}$Y activity. Gated and ungated spectra measurements of the $^{90}$Y microspheres were repeated more than 1 month after the reference date (i.e., after more than 10 half-lives). At this point, the $^{90}$Y microspheres were effectively no longer active as a survey meter could not distinguish the source from background. Again, the ungated results were checked for $^{88}$Y to ensure the bremsstrahlung continuum present in the $^{90}$Y photon spectra had not resulted in the inability to resolve the $^{88}$Y gamma emissions. The gated spectra were checked for the presence of the 511 keV peak, which could indicate the presence of a $^{90}$Sr impurity.

## 4.4 Radioactive decay corrections

This section describes the corrections that were used to account for the radioactive decay of the sources used to determine the activity of $^{90}$Y sources. This includes both the $^{90}$Y sources and the $^{22}$Na sources used for the efficiency calibration of the CDS. The equation,

$$k_{\text{Ref time}} = e^{\lambda T}, \tag{4.3}$$

defines the multiplicative correction, $k_{\text{Ref time}}$, used to correct measurements to a reference time. $T$ is the time difference between the reference time and the measurement start time. The decay constant, $\lambda$, is defined by the equation,

$$\lambda = \frac{\ln(2)}{t_{1/2}}, \tag{4.4}$$

where $t_{1/2}$ is the half-life of the source being measured.

The multiplicative correction, $k_{\text{Measurement decay}}$, was used to correct for decay that occurred during the measurement, and is defined by the equation,

$$k_{\text{Measurement decay}} = \frac{\lambda t}{1 - e^{-\lambda t}}, \tag{4.5}$$

where $\lambda$ is the decay constant and $t$ is the measurement time.

## 4.5 Attenuation correction

To accurately determine activity from spectra data, a correction for the difference in the attenuation properties of the efficiency calibration source and the $^{90}$Y source-of-interest was applied to the measurement results [Debertin and Helmer, 1988]. Like positron emission tomography (PET), the probability of recording an event with the CDS was dependent on the detection of the correlated annihilation photons in both detectors [Phelps, 2004]. Thus, the correction factor corrects for losses from attenuation experienced by either detector.

For this work, the Monte Carlo transport code MCNP5 [X-5 Monte Carlo Team, 2005] was used to calculate the attenuation correction for the different efficiency calibration source and source-of-interest combinations used for determining the activity of the source-of-interest from measurements with the CDS. Table 4.1 provides a list of these source combinations.

The material information for the $^{22}$Na sources in the FSA and the shipping vial and the $^{90}YCl_3$ SRM source was obtained from the respective source's calibration certificate. Geometric information, such as the outer diameter of the vial and the fluid height of the sources in the FSAs was determined with caliper measurements. The NIST FSA geometry

Table 4.1: Table of the efficiency calibration source and source-of-interest combinations for which attenuation corrections were determined.

| Combination | Efficiency calibration source | Source-of-interest |
|---|---|---|
| 1 | $^{22}$Na in flame sealed ampoule | $^{90}YCl_3$ in flame sealed ampoule |
| 2 | $^{22}$Na in flame sealed ampoule | $^{90}$Y microspheres in shipping vial |
| 3 | $^{22}$Na in flame sealed ampoule | $^{90}$Y microspheres in v-vial |
| 4 | $^{22}$Na in shipping vial | $^{90}$Y microspheres in shipping vial |

had a 0.6-mm-thick borosilicate glass wall. The $^{90}YCl_3$ SRM source was in a solution of 1.0 mol·L$^{-1}$ HCl. The $^{22}$Na source in the FSA was in a solution of 0.1 mol·L$^{-1}$ HCl. The $^{22}$Na source in the shipping vial was in a solution of water. The water added to the solution in the shipping vial to increase the total volume to 5 mL was taken into account.

The geometric information of the shipping vial and v-vial was also obtained with caliper measurements. The outer diameters of the vials and the settled microsphere heights were measured. Then one of each of the vials was sacrificed to determine the vial wall thicknesses. The dimensions of the "v" in the v-vial were also determined from the sacrificed vial. Sirtex Medical stated that the shipping vial was made from borosilicate glass and the v-vial was made of polycarbonate [Sirtex Medical, 2011]. Sirtex Medical also stated that the nominal wall thickness of the v-vial was 2 mm. This agreed with the average caliper measurement of 1.98 mm.

Material definitions of polycarbonate and borosilicate glass were obtained from the NIST website [Berger et al., 2005]. The material definitions of the solutions were calculated from the information given in the calibration certificates. Polystyrene from the NIST website was used as an approximation for the material of the resin microspheres [Berger et al., 2005]. The microspheres were settled at the bottom of the vials during measurements. The physical density of the microspheres was 1.6 g·cm$^{-3}$ [Dezarn et al., 2011], but the effective density of the settled microspheres was lower due to the water between the settled microspheres. The packing density (i.e., the fraction of the volume occupied by microspheres) of the settled microspheres was estimated in order to calculate an effective density of the

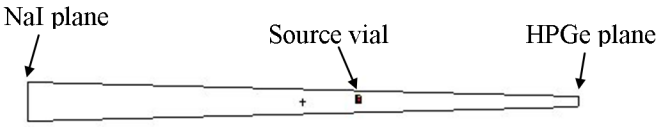


Figure 4.6: Rendering of the simulation geometry used to calculate the attenuation corrections. The lines connecting the detector planes define the FOV of the detection system.

material. Studies have found that spheres randomly settling in a container have packing densities that range from 0.56 to 0.64 [Haughey and Beveridge, 1969, Scott and Kilgour, 1969, Onoda and Liniger, 1990, Jaeger and Nagel, 1992]. A packing density of 0.60 was assumed for the microspheres settled at the bottom of the vials. An effective density of the settled microspheres was calculated using this packing density to weight the average density of the microspheres and water. This effective density was calculated to be $1.36\,\mathrm{g{\cdot}cm^{-3}}$. Simulations were also completed with effective densities that were calculated using the upper and lower bounds of the packing densities. The variation in the results due to the potential variation in the packing density was accounted for in the uncertainty associated with the attenuation correction.

The simulation geometry used in the MCNP5 simulations is shown in Figure 4.6. Circular planes were modeled to represent the front faces of the NaI and HPGe detectors. The diameters of the planes were modeled to match those of the respective detectors. The source vials were modeled using the geometry and material definitions described above. The active material in each source model was centered at 120 cm from the HPGe plane. Monoenergetic 511 keV photons were uniformly started in the active source material, and F2 tallies were used to score the uncollided fluence at each of the detector planes. This was completed

Table 4.2: MCNP5-calculated attenuation corrections applied for each efficiency calibration source and $^{90}$Y source-of-interest combination investigated.

| Vial combination | | |
|---|---|---|
| Efficiency calibration source | Source-of-interest | Attenuation correction |
| $^{22}$Na in flame sealed ampoule | $^{90}YCl_3$ in flame sealed ampoule | 1.001 |
| $^{22}$Na in flame sealed ampoule | $^{90}$Y microspheres in shipping vial | 1.178 |
| $^{22}$Na in flame sealed ampoule | $^{90}$Y microspheres in v-vial | 1.026 |
| $^{22}$Na in shipping vial | $^{90}$Y microspheres in shipping vial | 1.055 |

for each source vial. All simulations were run with sufficient particles to achieve statistical uncertainties of less than 0.1 %. Attenuation corrections, $k_{\text{Attenuation}}$, were calculated as the product of the ratio of the efficiency calibration vial simulation results, $F2_{\text{Cal., HPGe}}$ and $F2_{\text{Cal., NaI}}$, over the source-of-interest simulation results, $F2_{\text{Source., HPGe}}$ and $F2_{\text{Source., NaI}}$, from each detector, as given by Equation 4.6. Corrections were calculated for each vial combination that was investigated. The calculated attenuation corrections are presented in Table 4.2.

$$k_{\text{Attenuation}} = \frac{F2_{\text{Cal., HPGe}}}{F2_{\text{Source., HPGe}}} \cdot \frac{F2_{\text{Cal., NaI}}}{F2_{\text{Source, NaI}}} \tag{4.6}$$

## 4.6 Combining measurement results

The statistical uncertainty associated with each count rate measurement used to determine activity was not the same. To account for this, the weighted average of the determined activity, $\bar{A}$, was calculated using the equation,

$$\bar{A} = \frac{\sum A_i w_i}{\sum w_i}, \tag{4.7}$$

where $A_i$ is the determined activity from count rate measurement $i$, and $w_i$ is the weighting factor. The weighting factor is defined by the equation,

$$w_i = \frac{1}{s_i^2}, \tag{4.8}$$

where $s_i$ is the measured standard deviation of measurement $i$. The standard deviations of the individual measurements were calculated using the methods described in Section 3.2.7. This same weighting method was used to calculate the weighted average of the efficiency of the CDS.

To combine the measured standard deviations associated with each measurement, the pooled or internal variance, $var(A)_{\text{Internal}}$, was calculated using the equation,

$$var(A)_{\text{Internal}} = \frac{1}{\sum w_i}. \tag{4.9}$$

The internal variance assumes that the distribution about the mean is satisfactory as it does not depend on how well the individual activity values agree. The weighted or external variance, $var(A)_{\text{External}}$, does account for the potential spread in the individual activity values, which may be outside their associated standard deviation. The external variance was calculated using the equation,

$$var(A)_{\text{External}} = \frac{\sum (A_i - \bar{A})^2 w_i}{\sum w_i (m-1)}, \tag{4.10}$$

where $m$ is the total number of measurements that were performed. Both the internal and external variances were calculated for each data set and the greater of the two was used as the variance of the combined measurement results.

## 4.7 Results

### 4.7.1 Validation assay

The pulser series for determining the counting losses correction was not used in measurements to determine the activity of the $^{90}YCl_3$ SRM source. To assess the need to account for counting losses, the activity of the $^{90}YCl_3$ SRM source was determined from measurements using both the live time clock and the typical real time. The activity of the $^{90}YCl_3$ SRM source was determined to be 15.6 MBq $\pm$ 2.25 % using both methods. This indicated that the counting losses due to dead time for measurements of the $^{90}Y$ SRM source were negligible. As mentioned in Section 3.3, the live time clock does not account for pulse pile-up losses. At these lower relative count rates, it was assumed that the losses due to pulse pile-up were also negligible within 0.2 %. The determined activity was +2.6 % from the activity of 15.20 MBq that was provided by NIST. This difference was within the combined expanded uncertainty associated with the activity determined with the CDS. This indicated that the CDS was able to accurately determine the activity of $^{90}Y$ sources. Table 4.3 provides the uncertainty budget for the activity determination of the $^{90}YCl_3$ SRM source with the CDS. No impurities, such as $^{88}Y$, were detected in the ungated spectra, so no corrections were applied to the determined activity.

### 4.7.2 SIR-Spheres assay

Using the $^{22}Na$ source in the FSA as the efficiency calibration source resulted in the SIR-Spheres activity determination with the lowest uncertainty. The activity of the SIR-Spheres in the shipping vial was determined to be 3.72 GBq $\pm$ 1.84 % using the $^{22}Na$ source in the FSA as the efficiency calibration source. This activity was 24 % higher than the 3 GBq stated activity of the manufacturer. This was outside the manufacturer's stated uncertainty of $\pm$10 %. Selwyn et al. [2008] also performed a spectroscopic activity assay of a SIR-Spheres sample in the shipping vial using a single HPGe detector and determined an activity

Table 4.3: Uncertainty budget for the activity determination of the $^{90}YCl_3$ solution from the NIST SRM program.

| | Uncertainty | |
|---|---|---|
| Parameter | Type A (%) | Type B (%) |
| $^{22}$Na net count rate | 0.11 | – |
| $^{22}$Na activity | – | 0.41 |
| $^{22}$Na half-life | – | 0.04 |
| $^{22}$Na branching ratio | – | 0.02 |
| | | |
| $^{90}$Y net count rate | 1.59 | – |
| $^{90}$Y half-life | – | 0.03 |
| $^{90}$Y branching ratio | – | 1.47 |
| Counting losses | – | 0.20 |
| | | |
| Attenuation correction | 0.11 | 0.20 |
| Geometric positioning | – | 0.26 |
| Peak analysis algorithm | – | 0.15 |
| | | |
| Quadratic sum | 1.60 | 1.58 |
| Combined uncertainty | 2.25 | |
| Expanded combined uncertainty ($k = 2$) | 4.50 | |

that was 26 % higher than the 3 GBq value given by the Sirtex. These results suggest the manufacturer is not using an accurate method for determining the activity of the SIR-Spheres. Table 4.4 provides the uncertainty budget for the activity determination of the SIR-Spheres in the shipping vial with the $^{22}$Na source in the FSA as the calibration source.

Using the $^{22}$Na source in the shipping vial for the efficiency calibration, the activity of the SIR-Spheres in the shipping vial was determined to be 3.65 GBq $\pm$ 2.1 %. This value agreed with the activity determined with the $^{22}$Na source in the FSA as the efficiency calibration within its associated uncertainty. Since the activity determined with $^{22}$Na source in the FSA as the efficiency calibration had a lower uncertainty, this value was used in subsequent evaluations (such as determining calibration coefficients from well-type ionization chamber measurements, as presented in Chapter 5).

Table 4.4: Uncertainty budget for the activity determination of SIR-Spheres in the shipping vial with the $^{22}$Na FSA source as the efficiency calibration.

| | Uncertainty | |
|---|---|---|
| Parameter | Type A (%) | Type B (%) |
| $^{22}$Na net count rate | 0.19 | – |
| $^{22}$Na activity | – | 0.41 |
| $^{22}$Na half-life | – | 0.04 |
| $^{22}$Na branching ratio | – | 0.02 |
| | | |
| $^{90}$Y net count rate | 0.22 | – |
| $^{90}$Y half-life | – | 0.03 |
| $^{90}$Y branching ratio | – | 1.47 |
| Counting-losses correction | – | 0.84 |
| | | |
| Attenuation correction | 0.11 | 0.38 |
| Geometric positioning | – | 0.26 |
| Peak analysis algorithm | – | 0.15 |
| | | |
| Quadratic sum | 0.31 | 1.81 |
| Combined uncertainty | 1.84 | |
| Expanded combined uncertainty ($k = 2$) | 3.68 | |

Table 4.5: Uncertainty budget for the activity determination of SIR-Spheres in the v-vial with the $^{22}$Na FSA source as the efficiency calibration.

| | Uncertainty | |
|---|---|---|
| Parameter | Type A (%) | Type B (%) |
| $^{22}$Na net count rate | 0.19 | – |
| $^{22}$Na activity | – | 0.41 |
| $^{22}$Na half-life | – | 0.04 |
| $^{22}$Na branching ratio | – | 0.02 |
| | | |
| $^{90}$Y net count rate | 0.79 | – |
| $^{90}$Y half-life | – | 0.03 |
| $^{90}$Y branching ratio | – | 1.47 |
| Counting-losses correction | – | 0.84 |
| | | |
| Attenuation correction | 0.11 | 0.21 |
| Geometric positioning | – | 0.26 |
| Peak area algorithm | – | 0.15 |
| | | |
| Quadratic sum | 0.82 | 1.78 |
| Combined uncertainty | 1.96 | |
| Expanded combined uncertainty ($k = 2$) | 3.92 | |

The activity of the SIR-Spheres in the v-vial was determined to be 3.46 GBq $\pm$ 1.96 %. The lower activity in the v-vial compared to that in the shipping vial was expected as not all of the microspheres were able to be transferred from the shipping vial to the v-vial. Table 4.5 provides the uncertainty budget for the activity determination of the SIR-Spheres in the v-vial with the $^{22}$Na source in the FSA as the efficiency calibration source.

Selwyn et al. [2008] detected trace amounts of $^{88}$Y as an impurity in their measured $^{90}$Y microsphere sample. They corrected their results to account for the effects of the $^{88}$Y on their measurements. Ungated spectra were collected concurrently with all coincidence-gated spectra taken in this work. Additionally, ungated measurements were completed after the $^{90}$Y had effectively decayed away. An analysis of all ungated spectra taken of the SIR-Spheres samples showed no detectable amount of $^{88}$Y, so no corrections were applied in this work. Gated spectra collected after the $^{90}$Y microspheres effectively were no longer active had no 511 keV peak present. This indicated that there was no detectable $^{90}$Y still present due to a $^{90}$Sr impurity.

## 4.8 Conclusions

The ability of the CDS to accurately determine the activity of $^{90}$Y was demonstrated by comparing the CDS-determined activity of a $^{90}$Y SRM source to its known activity. This accurate determination of $^{90}$Y activity required an accurate efficiency calibration, attenuation corrections, and corrections for radioactive decay. Additionally, corrections for pair production interactions in the source or source holder from the bremsstahlung produced by the $^{90}$Y beta particles could be applied, but this effect was found to be negligible by Selwyn et al. [2007a]. The CDS was used to determine the activities of samples of SIR-Spheres in both a shipping vial and a v-vial with uncertainties ($k = 1$) of 1.84 % and 1.96 %, respectively. These determined activities can now be used to calibrate well-type ionization

chambers for clinical measurements of $^{90}$Y microspheres. These results demonstrated the potential use of the CDS as a standard measurement device for $^{90}$Y microsphere activity.

# Chapter 5

# Characterization of well-type ionization chambers for measurement of $^{90}$Y microsphere samples

## 5.1 Introduction

Determining the activity of a $^{90}$Y microsphere sample with a coincidence detection system (CDS) is not practical in a clinical setting. The ability to determine the activity of a $^{90}$Y microsphere sample from measurements needs to be transferred to a clinically-relevant measurement device, such as a well-type ionization chamber, through calibration of the device. As described in Section 2.6, the calibration of well-type ionization chambers differs between nuclear medicine and radiation oncology departments. This work has characterized both a Capintec (Ramsey, New Jersey) 12 atm dose calibrator and a Standard Imaging (SI) (Middleton, Wisconsin) IVB 1000 well chamber for the potential clinical determination of $^{90}$Y

microsphere activity. The current clinical measurements of $^{90}$Y microspheres are typically performed with dose calibrators in nuclear medicine departments. However, the calibration protocol used with well chambers allows these devices to be calibrated by an accredited dosimetry calibration laboratory (ADCL) in the exact measurement geometries that will be used clinically. These calibration methods would have the advantage of being able to provide a more accurate $^{90}$Y microsphere activity determination from clinical measurements compared with the calibration methods typically used in nuclear medicine.

A $^{90}$Y microspheres sample is fundamentally different from a uniformly distributed liquid source as the distribution of the microspheres is dependent on their state of agitation. These potential variations in the locations and effective densities of a $^{90}$Y microspheres sample may cause variations in the response of a well-type ionization chamber [Dezarn and Kennedy, 2007]. These effects were analyzed for both of the investigated well-type ionization chambers.

As mentioned in Section 2.2, there are two microsphere products. The work presented in this chapter focuses on the SIR-Spheres product as activity determinations of a SIR-Spheres sample had been completed with CDS measurements. The activity preparation methods used with the SIR-Spheres product are susceptible to being affected by the volume dependence of the well-type ionization chamber used for determining the source's activity. This work investigates the volume dependence of both well-type ionization chambers and their potential effects on the $^{90}$Y microsphere activity delivered to the patient. Additionally, the effects of source holders, vial wall thickness, and microsphere material are investigated. These characterizations were completed using both measurements and Monte Carlo simulations. Based on the results of these characterizations, suggestions for improvements to the current measurement methods for SIR-Spheres are presented.

### 5.1.1 Present clinical preparation of SIR-Spheres activity

The methods used to determine the prescription activity for the SIR-Spheres treatment are described in Section 2.2. Once the prescription activity has been determined, this activity is prepared for delivery to the patient. SIR-Spheres are provided by Sirtex Medical at the 3 GBq level on a reference date in a shipping vial with a total volume of 5 mL of microspheres and water. Typical prescription activities are in the range of $1.0 - 2.5$ GBq [Dezarn et al., 2011]. The recommended preparation of the activity includes: (1) agitating the microspheres in the shipping vial and completing an initial measurement in a dose calibrator, (2) re-agitating the microspheres and drawing out the desired activity with a syringe based on the proportion of the 5 mL volume, (3) re-measurement of the shipping vial, and (4) taking the difference of the measurements to determine the activity in the syringe. Once the desired activity is in the syringe, the microspheres are transferred to a v-vial. The v-vial is then placed in the delivery apparatus for delivery to the patient. It is important to note that no volume correction is applied to the second measurement result, and both measurements are completed with the same dose calibrator dial setting. If the response of the dose calibrator used for the preparation of the SIR-Spheres activity is dependent on the volume of the source, the actual activity that is delivered to the patient may differ from the prescribed activity. Additionally, because no National Institute of Standards and Technology (NIST)-traceable standard is available, the dial setting of the dose calibrator is based on the manufacturer-stated activity.

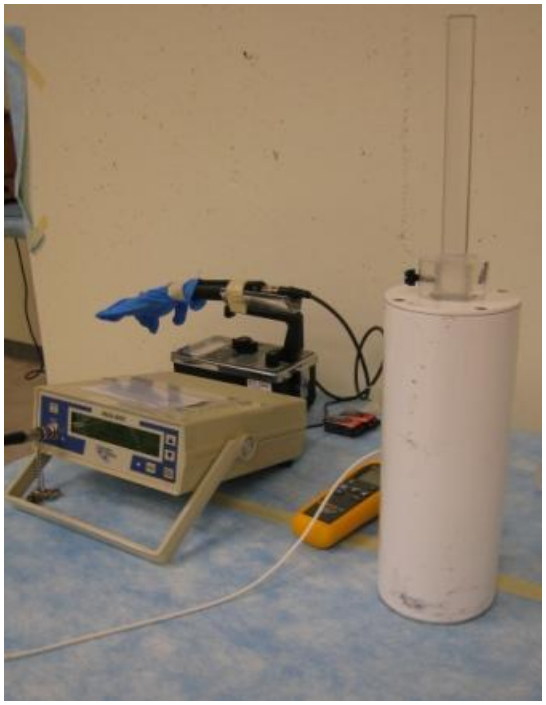

Figure 5.1: Photograph of the Standard Imaging IVB 1000 well chamber connected to a Standard Imaging Max 4000 electrometer.

## 5.2 Measurements of $^{90}$Y sources in well-type chambers

### 5.2.1 Experimental setup

#### 5.2.1.1 Chambers

Measurements were completed with both a well chamber and a dose calibrator. The well chamber investigated in this work was a SI IVB 1000 well chamber (serial number: H010484). Figure 5.1 shows the IVB 1000 well chamber connected to a SI Max 4000 electrometer. The IVB 1000 chamber was originally designed for measurements of intravascular brachytherapy source trains. The chamber was selected due to its large axial region of uniform response which allowed for the measurement of sources with elongated geometries [DeWerd et al., 2006]. The source vials for the $^{90}$Y microspheres can have source fluid heights of nearly 5 cm, so the large axial region of uniform response was necessary. The chamber body has a height of 26 cm and a diameter of 10.1 cm. The well of the chamber has a diameter of 3.7 cm and a depth of 22.2 cm. The IVB 1000 chamber is an air-communicating chamber. All measurements were corrected to standard temperature and pressure using Equation 2.11. A Max 4000 electrometer was used to apply a +300 V potential across the collecting electrode and the chamber inner wall during measurements. The electrometer was also used to determine the ionization current for each measurement. The electrometer-specific correction from the electrometer's calibration report was applied to all measurement results.

The dose calibrator investigated in this work was a Capintec 12 atm dose calibrator (serial number: 030801). Figure 5.2 shows the 12 atm dose calibrator connected to a SI Max 4000 electrometer. This chamber was filled with pressurized argon and was representative of a typical dose calibrator used in nuclear medicine departments in the U.S. The chamber body has a height of 43 cm and a diameter of 16.8 cm. The well of the chamber has a diameter of 7.0 cm and a depth of 27.2 cm. All measurements were completed with

Figure 5.2: Photograph of the Capintec 12 atm dose calibrator connected to a Standard Imaging Max 4000 electrometer.

a polycarbonate well liner in place. A Max 4000 electrometer was used to apply a +300 V potential across the collecting electrode and the chamber inner wall during measurements. This electrometer was also used to determine the ionization current for each measurement. The electrometer-specific correction from the electrometer's calibration report was also applied to all measurement results.

#### 5.2.1.2 Source holders and vials

As described in Section 5.1.1, the preparation of SIR-Spheres involves transferring the microspheres from the glass shipping vial to the polycarbonate v-vial. Both vials were investigated in this work. No existing source holder for IVB 1000 well chamber could accommodate these vials. A source vial holder was constructed from polymethyl methacrylate (PMMA) to hold each of these vials during measurements with the IVB 1000 well chamber and the 12 atm dose calibrator. The source holder consisted of collars that were attached to the neck of the vials with nylon screws. A photograph of the vials with the attached collars is


Figure 5.3: Photograph of the source holder collars attached to the v-vial (left) and the shipping vial (right).

shown in Figure 5.3. The collars were then fixed to a PMMA rod with a nylon set screw. Likewise, the rod/vial assembly was attached to a PMMA pedestal with a nylon set screw. The pedestal sat at the top of the well of the chamber, holding the source vial in place during measurements. The depth of the vial within the well could be adjusted by translating the rod up or down through the pedestal. Photographs of the constructed holder with both vials are shown in Figure 5.4 (a) and (b).

Dose calibrator measurements typically utilize a PMMA "dipper" source holder (see Figure 5.5). The dipper holder provides two measurement geometries. Vial measurements are typically completed with the vial in the bottom cup of the dipper, and syringe measurements are typically completed with syringe placed through the ring that is positioned higher on the the holder's post. The present clinical measurements of SIR-Spheres are completed in a dose calibrator with the shipping vial placed in the cup of the dipper holder. This measurement geometry was investigated in addition to the source vials in the constructed holder.

(a) 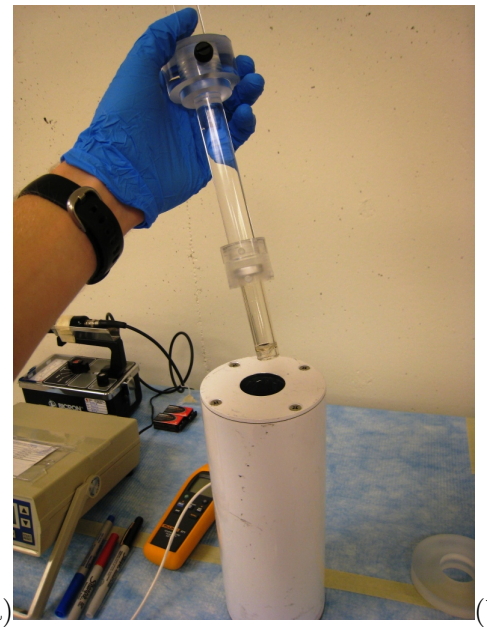 (b) 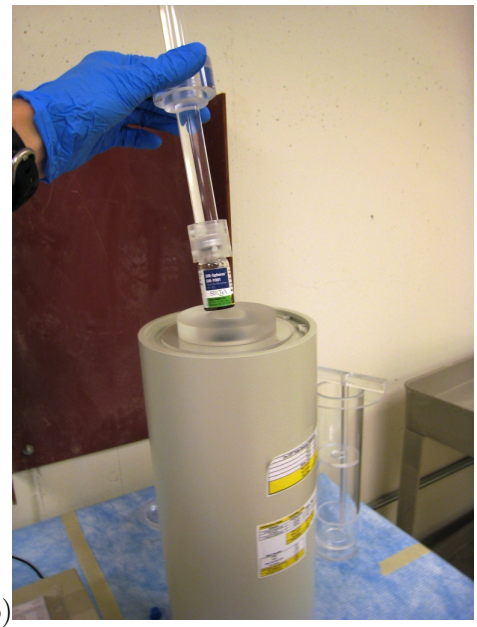

Figure 5.4: Photograph of the constructed source holder with (a) the v-vial and the IVB 1000 well chamber and (b) the shipping vial and the 12 atm dose calibrator.

### 5.2.2 $^{90}YCl_3$ standard activity solution measurements

Prior to measurements of the $^{90}YCl_3$ standard reference material (SRM) solution, a Novoste (Springfield, Virginia) Beta-Cath$^{TM}$ 30 mm source train was scanned through the wells of both chambers. The point of maximum response for each chamber was determined. The constructed source holder was configured to position the center of 5 mL of liquid contained within the shipping vial or v-vial at the point of maximum response. A visual indicator line was inscribed on the PMMA rod of the constructed holder for each chamber to reproducibly position the source vials. A constancy check of the 12 atm dose calibrator was completed with a $^{137}Cs$ tube source prior to the $^{90}YCl_3$ solution measurements. As mentioned in Section 2.6, the response of a dose calibrator can drift due to the leaking of its pressurized argon.

A description of the $^{90}YCl_3$ standard radioactivity solution provided annually by NIST is given in Section 4.2.1. Measurements of the flame-sealed ampoule (FSA) containing

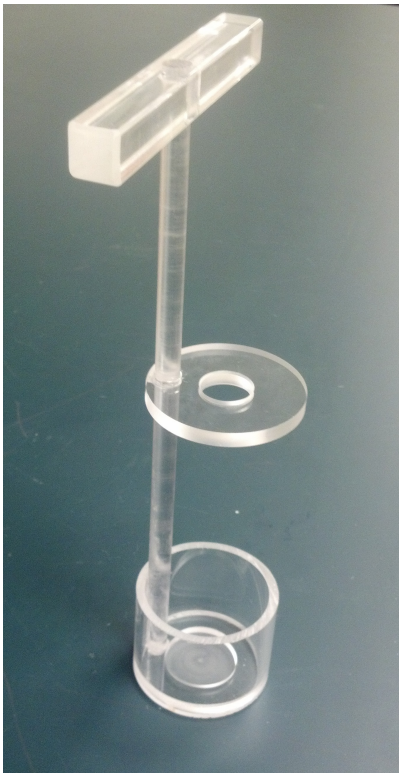

Figure 5.5: Photograph of the "dipper" source holder used with the Capintec 12 atm dose calibrator.

the $^{90}YCl_3$ solution were made in both the well chamber and the dose calibrator with the constructed holder. The FSA was then opened, and the solution was removed using a stainless steel needle and a 10 mL syringe. The shipping vial and v-vial were filled with the nominal volumes of the $^{90}YCl_3$ solution from 1 mL to 5 mL in 1 mL increments. Venting needles were placed in the rubber septa of the vials during the transfer of the $^{90}YCl_3$ solution between the vials. Measurements were completed in both chambers for each volume level with both vials using the constructed holders. Measurements of the shipping vial were also completed in the dose calibrator with the dipper holder. All measurements consisted of 30 s charge readings. Between each charge reading, the source vial was rotated 90°. The average of the four charge readings was used to calculate the ionization current for each measurement setup.

NIST provides the $^{90}YCl_3$ solution with a massic activity (in units MBq·g$^{-1}$). A Sartorius (Goettingen, Germany) balance with 0.1 mg resolution was used to determine the mass of the $^{90}YCl_3$ solution for each measurement setup. Therefore, the activity of the solution for each measurement setup was known. Using the known activity and ionization current from each measurement, calibration coefficients (in units MBq/pA) were calculated for each combination of volume, vial, chamber, and source holder. All calibration coefficients were corrected to the reference date given by NIST. The calibration coefficients for the different volume levels were compared for each of the measurement geometries.

### 5.2.3 Calculation of actual activity delivered

The methods for preparing the prescription activity of the SIR-Sphere for delivery to the patient were described in Section 5.1.1. To evaluate how the differences in the calibration coefficients between the volume levels would affect the delivered activity, an initial activity of 3.0 GBq was assumed for the source. Equations 5.1, 5.2, and 5.3 were used to determine the actual activity, $A_{\text{Actual}}$, that would be delivered to the patient for prescription levels of

1.2, 1.8, and 2.4 GBq, respectively, where $N_{\mathrm{A},\ X\mathrm{mL}}$ is the calibration coefficient determined for a volume of $X$ mL. This analysis was completed for each of the investigated measurement geometries and the percent differences between the actual activities and the prescription activities were calculated.

$$A_{\mathrm{Actual}} = 3\,\mathrm{GBq} - 1.8\,\mathrm{GBq}(\frac{N_{\mathrm{A},\ 3\mathrm{mL}}}{N_{\mathrm{A},\ 5\mathrm{mL}}}) \tag{5.1}$$

$$A_{\mathrm{Actual}} = 3\,\mathrm{GBq} - 1.2\,\mathrm{GBq}(\frac{N_{\mathrm{A},\ 2\mathrm{mL}}}{N_{\mathrm{A},\ 5\mathrm{mL}}}) \tag{5.2}$$

$$A_{\mathrm{Actual}} = 3\,\mathrm{GBq} - 0.6\,\mathrm{GBq}(\frac{N_{\mathrm{A},\ 1\mathrm{mL}}}{N_{\mathrm{A},\ 5\mathrm{mL}}}) \tag{5.3}$$

### 5.2.4 $^{90}$Y microsphere sample measurements

Measurements were completed with the IVB 1000 well chamber and the 12 atm dose calibrator of the $^{90}$Y microspheres (SIR-Spheres) in the shipping vial and v-vial. The microspheres were measured in both settled and agitated states for both vials. The same source holders were used as with measurements of the $^{90}YCl_3$ solution. Again, all measurements consisted of 30 s charge readings. Between each charge reading, the source vial was rotated 90°. For measurements with the microspheres in an agitated state, the microspheres were re-agitated before each charge measurement. The average of the four charge readings was used to calculate the ionization current for each measurement setup. The activity of the $^{90}$Y microspheres contained in both the shipping vial and the v-vial had been determined with the CDS. These results are presented in Section 4.7.2. Using the known activity and the ionization current from each measurement, calibration coefficients (in units MBq/pA) were calculated from each combination of the vial, chamber, and state of the microspheres within the vials. All calibration coefficients were corrected to the reference date given by Sirtex.

After measurements of the $^{90}$Y microspheres, a $^{137}$Cs tube source constancy measurement was again completed for the 12 atm dose calibrator.

## 5.3 Monte Carlo simulations

The number of well-type ionization chamber measurement geometries that were able to be investigated with the $^{90}$Y microspheres was limited by the need to determine the activity of the $^{90}$Y microspheres with the CDS for each measurement geometry. Due to the 64 h half-life of $^{90}$Y, it was not feasible to complete chamber measurements at different volume levels of $^{90}$Y microspheres in the v-vial and shipping vial, as was completed with the $^{90}YCl_3$ solution. To investigate the potential volume effects with the microspheres, Monte Carlo N-Particle 5 (MCNP5) transport code [X-5 Monte Carlo Team, 2005] was used to complete simulations of each measurement geometry of the Capintec 12 atm dose calibrator with volumes ranging from 1 to 5 mL. Measurement results of the SI IVB 1000 well chamber indicated that the chamber would not be well-suited for the clinical determination of $^{90}$Y microsphere activity (as presented in Section 5.4.1). As such, simulations with the IVB 1000 well chamber were not completed. Simulations investigating the variation in the Capintec 12 atm dose calibrator response due to variation in the vial wall thickness and the location of a source within the well of the chamber were also completed. For all simulations, the $^{90}$Y beta spectrum from the International Commission on Radiation Units and Measurements report 72 [2004] was used, as well as the step- and energy-specific energy straggling algorithm in MCNP5.

### 5.3.1 Dose calibrator model

A MCNP5 model of the Capintec 12 atm dose calibrator was created from dimensions and material specifications provided by Capintec. A form of the ideal gas law given by the equation,

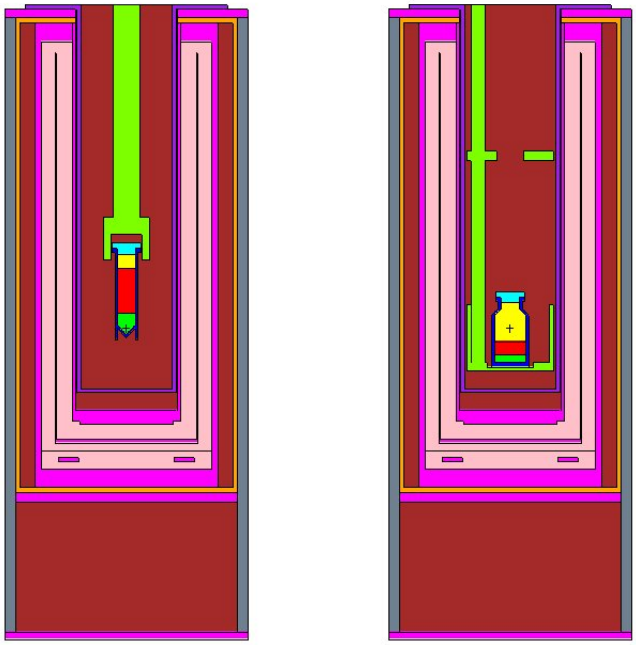

(a) (b)

Figure 5.6: Visual Editor renderings of the MCNP5 model of the Capintec 12 atm dose calibrator with (a) the constructed holder and the v-vial and (b) the dipper holder and the shipping vial.

$$\rho = \frac{MW \cdot P}{R \cdot T}, \tag{5.4}$$

was used to estimate the density, $\rho$, of the nominal 12 atm of argon filling the sensitive volume of the dose calibrator; where $MW$ is molecular weight, $P$ is pressure, $R$ is the ideal gas constant, and $T$ is temperature.

The three measurement geometries: the shipping vial in the dipper holder, the shipping vial in the constructed holder, and the v-vial in the constructed holder were implemented into the dose calibrator model. Figure 5.6 shows Visual Editor model renderings of two measurement geometries.

### 5.3.2 Source models

#### 5.3.2.1 Vial models

The shipping vial and the v-vial were modeled from dimensions obtained with caliper measurements. As described in Section 4.5, the outer dimensions of the vial and the fluid height were determined and then one of each of the vials was sacrificed to determine the thickness of the vial walls and to determine the dimensions of the "v" in the v-vial. Sirtex Medical stated that the shipping vial was composed of borosilicate glass and the v-vial was composed of polycarbonate [Sirtex Medical, 2011]. Material definitions of polycarbonate and borosilicate glass were obtained from the NIST online database [Berger et al., 2005]. Sirtex Medical also provided that the nominal wall thickness of the v-vial was 2 mm.

#### 5.3.2.2 $^{90}YCl_3$ solution volume dependence simulations

Due to uncertainties associated with some of material definitions used in the MCNP5 dose calibrator model (such as the density of the argon filling the sensitive volume), it was important to assess the ability of the model to accurately predict the relative response of the dose calibrator. The volume dependence measurements of the $^{90}YCl_3$ solution were compared to the relative response of simulations with the same geometry. The $^{90}YCl_3$ solution was modeled using the same methods described in Section 4.5. The material definition was created based on the information provided in the calibration certificate given by NIST. Simulations were completed with volumes of the $^{90}YCl_3$ solution ranging from $1-5$ mL in 1 mL increments for each of the three vial and holder configurations. All simulations were run with a sufficient number of particles to achieve statistical uncertainties of less than 0.7 %. The simulation and measurement results were normalized to the respective 5 mL result for comparison.

#### 5.3.2.3 Microspheres volume dependence simulations

It is recommended that a sample of SIR-Spheres be agitated prior to measurement in a dose calibrator [Dezarn et al., 2011]. This theoretically results in a uniform distribution of microspheres within the water. It was impractical to model the individual microspheres (typically 60 million) present in a SIR-Spheres sample. Therefore, the microsphere and water suspension was modeled as a single, uniform material. The exact material composition of SIR-Spheres was unavailable as this is proprietary information held by Sirtex Medical. For this work, polystyrene was assumed for the microsphere material. Volume dependence simulations were repeated with three separate materials representing the agitated microspheres and water suspension. These materials were polystyrene, water, and a combination of polystyrene and water. The polystyrene alone and water alone simulations represented the extreme cases, while the simulations with the polystyrene/water combination represented a more realistic case. The ratio of the polystyrene and water for the realistic case was based on the ratio of the volume occupied by microspheres and by water. This ratio was calculated based on the average number of microspheres in a sample (60 million) and the average volume of each microsphere (from the average diameter of 32 $\mu$m). The same density was used for all three materials. The density was also calculated based on the proportion of microspheres-to-water in a SIR-Spheres sample. The relative proportions were used to weight an average of the microsphere density of 1.6 $\mathrm{g{\cdot}cm^{-3}}$ and the water density of 1.0 $\mathrm{g{\cdot}cm^{-3}}$. This weighted average was 1.123 $\mathrm{g{\cdot}cm^{-3}}$.

Simulations were completed with volumes of the microsphere and water suspension from $1-5$ mL in 1 mL increments for each of the three vial and holder configurations and the three materials. All simulations were run with a sufficient number of particles to achieve statistical uncertainties of less than 0.7 %. The simulation results were normalized to their respective 5 mL result for comparison. Based on the relative response determined from these simulations, the same evaluation investigating the actual activity that would be delivered

Table 5.1: Measured wall thicknesses at 90° intervals of the shipping vial and v-vial with the average and standard deviation of the measurements.

| | Wall thickness (mm) | |
|---|---|---|
| Measurement | V-vial | Shipping vial |
| 1 | 2.06 | 1.75 |
| 2 | 2.12 | 2.37 |
| 3 | 1.77 | 2.03 |
| 4 | 1.98 | 1.84 |
| Average: | 1.98 | 2.00 |
| Std. Dev.: | 0.15 | 0.27 |

to the patient compared to the prescribed value due to the volume dependencies of the the measurement setup (as described in Section 5.2.3) was completed. These results were compared to the results from the $^{90}YCl_3$ solution measured values.

### 5.3.3 Variation with vial wall thickness

Sirtex Medical provided the material of the shipping vial and the v-vial, as well as a nominal wall thickness of 2 mm for the v-vial [Sirtex Medical, 2011]. However, the tolerance of the wall thicknesses for both vials was unavailable. A variation in the wall thickness of a vial may cause a variation in the response of the dose calibrator. Four caliper measurements of the vial wall thickness were completed at 90° intervals for both a sacrificed v-vial and shipping vial. The results of these measurements are shown in Table 5.1. All previously discussed simulations were completed with vial wall thicknesses of 2 mm for both the v-vial and the shipping vial. Simulations to investigate variation in the dose calibrator response due to variations in vial wall thickness were completed for vial wall thicknesses at approximately plus or minus one and two standard deviations from the average measured thickness values. That is, simulations were completed with wall thicknesses of 1.70, 1.85, 2.15, and 2.30 mm for the v-vial and with wall thicknesses of 1.5, 1.75, 2.25, and 2.5 mm for the shipping vial. All simulations were completed with the source defined as 5 mL of the microsphere and water suspension using the realistic combination of polystyrene and

water as the material definition, and a sufficient number of particles were transported to achieve statistical uncertainties of less than 0.7 %. Only the outer diameters of the vials were changed to ensure the position of the source material remained constant. The results of these simulations were compared to previous baseline simulations with 2 mm vial wall thicknesses.

### 5.3.4 Variation with source position

The response of a dose calibrator can vary due to the location of the source within the well of the chamber. To characterize this effect for the Capintec 12 atm dose calibrator, simulations of a $^{90}$Y point source in a 5 mm radius water sphere were completed at 0.5, 2.375, 4.25, 6.125, 8.0, 9.875, 11.75, 13.625, 15.5, 19.25, and 23.0 cm from the polycarbonate liner near the bottom of the well of the dose calibrator. All simulations were run with a sufficient number of particles to achieve statistical uncertainties of less than 0.8 %. The results of these simulations were compared to the location of the source material in the three investigated measurement geometries to analyze how the response of the dose calibrator varied in these regions.

## 5.4 Results

### 5.4.1 Measurements

#### 5.4.1.1 $^{90}YCl_3$ standard activity solution

Figure 5.7 shows plots of the inverse calibration coefficient (which is proportional to the response of the well-type ionization chambers) versus the nominal volume of the $^{90}YCl_3$ solution for the five investigated measurement setups. The results with the IVB 1000 well chamber with both the v-vial and the shipping vial showed a decrease in response with an increase in volume, which indicated volume dependencies for these measurement

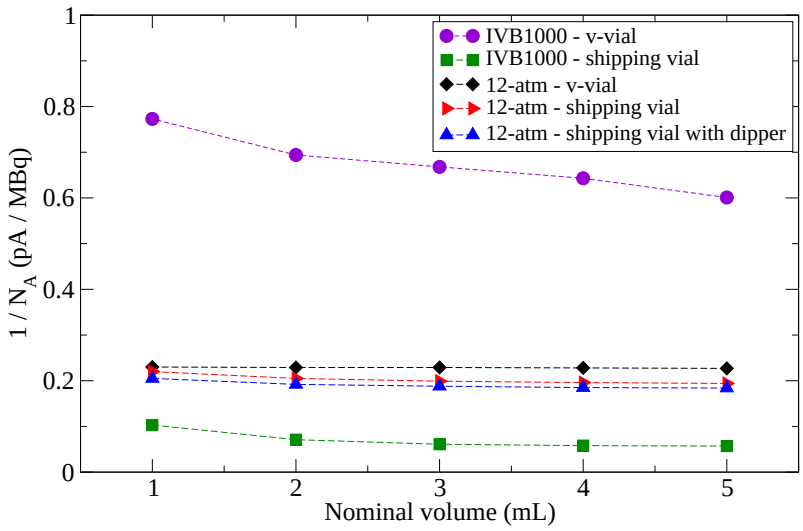


Figure 5.7: Plot of the well-type ionization chamber responses for each measurement setup versus the nominal volume of the $^{90}YCl_3$ solution.

geometries. For the IVB 1000 well chamber results, there was approximately an order of magnitude difference in the response of the chamber between measurements with the v-vial and measurements with the shipping vial. The inner well wall of the IVB 1000 well chamber is constructed of butyrate and is approximately 0.8 mm thick. This much thinner than the 2.6-mm-thick aluminum wall of the 12 atm dose calibrator, which additionally had the 3.0-mm-thick polycarbonate liner in place during measurements. Laedermann et al. [2004] found that the response of a well-type ionization chamber to beta-emitting sources increases rapidly once direct interactions of betas in the sensitive gas volume of chamber the starts to occur. The large variation between the measurements completed with the two vials in the IVB 1000 well chamber was likely due to direct interactions of the $^{90}Y$ beta particles in the sensitive air volume of the chamber during measurements with the v-vial. This effect was most likely reduced during measurements with the shipping vial due to the increased self-absorption of the $^{90}Y$ beta particles with the larger diameter vial.

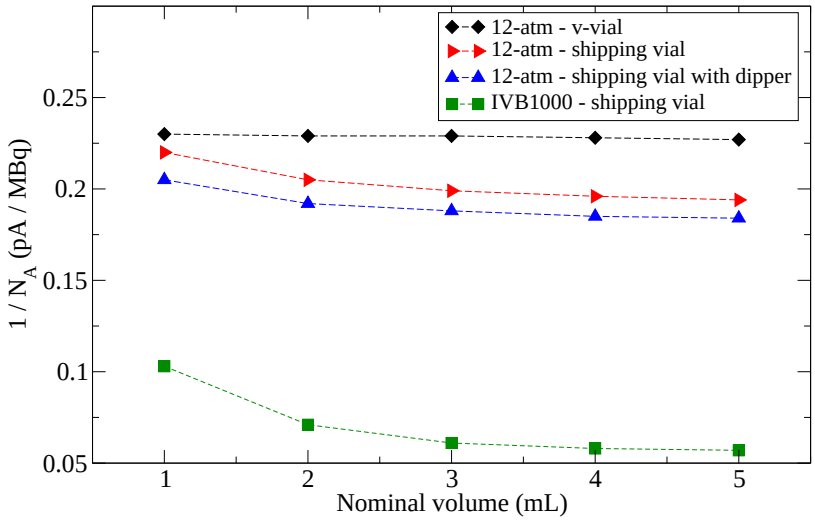


Figure 5.8: Plot of the well-type ionization chamber responses for some of the measurement setups versus the nominal volume of the $^{90}YCl_3$ solution on a reduced scale.

Figure 5.8 shows some of the data from Figure 5.7, but on a smaller scale such that the shape of the 12 atm dose calibrator response plots can be visualized. The data for the dose calibrator for both configurations with the shipping vial showed volume dependence as there was a decrease in response with increasing volume. The response of the dose calibrator with the v-vial showed a flat response across the investigated volumes, indicating volume independence for this measurement setup.

The same calibration coefficient data from Figures 5.7 and 5.8 are presented in Tables 5.2 and 5.3 for the IVB 1000 well chamber and the 12 atm dose calibrator, respectively. Included in the tables are the percent differences from the respective 5 mL calibration coefficient. In Table 5.2, it is shown that the response of the IVB 1000 well chamber can vary by as much as 22 % with the v-vial and as much as 45 % with the shipping vial due to the volume of the source. The variation in response of the 12 atm dose calibrator with change in volume was shown to be less than the IVB 1000 well chamber. However, for both measurement

Table 5.2: Measured calibration coefficients for the SI IVB 1000 well chamber with the v-vial and the shipping vial at different volumes of the NIST SRM $^{90}YCl_3$ solution. The percent difference from the 5 mL calibration coefficient is also given for each vial.

| Volume (mL) | V-vial | | Shipping vial | |
|---|---|---|---|---|
| | Calibration coefficient (MBq/pA) | Difference from 5 mL (%) | Calibration coefficient (MBq/pA) | Difference from 5 mL (%) |
| 5 | 1.663 | – | 17.65 | – |
| 4 | 1.556 | -6.43 | 17.38 | -1.51 |
| 3 | 1.496 | -10.0 | 16.33 | -7.46 |
| 2 | 1.441 | -13.4 | 13.99 | -20.7 |
| 1 | 1.294 | -22.2 | 9.682 | -45.1 |

setups with the shipping vial, the dose calibrator still showed a maximum variation of over 10 % due to change in volume. The relatively small variation in response with change in volume that was seen in Figure 5.8 with the v-vial in the dose calibrator is shown to have a maximum variation of 1.3 %.

The effects of the volume dependencies of the investigated well-type ionization chambers on the activities delivered to patients were assessed. For an assumed initial activity of 3 GBq, the actual activities that would be delivered for three prescription activities are shown in Tables 5.4 and 5.5 for the IVB 1000 well chamber and the 12 atm dose calibrator, respectively. The actual activities varied from the prescription activities for the IVB 1000 well chamber by 5.5 to 15 % for the v-vial and by 11 to 14 % for the shipping vial. The lower volume dependence of the Capintec 12 atm dose calibrator resulted in less variation in the actual activities from the prescription activities. With the shipping vial in both measurement configurations in the 12 atm dose calibrator, the actual activity was approximately 3 % higher than the prescription activity for all prescription levels. The differences with the shipping vial in the constructed holder ranged from 2.9 to 3.7 %, and the differences with the shipping vial in the dipper holder ranged from 2.6 to 2.9 %. The v-vial had the lowest differences in the actual activities from the prescription activities, which ranged from 0.33 to 1.2 %.

Table 5.3: Table of the measured calibration coefficients for the Capintec 12 atm dose calibrator with the v-vial and the shipping vial at different volumes of the NIST SRM $^{90}YCl_3$ solution. The percent difference from the 5 mL calibration coefficient is also given for each measurement geometry.

| Volume (mL) | V-vial | | Shipping vial | | Shipping vial in dipper | |
|---|---|---|---|---|---|---|
| | Calibration coefficient (MBq/pA) | Difference from 5 mL (%) | Calibration coefficient (MBq/pA) | Difference from 5 mL (%) | Calibration coefficient (MBq/pA) | Difference from 5 mL (%) |
| 5 | 4.406 | – | 5.152 | – | 5.436 | – |
| 4 | 4.377 | -0.665 | 5.114 | -0.750 | 5.418 | -0.324 |
| 3 | 4.372 | -0.779 | 5.026 | -2.44 | 5.331 | -1.92 |
| 2 | 4.375 | -0.714 | 4.883 | -5.23 | 5.211 | -4.14 |
| 1 | 4.349 | -1.30 | 4.549 | -11.7 | 4.872 | -10.4 |

Table 5.4: Comparison of the prescription (Rx) activities and the actual activities that would be delivered due to the volume effects of the IVB 1000 well chamber with the v-vial and the shipping vial as determined from measurements with the $^{90}YCl_3$ solution.

| | V-vial | | Shipping vial | |
|---|---|---|---|---|
| Rx activity (GBq) | Actual activity (GBq) | Difference from Rx (%) | Actual activity (GBq) | Difference from Rx (%) |
| 2.4 | 2.53 | 5.5 | 2.67 | 11 |
| 1.8 | 1.96 | 8.9 | 2.05 | 14 |
| 1.2 | 1.38 | 15 | 1.33 | 11 |

The large volume dependencies and resulting large differences in the delivered activity from the prescription activity with the IVB 1000 well chamber indicated that this device would not be ideal for use as a clinical measurement device for determining the activity of SIR-Spheres.

#### 5.4.1.2 $^{90}$Y microspheres

The measured calibration coefficients for SIR-Spheres in the SI IVB 1000 and the Capintec 12 atm dose calibrator are given in Tables 5.6 and 5.7, respectively. Calibration coefficients are given for the microspheres in both an agitated and a settled state, and the percent difference of the settled state from the agitated state is provided. For the IVB 1000 well chamber, the greatest difference between the agitated and settled state was seen with the shipping vial and was just over 6 %. With the v-vial, the difference was 1.35 %. For the 12 atm dose calibrator, the largest difference between the agitated and settled state was with the v-vial at 0.958 %. However, the differences for all of measurement configurations with the 12 atm dose calibrator were less than 1 %.

Tables 5.8 and 5.9 compare the percent differences of the agitated SIR-Spheres calibration coefficients in the investigated measurement geometries from calibration coefficients of various other source and vial configurations for the SI IVB 1000 well chamber and the Capintec 12 atm dose calibrator, respectively. For this comparison, the calibration coefficients for the$^{90}YCl_3$ solution and the SIR-Spheres with the Capintec 12 atm dose calibrator

Table 5.5: Comparison of the prescription (Rx) activities and the actual activities that would be delivered due to the volume effects of the 12 atm dose calibrator with the v-vial and the shipping vial as determined from measurements with the $^{90}YCl_3$ solution.

| | V-vial | | Shipping vial | | Shipping vial in dipper | |
|---|---|---|---|---|---|---|
| Rx activity (GBq) | Actual activity (GBq) | Difference from Rx (%) | Actual activity (GBq) | Difference from Rx (%) | Actual activity (GBq) | Difference from Rx (%) |
| 2.4 | 2.41 | 0.33 | 2.47 | 2.9 | 2.46 | 2.6 |
| 1.8 | 1.81 | 0.48 | 1.86 | 3.5 | 1.85 | 2.8 |
| 1.2 | 1.21 | 1.2 | 1.24 | 3.7 | 1.23 | 2.9 |

Table 5.6: Measured calibration coefficients for the SI IVB 1000 well chamber with resin $^{90}$Y microspheres agitated and settled at the bottom of the both the v-vial and the shipping vial . The percent difference between the calibration coefficients for agitated and settled microspheres is also given for each vial.

| State of microspheres in vial | V-vial | | Shipping vial | |
|---|---|---|---|---|
| | Calibration coefficient (MBq/pA) | Difference from agitated (%) | Calibration coefficient (MBq/pA) | Difference from agitated (%) |
| Agitated | 1.722 | – | 14.22 | – |
| Settled | 1.745 | 1.35 | 15.08 | 6.07 |

were normalized to the respective measured $^{137}$Cs tube source calibration coefficients. The calculated calibration coefficients (in U/nA) from the two $^{137}$Cs tube measurements differed by less than 0.2 %.

Previous studies have determined that errors as high as 50 % can occur when completing dose calibrator measurements of $^{90}$Y sources in geometries differing from the calibration geometry [Zimmerman and Cessna, 2000, Wastiel et al., 2005]. The NIST standard geometry is a 5 mL FSA and is commonly used to calibrate dose calibrators for the determination of activity. As shown in Table 5.8, potential errors as high as 1300 % could occur in determining the SIR-Spheres activity from the IVB 1000 well chamber measurements if the NIST geometry was used to calibrate the chamber. Again, this large difference is most likely due to the direct contribution of betas to the ionization current for measurements with the smaller FSA compared to the shipping vial, as discussed in Section 5.4.1.1. These potential errors were found to be lower with the 12 atm dose calibrator, as shown in Table 5.9, where the differences between calibration coefficients with the SIR-Spheres and the $^{90}YCl_3$ solution in a FSA ranged from 2.61 to 27.0 %.

Using a Capintec model CRC-15R dose calibrator, Dezarn and Kennedy [2007] found a 20 % difference between measurements of SIR-Spheres in a shipping vial and a v-vial. Results from the Capintec 12 atm dose calibrator (which is similar to the CRC-15R) measurements in this work are in agreement with Dezarn and Kennedy [2007], with differences

Table 5.7: Measured calibration coefficients for the Capintec 12 atm dose calibrator with resin $^{90}$Y microspheres agitated and settled at the bottom of the both the v-vial and the shipping vial. The percent difference between the calibration coefficients for agitated and settled microspheres is also given for each measurement setup.

| State of microspheres in vial | V-vial | | Shipping vial | | Shipping vial in dipper | |
|---|---|---|---|---|---|---|
| | Calibration coefficient (MBq/pA) | Difference from agitated (%) | Calibration coefficient (MBq/pA) | Difference from agitated (%) | Calibration coefficient (MBq/pA) | Difference from agitated (%) |
| Agitated | 4.483 | – | 5.189 | – | 5.548 | – |
| Settled | 4.526 | 0.958 | 5.174 | -0.298 | 5.542 | -0.101 |

Table 5.8: Percent differences of the SI IVB 1000 well chamber calibration coefficients for the agitated SIR-Spheres in the v-vial and shipping vial from other measured calibration coefficients for various source and vial configurations.

| | Difference (%) | |
|---|---|---|
| Source and vial | V-vial | Shipping vial |
| $^{90}YCl_3$ solution in FSA | 69.8 | 1300 |
| $^{90}YCl_3$ solution in v-vial | 3.52 | – |
| $^{90}YCl_3$ solution in shipping vial | – | -19.4 |
| SIR-Spheres in v-vial | 0.00 | 726 |

Table 5.9: Percent differences of the Capintec 12 atm dose calibrator calibration coefficients for the agitated SIR-Spheres in the v-vial, shipping vial, and shipping vial in the dipper from other measured calibration coefficients for various source and vial configurations.

| | Difference (%) | | |
|---|---|---|---|
| Source and vial | V-vial | Shipping vial | Shipping vial in dipper |
| $^{90}YCl_3$ solution in FSA | 2.61 | 18.8 | 27.0 |
| $^{90}YCl_3$ solution in v-vial | 1.53 | – | – |
| $^{90}YCl_3$ solution in shipping vial | – | 0.516 | – |
| $^{90}YCl_3$ solution in shipping vial in dipper | – | – | 1.86 |
| SIR-Spheres in v-vial | 0.00 | 15.8 | 23.8 |
| SIR-Spheres in shipping vial in dipper | -19.2 | -6.46 | 0.00 |

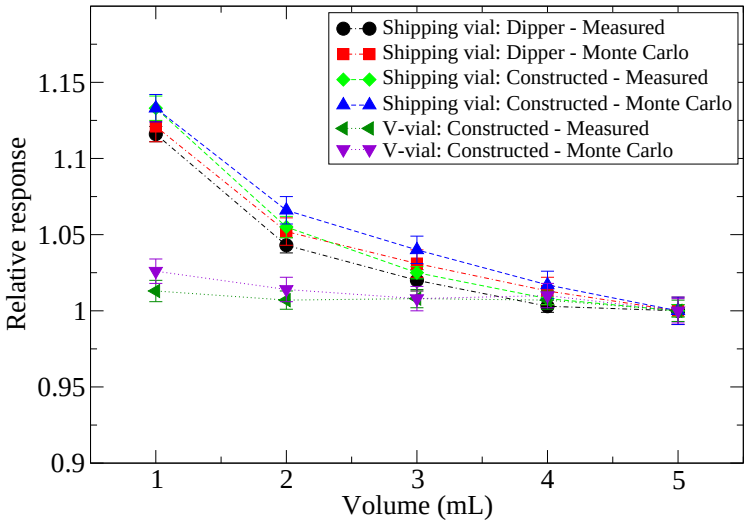


Figure 5.9: Comparison of the measured and Monte Carlo-determined relative response of the Capintec 12 atm dose calibrator versus volume of the $^{90}YCl_3$ solution for three measurement geometries. Values are normalized to the respective 5 mL value.

between measurements with the shipping vial and v-vial ranging from 15.8 to 23.8 % depending on the measurement setup. These results are shown in Table 5.9. Again with the IVB 1000 well chamber, the difference between the v-vial and the shipping vial with the SIR-Spheres was found to be large at 726 %, as shown in Table 5.8.

### 5.4.2 Monte Carlo simulations

#### 5.4.2.1 Comparison to volume dependence measurements

Figure 5.9 compares the measured and Monte Carlo-determined response of the Capintec 12 atm dose calibrator with different volumes of the $^{90}YCl_3$ solution for the three investigated measurement geometries. Each data set was normalized to its respective 5 mL value for comparison. The error bars for the Monte Carlo-determined values represent the statistical uncertainty associated with the simulations, and the error bars for the measured values

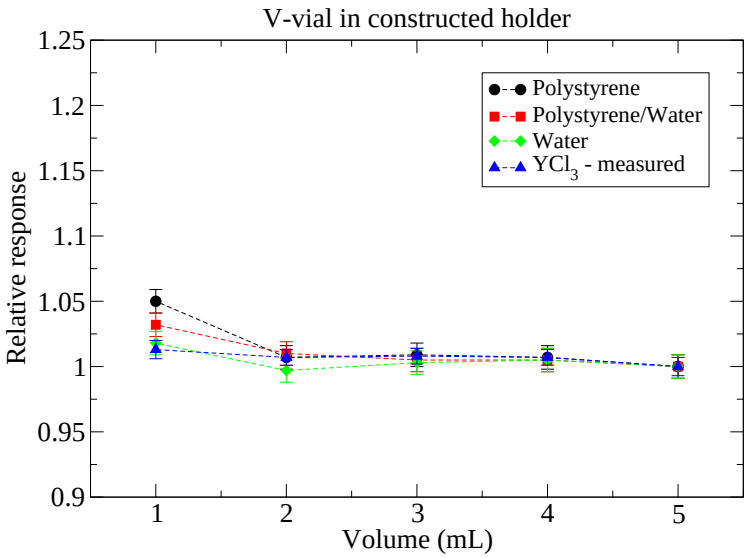


Figure 5.10: Comparison of the relative response of the Capintec 12 atm dose calibrator versus volume for the v-vial in the constructed holder with different simulated materials for the microspheres. The measured values with $^{90}YCl_3$ solution are also included. Values are normalized to the respective 5 mL value.

represent the NIST-stated activity uncertainty of the $^{90}YCl_3$ solution and the statistical uncertainty from the four dose calibrator charge measurements. It is seen that there is agreement between the measured and Monte Carlo-determined values for each of the three vial and source configurations within the expanded uncertainty associated with the data. This indicated that the Monte Carlo model of the Capintec 12 atm dose calibrator was able to predict the actual relative response of the chamber. Based on these results, the use of the model was extended to investigate the response of the chamber for other measurement geometries.

#### 5.4.2.2 Volume dependence of microspheres

Figures 5.10, 5.11, and 5.12 present the relative response of the Capintec 12 atm dose calibrator versus volume for the v-vial, the shipping vial in the constructed holder, and

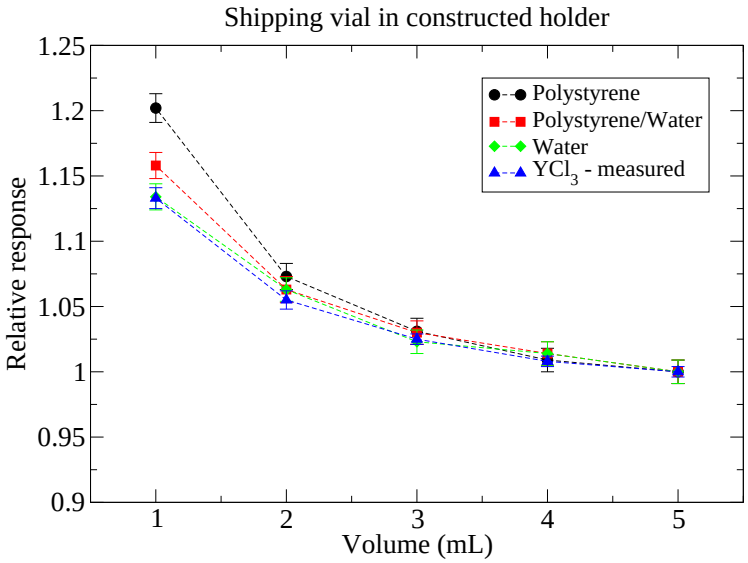


Figure 5.11: Comparison of the relative response of the Capintec 12 atm dose calibrator versus volume for the shipping vial in the constructed holder with different simulated materials for the microspheres. The measured values with $^{90}YCl_3$ solution are also included. Values are normalized to the respective 5 mL value.

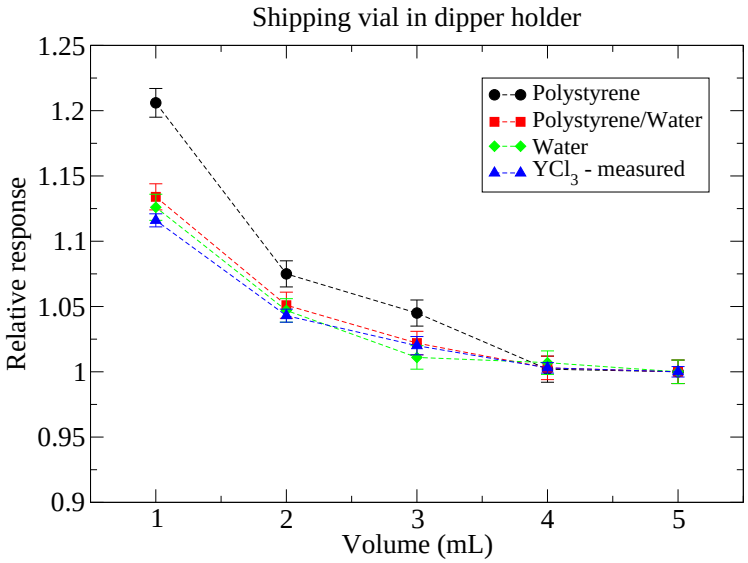


Figure 5.12: Comparison of the relative response of the Capintec 12 atm dose calibrator versus volume for the shipping vial in the dipper holder with different simulated materials for the microspheres. The measured values with $^{90}YCl_3$ solution are also included. Values are normalized to the respective 5 mL value.

the shipping vial in the dipper holder, respectively, with different simulated materials for the microspheres. For comparison, the measured $^{90}$YCl solution data was also included. All plots were normalized to their respective 5 mL value. For all three vial configurations, there was good agreement between the water simulation results and the measured $^{90}$YCl solution data. For the v-vial results presented in Figure 5.10, all plots were in agreement except at the 1 mL volume. At this volume level, the largest deviation was seen with the polystyrene simulations with a relative response of 1.050. The next largest deviation was observed for the polystyrene/water combination with a relative response of 1.032. As seen in the measured $^{90}$YCl solution data, the simulations with the shipping vial had larger variations in the relative response of the dose calibrator with change in volume. Again, the largest variation occurred at the 1 mL level with the polystyrene simulations for both shipping vial configurations. For the shipping vial in the constructed holder, the maximum relative response was 1.202 and for the shipping vial in the dipper holder, the maximum relative response was 1.206. For the polystyrene and water simulations, the maximum relative responses for the shipping vial in the constructed holder and the dipper holder were 1.158 and 1.134, respectively.

For an assumed initial activity of 3 GBq, the data presented in the Figures 5.10, 5.11, and 5.12 were used to calculate the actual activities that would be delivered for three prescription activities. These values are shown in Tables 5.10 and 5.11 for the realistic polystyrene and water combination material definition and the extreme 100 % polystyrene material definition of the microspheres, respectively. Because of the good agreement between the simulations with water as the source material and the measurements with the $^{90}YCl_3$ solution, this analysis was not completed using the water simulation data.

As seen with the $^{90}YCl_3$ solution data, the greater volume dependencies with the shipping vial lead to larger variations between the prescription activity and the actual activity. Comparing the calculated values in Table 5.10 from the polystyrene and water combination

Table 5.10: Comparison of the prescription (Rx) activities and the actual activities that would be delivered due to the volume effects of the Capintec 12 atm dose calibrator with the v-vial and the shipping vial as determined from Monte Carlo simulations of the microsphere material modeled as the realistic case of a polystyrene and water combination.

| | V-vial | | Shipping vial | | Shipping vial in dipper | |
|---|---|---|---|---|---|---|
| Rx activity (GBq) | Actual activity (GBq) | Difference from Rx (%) | Actual activity (GBq) | Difference from Rx (%) | Actual activity (GBq) | Difference from Rx (%) |
| 2.4 | 2.42 | 0.81 | 2.48 | 3.4 | 2.47 | 2.9 |
| 1.8 | 1.81 | 0.67 | 1.87 | 3.9 | 1.86 | 3.2 |
| 1.2 | 1.21 | 0.77 | 1.25 | 4.4 | 1.24 | 3.2 |

Table 5.11: Comparison of the prescription (Rx) activities and the actual activities that would be delivered due to the volume effects of the Capintec 12 atm dose calibrator with the v-vial and the shipping vial as determined from Monte Carlo simulations of the microsphere material modeled as the extreme case of 100 % polystyrene.

| | V-vial | | Shipping vial | | Shipping vial in dipper | |
|---|---|---|---|---|---|---|
| Rx activity (GBq) | Actual activity (GBq) | Difference from Rx (%) | Actual activity (GBq) | Difference from Rx (%) | Actual activity (GBq) | Difference from Rx (%) |
| 2.4 | 2.43 | 1.2 | 2.50 | 4.2 | 2.50 | 4.3 |
| 1.8 | 1.81 | 0.49 | 1.88 | 4.6 | 1.88 | 4.6 |
| 1.2 | 1.22 | 1.3 | 1.25 | 4.6 | 1.28 | 6.5 |

simulations to the calculated values in Table 5.5 from the $^{90}YCl_3$ solution measurements, it is seen that for the microsphere material (for the realistic case) results in a slight increase in the deviations of the delivered activity from the prescription activity for the shipping vial configurations with the difference range increasing from $2.6 - 3.7\,\%$ to $2.9 - 4.4\,\%$. For the simulations with the source material definition of $100\,\%$ polystyrene, these deviations are greater with the differences ranging from $4.2 - 6.5\,\%$. This is seen by comparing the values in Table 5.11 with the values in Tables 5.5 and 5.10 for the shipping vial configurations.

The differences between the actual activity and the prescription activity are again the lowest with the v-vial. From simulations with the polystyrene and water combination, the calculated differences were all below $1\,\%$, as shown in Table 5.10. For simulations with the extreme case of $100\,\%$ polystyrene, the maximum difference was $1.3\,\%$, which is just slightly above the maximum difference determined from the measured $^{90}YCl_3$ solution data of $1.2\,\%$. These results indicated that the v-vial would be the favored measurement vial over the shipping vial due to the decreased volume dependencies which result in decreased differences between the intended and delivered activity with SIR-Spheres.

#### 5.4.2.3 Variation with vial wall thickness

Table 5.12 presents the variation in the response of the 12 atm dose calibrator for various vial wall thicknesses relative to a vial wall thickness of 2 mm. The differences seen with the various wall thicknesses of the v-vial were all within the $0.7\,\%$ statistical uncertainty associated with the Monte Carlo simulations. This indicated that these wall thickness have very little effect on the response of the dose calibrator. The differences seen with the shipping vial in the two measurement setups had difference values above the $0.7\,\%$ statistical uncertainty associated with the Monte Carlo simulations. As would be expected, the thickness values less than 2 mm showed an increased response of the dose calibrator, and thickness values more than 2 mm showed a decreased response of the dose calibrator.

Table 5.12: Percent differences in the Monte Carlo-determined response of the Capintec 12 atm dose calibrator with various vial wall thicknesses compared to a vial wall thickness of 2 mm.

| Wall thickness (mm) | Difference from 2 mm (%) | | |
|---|---|---|---|
| | V-vial | Shipping vial | Shipping vial in dipper |
| 1.70 | -0.36 | – | – |
| 1.85 | 0.12 | – | – |
| 2.15 | 0.32 | – | – |
| 2.30 | -0.13 | – | – |
| 1.50 | – | 0.67 | 1.4 |
| 1.75 | – | 0.51 | 0.65 |
| 2.25 | – | -0.54 | -0.73 |
| 2.50 | – | -0.98 | -1.3 |

The differences seen with the shipping vial in the constructed holder were all within 1 %. The differences seen with the shipping vial in the dipper were greater, ranging from −1.3 % to 1.4 %. These results indicated that measurements of SIR-Spheres with the v-vial in the dose calibrator would be the least susceptible to variations in thickness of the vial wall.

#### 5.4.2.4 Variation with source position

Figure 5.13 shows the results of the point source simulations at various locations along the axis of the Capintec 12 atm dose calibrator MCNP5 model. The results were normalized to the point of maximum response, which was 8.0 cm above the bottom of the polycarbonate well liner. The shaded regions in Figure 5.13 represent the position of 5 mL of liquid in the shipping vial or v-vial for the three investigated measurement geometries. The response of the dose calibrator was found to be flat within 1 % for the region from 6.125 cm to 11.75 cm. Note that none of the measurement geometries fell completely within this region of flat response. The response gradient with position in the regions occupied by 5 mL for each measurement setup created a competing effect with the change in volume, particularly for the shipping vial in the dipper. As shown in the plots of relative response versus volume, as the volume decreased, the response increased. The volume decrease caused a shift in

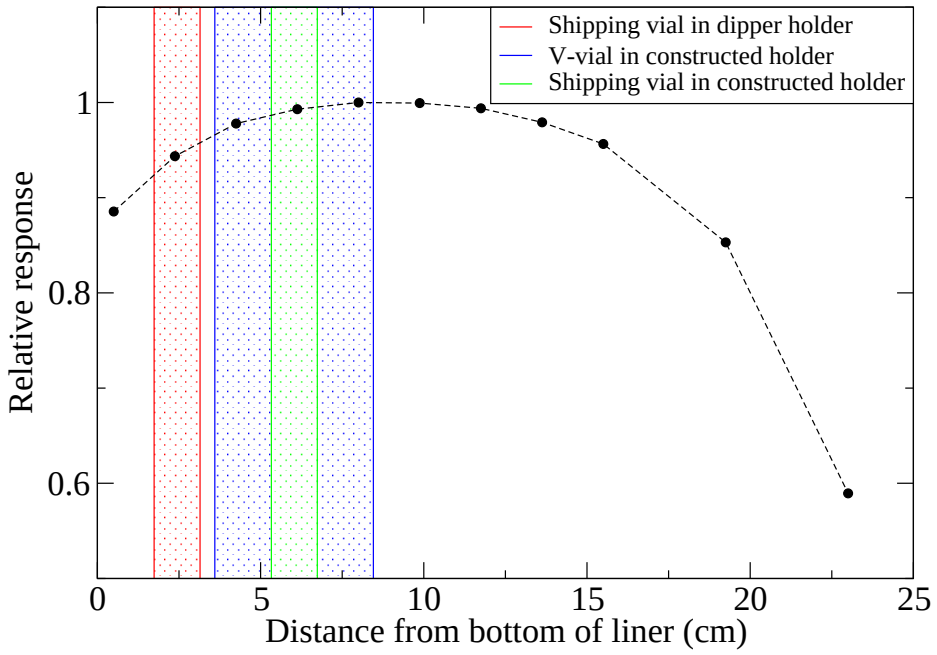


Figure 5.13: Plot of the Monte Carlo-determined relative response of the Capintec 12 atm dose calibrator to a $^{90}$Y point source in a 5 mm radius of water at various locations from the bottom of the dose calibrator well liner. The color shaded regions represent the location of the source material for each of the measurement geometries.

Table 5.13: Uncertainty budget for the calibration coefficient of SIR-Spheres in the v-vial for the Capintec 12 atm dose calibrator.

| | Uncertainty | |
|---|---|---|
| Parameter | Type A (%) | Type B (%) |
| Charge | 0.18 | 0.05 |
| Half-life | – | 0.03 |
| Source positioning | – | 0.30 |
| Source volume | – | 1.0 |
| Vial thickness | – | 0.60 |
| Normalization to $^{137}$Cs tube source | 0.20 | 0.20 |
| Electrometer voltage | 0.02 | 0.10 |
| Electrometer charge readout error | 0.05 | 0.10 |
| Electrometer timing error | 0.05 | 0.10 |
| Source activity | 0.82 | 1.78 |
| Quadratic sum | 0.87 | 2.17 |
| Combined uncertainty | 2.33 | |
| Expanded combined uncertainty ($k = 2$) | 4.66 | |

position of the source material toward the bottom of the well of the chamber. This change in position caused a decrease in response. Moving the measurement location to the region of uniform response would isolate the volume effects. The evaluated volume effects would potentially be larger in magnitude, but would be independent of source position, meaning potential volume corrections would be more accurate.

## 5.5 Conclusions

Both an IVB 1000 well chamber and a 12 atm dose calibrator were characterized for their use as a clinical measurement device that could be used to determine that activity of a SIR-Spheres sample. The IVB 1000 well chamber was found to exhibit large volume dependencies for $^{90}YCl_3$ solution measurements. These dependencies lead to large differences between the prescription activity and the actual activity that would be delivered to a patient. Because

of these results, the IVB 1000 well chamber would not be an ideal measurement device for the clinical determination of SIR-Spheres activity.

The IVB 1000 well chamber was included in this investigation as the calibration protocol associated with radiation oncology-type well chambers allows for calibration in the same measurement geometry that is used clinically. However, The IVB 1000 well chamber was found to not be an ideal clinical measurement device for SIR-Spheres. The same proposed methodology could be applied to dose calibrators, but dose calibrators are not typically shipped to an ADCL for calibration. Additionally, dose calibrators typically being pressurized chambers complicates their potential for being sent to an ADCL due to the HAZMAT regulatory restrictions on shipping pressurized equipment. This creates a logistical problem with establishing a calibration program based on the protocol used with radiation oncology well chambers. To establish a calibration protocol using the CDS as a standard measurement device for determining the activity of $^{90}$Y microspheres, a hybrid of the radiation oncology and the nuclear medicine protocol would need to be implemented. This could involve a physicist acquiring a microsphere sample from the manufacturer, making measurements in their dose calibrator, and then sending the sample to an ADCL. The activity of the sample could then be determined with the CDS (or possibly with a reference well-type ionization chamber traceable to the CDS). The clinical physicist would have to ensure that the measurement geometry used in the initial measurement would continue to be used with future measurements and that a consistent dial setting would be used.

This work has shown that calibration and measurements with the v-vial would provide a more accurate determination of the activity of $^{90}$Y microspheres from dose calibrator measurements compared to the shipping vial that is presently used. The v-vial was shown to produce less variation in the response of the dose calibrator with different volumes and vial wall thicknesses compared to the shipping vial. Additionally, calibration and measurement in the v-vial would provide more accurate post-treatment activity assays. There are

occasions with the SIR-Spheres treatment that a point of stasis is reached and the microspheres are no longer flowing into the patient's vasculature [Kennedy et al., 2007]. In these situations the treatment is terminated. For these situations, it would be advantageous to be able to assay the remaining activity in the v-vial that was not delivered to the patient. Calibration with the v-vial would provide the ability to complete this assay accurately. Table 5.13 provides the uncertainty budget for the calibration coefficient of SIR-Spheres in the v-vial for the Capintec 12 atm dose calibrator based on the results presented in this chapter, as well as Chapter 4, and the evaluation techniques typically employed by the UW ADCL [UWADCL, 2006].

This work has focused on the SIR-Spheres $^{90}$Y microsphere product. The TheraSphere product does not use the same activity preparation methods, so the product would not be subject to the same variations in the actual activity delivered from the prescription activity due to the volume dependence of the well-type ionization chambers used for the clinical determination of activity. Rather than drawing out the desired activity from a sample, the TheraSphere product is shipped at different activity levels. This allows the user of the product to select the appropriate activity based on the scheduled time of the microsphere delivery. However, the various activity levels mean that the number of microspheres in the vial will also vary. This change in the number of microspheres contained in the vial could have an effect of the response of the dose calibrator used to clinically determine the activity of the sample. Investigation of these effects is a potential area of future work.

# Chapter 6

# Microsphere-specific dose kernels

## 6.1 Introduction

Image-based dosimetry for $^{90}$Y microspheres was described in Section 2.7, where dose distribution calculation methods used in radioimmunotherapy (RIT) have been extended to the microspheres. Unlike RIT, where radioactive atoms are attached to antibodies (i.e., nanometer scale), microspheres are larger (i.e., micrometer scale) and have radioactive material throughout their volume or surface. Recent work by Guimaraes et al. [2010] used the Low Energy physics model in the Monte Carlo transport code Geant4 [S. Agostinelli et al., 2003] to calculate the dose-rate distributions around both $^{32}$P and $^{90}$Y glass microspheres in water. They presented plots of the emitted electron energy spectrum from various sizes of microspheres and a point source. These plots showed that the emitted electron energy spectrum was deformed when the glass material was present compared to point source simulations, with the glass material reducing the number of emitted electrons, particularly at lower energies. This suggested that the construction of the source may cause a difference in the dose kernel.

Guimaraes et al. [2010] validated their calculations by comparing $^{90}$Y point source simulations to reference data in the International Commission on Radiation Units and Mea-

surements Report 72 (ICRU 72) [2004]. Near the maximum range of $^{90}$Y (1.1 cm in water), Guimaraes et al.'s point source simulation results were more than 50 % lower than the ICRU 72 reference data. They noted that this deviation was due to differences in the stopping power data for water used by the Low Energy physics model of Geant4 and ICRU 72. Guimaraes et al. also presented a table of dose-rate distributions determined from simulations with a glass $^{90}$Y microsphere source. However, when these data were compared to the ICRU 72 data, they were found to be more than 25 % higher than the reference data near the maximum range of $^{90}$Y (even though the glass has a density more than three times that of water). This would imply that the presence of the glass actually increased the dose at a distance from the source center, which was not likely. These results warranted further investigation.

Dose kernel calculations with Monte Carlo techniques can differ due to a number of variables including electron transport methods, energy spectrum, and cross-sectional data. This chapter presents work that used the Monte Carlo transport codes Electron Gamma Shower (EGSnrc) [Kawrakow, 2000a,b] and Monte Carlo N-Particle (MCNP5) [X-5 Monte Carlo Team, 2005] to further evaluate the effects of glass microsphere material on the determined dose kernel for $^{90}$Y. This work also investigated the effects of resin microsphere material and the effects of liver as a surrounding material. Results from the two transport codes were compared.

### 6.1.1 $^{90}$Y microsphere characteristics

The two commercially available $^{90}$Y microsphere products, TheraSphere® and SIR-Spheres®, are described in Section 2.2. Recall that for TheraSphere, $^{90}$Y is a component of the glass matrix and is present throughout the volume of the sphere. For SIR-Spheres, $^{90}$Y is affixed to the resin microspheres via an ion exchange process and is present only on the surface of the sphere. Due to these differences in manufacturing methods, glass microspheres have a

higher approximate initial $^{90}$Y activity per microsphere of 2500 Bq versus 50 Bq for resin microspheres [Dezarn et al., 2011]. Thus, for the same injected activity, more microspheres would be infused with SIR-Spheres compared to TheraSphere. The stated diameter and density of the commercially available microspheres vary between publications. Tables 6.1 and 6.2 list some of the published diameters and densities, respectively, for both glass and resin microspheres.

Table 6.1: List of some published diameters for commercially available microspheres.

| | Type of microsphere | Diameter ($\mu$m) |
|---|---|---|
| TheraSphere package insert | Glass | $20 - 30$ |
| Dezarn [2008] | Glass | $25 \pm 10$ |
| Sarfaraz et al. [2004] | Glass | $25 \pm 10$ |
| Kennedy et al. [2004] | Glass | $25 \pm 10$ |
| SIR-Spheres package insert | Resin | $20 - 60$ |
| Dezarn [2008] | Resin | $32 \pm 10$ |
| Mo et al. [2005] | Resin | 35 |
| Kennedy et al. [2004] | Resin | $32 \pm 10$ |

Table 6.2: List of some published densities for commercially available microspheres.

| | Type of microsphere | Density (g·cm$^{-3}$) |
|---|---|---|
| Guimaraes et al. [2010] | Glass | 3.2 |
| Welsh et al. [2006] | Glass | 3.2 |
| Kennedy et al. [2007] | Glass | 3.6 |
| Day and Ehrhardt [1994] | Glass | 3.29 |
| Kennedy et al. [2010] | Resin | 2.12 |
| Welsh [2006] | Resin | 1.6 |
| Kennedy et al. [2007] | Resin | 1.6 |
| Mo et al. [2005] | Resin | 1.0 |

## 6.2 Methods and materials

### 6.2.1 Monte Carlo transport codes

Monte Carlo transport codes handle electron transport in a variety of ways, but for macroscopic simulations they all typically employ the condensed history technique developed by

Berger [1963]. This technique is needed due to the large number of interactions a single electron will undergo in the process of slowing down. The condensed history technique groups a number of collisional interactions into a single electron step. The cumulative effect of all of the interactions within the step are accounted for by sampling the energy loss and direction changes from the appropriate multiple scattering distributions [Kawrakow, 2000a]. Berger defined two classes of the condensed history techniques [1963]. The class I technique uses a precomputed energy grid for all cross sections, which results in the need for interpolations when particles do not conform to the grid energies. Additionally, primary and secondary particles are not correlated. The class II technique explicitly transports secondary particles that are above a threshold energy. The two transport codes used in this research were EGSnrc (version 4) [Kawrakow et al., 2010] and MCNP5 (version 1.51) [X-5 Monte Carlo Team, 2005]. Some of the specific aspects of each of these codes are described in the subsequent sections.

#### 6.2.1.1 EGSnrc

EGSnrc uses a class II technique for the treatment of electron collisional energy loss [Kawrakow et al., 2010]. EGSnrc has been shown to have accurate electron transport [Kawrakow, 2000a,b]. This is due to the use of the PRESTA II algorithm and the code's ability to actively change the step size of the electron transport, going to single interaction tracking when the electron is near a boundary. These features in EGSnrc allowed the default electron transport settings to be used in this work (ESTEPE = 0.25, XIMAX = 0.5, EXACT boundary crossing algorithm, skin depth for BCA = 3, and spin effects on) [Kawrakow and Rogers, 2006].

For EGSnrc simulations, the EDKnrc user code was used [Mainegra-Hing et al., 2005]. EDKnrc was developed for the calculation of energy deposition kernels for monoenergetic photons and dose kernels for electron sources and has been shown to agree with previous

studies using EGS4/PRESTA I [Simpkin and Mackie, 1990]. The native settings for EDKnrc only allow for theoretical point sources. The user code was updated to allow uniformly distributed spherical-type sources for the simulation of microspheres. These updates to the user code are given in Appendix B.2. The output of a simulation provides the dose delivered to a spherical shell of a specified medium.

#### 6.2.1.2 MCNP5

MCNP5 uses a class I technique for the treatment of electron collisional energy loss and by default has an average energy loss per step of 8.3 % [X-5 Monte Carlo Team, 2005], which cannot be changed by the user without altering the source code and recompiling [Reynaert et al., 2002]. The logic for sampling the energy straggling can be selected by the user in the 18th entry of the debug information card (DBCN). The default setting (DBCN 17J 0), also referred to as the bin-centered option, has been compared to the ITS energy indexing algorithm (DBCN 17J 1) by a number of authors [Reynaert et al., 2002, Jeraj et al., 1999, Schaart et al., 2002]. All found the ITS algorithm to be more accurate than the bin-centered option. However, for simulations with small geometric regions (even with the ITS algorithm), it is possible to have situations where non-physical results can be obtained [Reynaert et al., 2002]. A third option for sampling the energy straggling was made available with the release of version 1.40 of MCNP5. The new energy- and step-specific method (DBCN 17J 2) allows the energy loss for each electron transport step to be sampled separately from adjacent steps and uses the specific energy and step length of that step [X-5 Monte Carlo Team, 2005]. This method largely eliminates the linear interpolations and energy misalignments of the other algorithms. Hughes [2005] showed that adjacent geometric regions with thicknesses down to 100 $\mu$m do not affect the calculated electron energy spectrum.

With MCNP5, the user also has the ability to change the number of substeps per energy step for a specific material using the ESTEP card. The default value depends on the average atomic number of the material and ranges from 2 to 15. For example, the default value for water is 3. For geometries with small regions, increasing ESTEP can accommodate an accurate simulation of the electron's trajectory as the angular distribution is sampled at these substeps [X-5 Monte Carlo Team, 2005]. However, as Schaart et al. [2002] showed, increasing ESTEP has no effect on errors in the calculation of energy loss due to interrupted energy steps. For all MCNP5 simulations, the *F8 tally was used to score the energy deposited by both photons and electrons in spherical shells. The mass of the shell was then used to calculate the dose delivered to the shell.

### 6.2.2 Point source simulations

Simulations were completed with the source centered in a sphere of water (or liver, as described below) with a 20 cm radius. Scoring regions were spherical shells with thicknesses of 10 $\mu$m or 100 $\mu$m centered at radial distances matching those presented in ICRU 72 [2004] for comparison.

#### 6.2.2.1 Optimization of electron transport for MCNP5

Due to the number of user-selectable parameters available for electron simulations with MCNP5, the optimal settings were first determined using point source simulations. To extend the work of Hughes [2005] and investigate the influence of cell thickness, point source simulations were completed with scoring region thicknesses of 100 $\mu$m and 10 $\mu$m in water ($\rho = 1.0\,\mathrm{g{\cdot}cm^{-3}}$) using the default (DBCN 17J 0), the ITS-style (DBCN 17J 1), and the energy- and step-specific (DBCN 17J 2) methods. The use of the different straggling methods with MCNP5 will be referred to as $\mathrm{MCNP_{Def}}$, $\mathrm{MCNP_{ITS}}$, and $\mathrm{MCNP_{Specific}}$, respectively. To investigate the effect of changing the number of substeps per major step,

simulations were also completed with $\text{MCNP}_{\text{Specific}}$ using ESTEP set to 7, 10, 15, and 100 in addition to the default value of 3. Based on the results of these simulations, which are presented in Section 6.3.1, all subsequent microsphere simulations with MCNP5 used $\text{MCNP}_{\text{Specific}}$ with ESTEP set to 10.

#### 6.2.2.2 Dose rate simulations

For all simulations, the $^{90}$Y beta spectrum from ICRU 72 [2004] was used, which is the same spectrum used by Guimaraes et al. [2010]. All tally regions were 10 $\mu$m thick spherical shells (besides the 100 $\mu$m thick regions previously noted). Point source simulations were completed with EDKnrc and MCNP5 in water ($\rho = 1.0\,\text{g}\cdot\text{cm}^{-3}$) and liver. The elemental composition and density of liver ($\rho = 1.06\,\text{g}\cdot\text{cm}^{-3}$) from ICRU Report 44 (ICRU 44) [1989] were used. In order to isolate the differences in the simulation results due only to the differences in chemical composition between water and liver, simulations were also completed in water with a density of $1.06\,\text{g}\cdot\text{cm}^{-3}$ (i.e., the same density as ICRU 44 liver). All sources were assumed to have an activity of 1 Bq and sufficient particles were transported in every simulation to achieve statistical uncertainties of less than 1 %. The results of these point source simulations were compared to ICRU 72 reference data.

### 6.2.3 Microsphere simulations

For microspheres, simulations were again completed with the source centered in a sphere of water or liver with a 20 cm radius. And again, scoring regions were spherical shells with thicknesses of 10 $\mu$m centered at radial distances matching those presented in ICRU 72 [2004], except for radii that were within the microsphere.

For glass microspheres, the composition $17(Y_2O_3)-19(Al_2O_3)-64(SiO_2)$ was used [Erbe and Day, 1993]. The resin composition of SIR-Spheres is proprietary information, but the microspheres are likely composed of a cation exchange resin [e.g., Aminex 50W-X4 (Biorad,

Hercules, CA)] [Gray, U. S. Patent Application Publication No. US 2010/0215571 A1 (26 August 2010)]. Most cation exchange resins are composed of crosslinked polystyrene with sulfonic acid groups [Guo et al., 2009]. For this work, the composition of polystyrene from the National Institute of Standards and Technology (NIST) website [Berger et al., 2005] was used as an approximation. Simulations were completed for both average and maximum diameters and densities for both glass and resin microspheres based on the values given in Tables 6.1 and 6.2. For glass microspheres, the average values of 25 $\mu$m and 3.29 g·cm$^{-3}$ and the maximum values of 35 $\mu$m and 3.6 g·cm$^{-3}$ were used. For resin microspheres, the average values of 32 $\mu$m and 1.6 g·cm$^{-3}$ and the maximum values of 60 $\mu$m and 2.12 g·cm$^{-3}$ were used. The source distributions were chosen to match the different manufacturing methods. For glass microspheres, source particles were started uniformly throughout the volume of the sphere. For resin microspheres, the source particles were started uniformly on the surface of the sphere.

Simulations of both resin and glass microspheres were completed with both transport codes in water and in liver. Each simulation only used a single microsphere, neglecting any intersource effects on the calculated dose distribution. Sufficient particles were transported to achieve statistical uncertainties of less than 1 % in all microsphere simulations. The results of the microsphere simulations were compared to the point source results completed in the same medium (water or liver) and with the same transport code.

## 6.3 Results

### 6.3.1 Point source simulations

#### 6.3.1.1 Optimization of electron transport for MCNP5

The use of MCNP$_{\text{Specific}}$ appeared to reduce the number of non-physical artifacts that were observed with the other two electron transport options in MCNP5. This is demon-

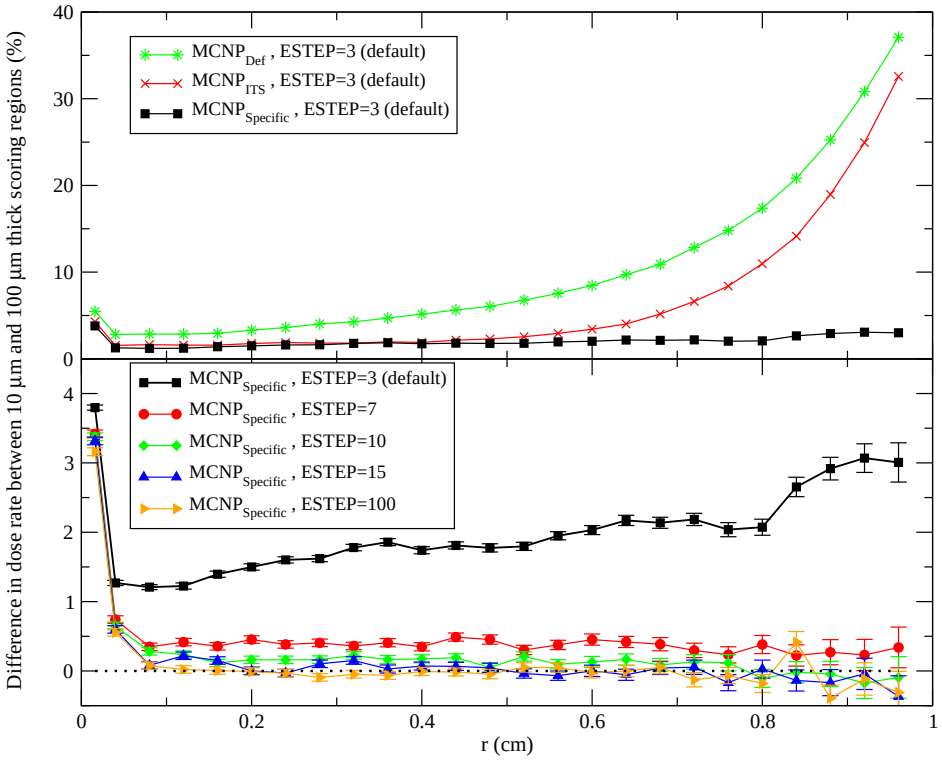


Figure 6.1: Percent difference in dose rate between point source simulations with 10 $\mu$m and 100 $\mu$m thick scoring regions versus distance from the source for: the three transport modes in MCNP5 (top) (error bars are not displayed as they were contained within the symbols) and using $\text{MCNP}_{\text{Specific}}$ with varying values of ESTEP (bottom).

strated in the top portion of Figure 6.1 as $\text{MCNP}_{\text{Specific}}$ showed less difference between the simulations with 10 $\mu$m and 100 $\mu$m thick scoring regions. However, there still was an offset between the simulations with the different scoring region thicknesses. This was resolved by increasing the ESTEP value, as shown in the bottom portion of Figure 6.1. A slight offset was observed in the dose rate between the two scoring regions for simulations with ESTEP set to 7. The simulations using the larger values of ESTEP (10, 15, and 100) all showed little difference between the different sized scoring regions. Based on these results, an ESTEP value of 10 was chosen for the subsequent simulations as it was the lowest value of ESTEP that demonstrated geometric independence. Using a lower value of ESTEP reduced the

required computation time of the simulations. The computing time approximately scaled linearly with the ESTEP value. For example, a simulation with ESTEP set to 10 would take approximately twice as long to complete as a simulation with ESTEP set to 5. Note in Figure 6.1 that the difference between the 10 $\mu$m and 100 $\mu$m thick scoring regions at the first investigated radial distance was approximately 3 to 5 % for all data series. This was due to volume averaging occurring in the simulations with the 100 $\mu$m thick scoring regions due to the sharp fall off of dose across the thickness of the scoring region. Note that the effect is resolved by the third investigated radial distance.

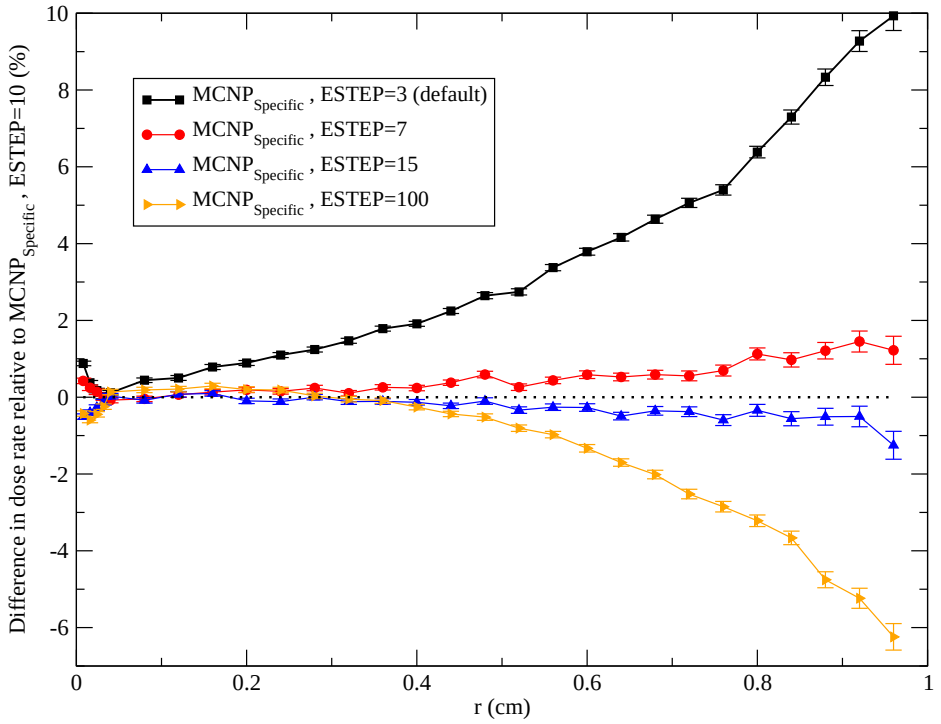


Figure 6.2: Percent difference in dose rate between point source simulations using MCNP$_{\text{Specific}}$ with ESTEP = 10 and other ESTEP values versus distance from the source.

Figure 6.2 shows the differences between the simulations with 10 $\mu$m thick scoring for the different values of ESTEP relative to ESTEP=10. As the value of ESTEP was increased,

the dose rate decreased. The reason for this decrease is unclear, but may be due to the increased values of ESTEP affecting the simulated scattering of the electrons, particularly in the larger non-scoring regions of the simulation geometry [Schaart et al., 2002]. A more exhaustive study of the abilities and limitations of $MCNP_{Specific}$ and ESTEP may help to guide future users to the most appropriate settings for their specific geometry.

#### 6.3.1.2 Dose rate simulations

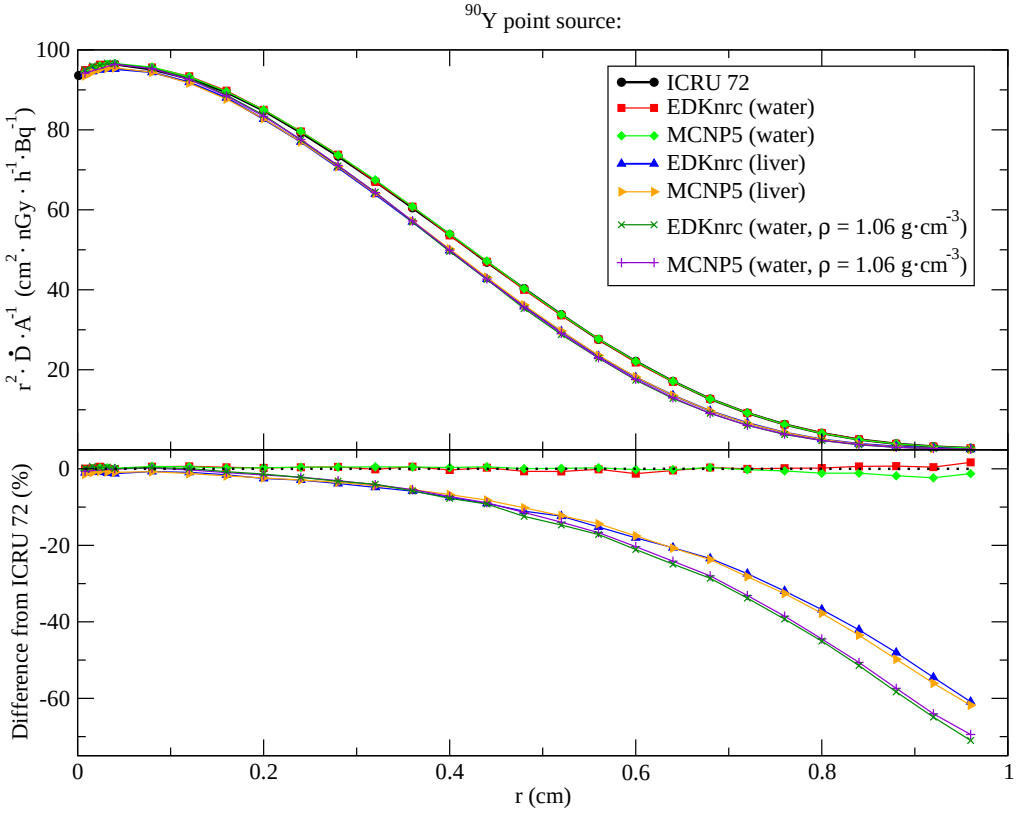


Figure 6.3: Radial dose-rates around a $^{90}Y$ point source (top) and percent differences from ICRU 72 reference data (bottom) for simulations with EDKnrc and MCNP5 (with $MCNP_{Specific}$ and ESTEP = 10) in water and liver. Error bars are not displayed as they were contained within the symbols.

Figure 6.3 presents the results of the point source simulations with both transport codes. The top portion of the plot shows the radial dose rate as a function of distance from

the source. It can be seen that simulations with EDKnrc and MCNP5 in water ($\rho$ = 1.0 g·cm$^{-3}$) agreed with each other and with ICRU 72 data. This is further demonstrated in the bottom portion of Figure 6.3, which presents the percent difference between the point source simulation results and the ICRU 72 data. The results of both transport codes in water were within 2 % of the ICRU 72 values over the range of the data. The radial distance in which 90 % of the emitted energy is absorbed, $X_{90}$, was calculated as 5.40 mm in this work for water ($\rho$ = 1.0 g·cm$^{-3}$), which was in good agreement with the value of 5.43 mm calculated by Mainegra-Hing et al. [2005]. Within $X_{90}$, the differences from ICRU 72 data were less than 0.7 % for both transport codes.

There was also good agreement between simulations in liver completed with EDKnrc and MCNP5. However, there was a large difference between the simulations in liver and in water. Both the EDKnrc and MCNP5 results in liver were more than 60 % less than the ICRU 72 values near the maximum range of $^{90}$Y and more than 12 % less than ICRU 72 within $X_{90}$. $X_{90}$ was calculated as 5.16 mm for liver and 5.10 mm for water ($\rho$ = 1.06 g·cm$^{-3}$). The results of the simulations in water with a density of 1.06 g·cm$^{-3}$ showed that the differences between water ($\rho$ = 1.0 g·cm$^{-3}$) and liver are largely due to the difference in density between the materials, and not the differences in chemical composition. Within $X_{90}$, the difference between water ($\rho$ = 1.06 g·cm$^{-3}$) and liver was less than 1.6 %. Sarfaraz et al. [2004] mentioned that they did not take the density of the patient's liver into account in their calculation of the dose distribution, but accounting for the patient's liver density would increase the accuracy of the calculated distribution.

### 6.3.2 Microsphere simulations

Figure 6.4 presents the results of the glass microsphere simulations in water for both transport codes and the results of Guimaraes et al. [2010] for comparison. The top portion of Figure 6.4 shows the radial dose rate as a function of distance from the center of the

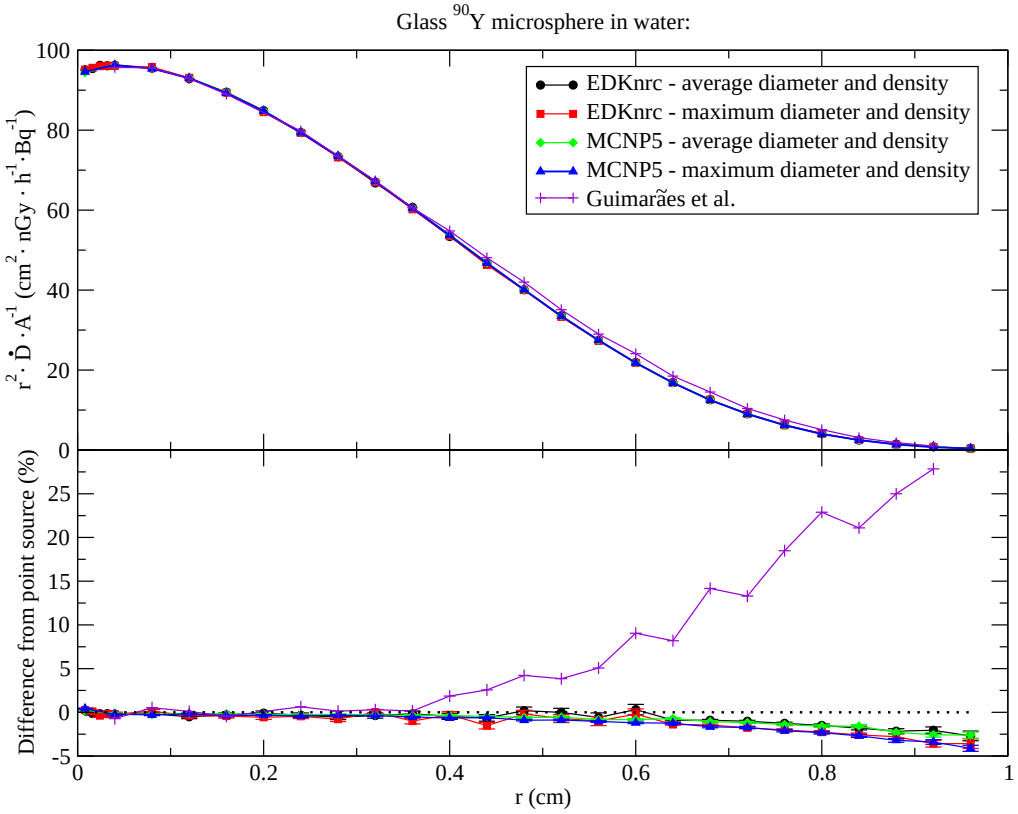


Figure 6.4: Radial dose-rate distributions around a $^{90}$Y glass microsphere in water (top) (error bars are not displayed as they were contained within the symbols) and percent differences from point source simulations (bottom) from the respective transport codes. For Guimaraes et al. [2010], the percent difference presented is relative to ICRU 72 data.

microsphere, and the bottom portion shows the percent difference from the point source simulations in water using the same transport code. For Guimaraes et al., the percent difference shown is relative to ICRU 72 reference data. It is seen that the maximum difference was more than 25 %. The results with both EDKnrc and MCNP5 showed there was little relative difference between the radial dose-rate distributions of the glass microspheres and a point source. The glass microsphere simulations were within 4.2 % of the point source simulations over the presented range and within 1.0 % inside of $X_{90}$ for the simulations with the maximum microsphere diameter and density. For the average microsphere diameter and density, the microsphere simulations were within 2.8 % and 0.9 % of the point source

simulations over the presented range and inside of $X_{90}$, respectively. As expected, the relative decrease for the simulations with the maximum diameter and density was greater at distances near the maximum range of $^{90}$Y compared to the decrease for simulations with the average values. Both transport codes showed this, and there was good agreement between the codes in the magnitude of these differences.

Guimaraes et al.'s [2010] radial dose-rate distributions were calculated from the average of 20, 40, and 60 $\mu$m diameter glass microsphere ($\rho = 3.2\,\mathrm{g{\cdot}cm^{-3}}$) simulations with the Geant4 Low Energy physics model [S. Agostinelli et al., 2003] and resulted in a maximum difference from ICRU 72 reference data of more than 25 %. As noted in Section 6.1, they presented their point source simulation results as being more than 50 % lower than ICRU 72 reference data near the maximum range of $^{90}$Y, but this is likely an error in the sign of the difference. Guimaraes et al. noted that the Low Energy physics model uses different stopping power data than ICRU 72 and showed that the CSDA range for a 2.28 MeV electron (the $^{90}$Y end point energy) in water is greater for the Low Energy physics model than for the ICRU 72 data (1.150 cm versus 1.129 cm, respectively). With the larger CSDA range, one would expect the point source simulation results to be higher than the ICRU 72 data near the maximum range of $^{90}$Y.

Guimaraes et al. [2010] also presented point source simulation results for the Standard and Penelope physics models in Geant4. These models showed much better agreement with the ICRU 72 reference data. Guimaraes et al. gave their reasoning for choosing the Low Energy physics model over the other models by simply stating it is the model recommended for medical physics applications, but they provided no citation for this claim.

Guimaraes et al. [2010] did not present a comparison of their microsphere simulation and point source simulation results. However, assuming they made an error in the sign of the difference for their point source simulation data relative to ICRU 72 data, their results would show a reduction in the radial dose rate for microsphere simulation results relative

to point source simulation results, as would be expected. The magnitude of this difference between the microsphere simulations and point source simulation results would likely be larger than those determined in this work as they simulated glass microspheres with larger diameters.

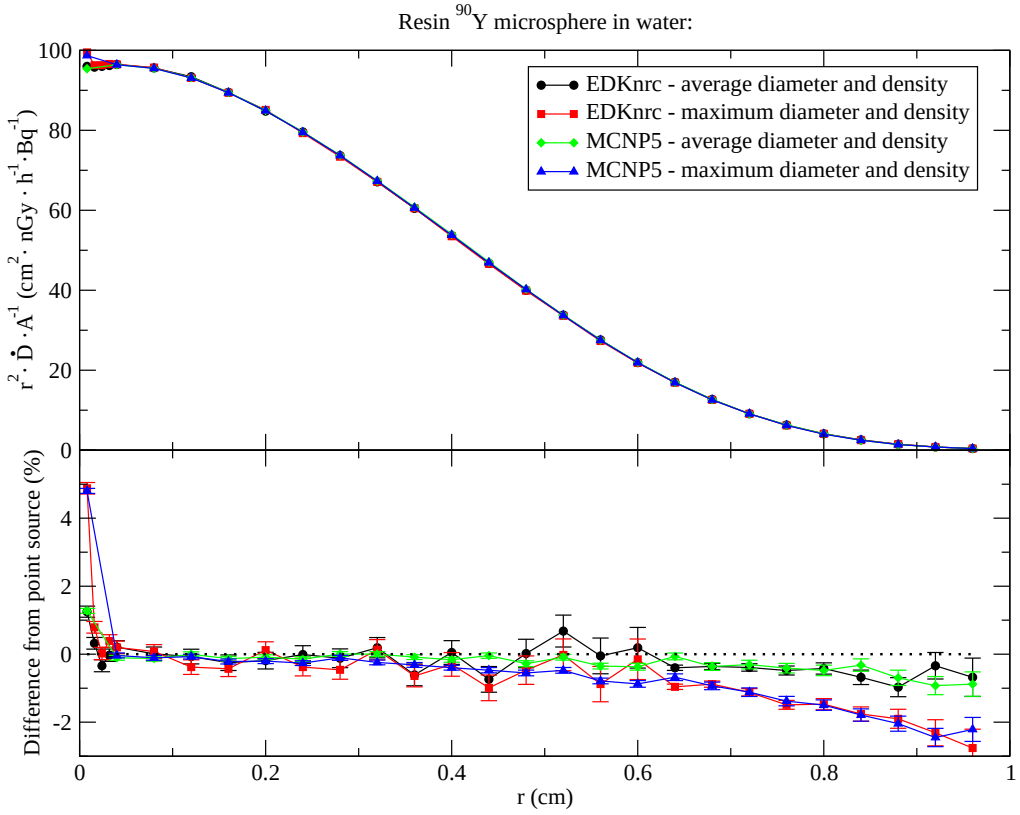


Figure 6.5: Radial dose-rate distributions around a $^{90}$Y resin microsphere in water (top) (error bars are not displayed as they were contained within the symbols) and percent differences from point source simulations (bottom) from the respective transport codes.

Figure 6.5 shows the results of the resin microsphere simulations in water. Like the glass microsphere simulations in water, there was little difference between the resin microsphere results and the point source results. The polystyrene material affected the dose kernel less than the glass material relative to a point source, as the resin microsphere simulations were within 2.8 % of the point source simulations over the presented range and within 1.0 % inside of $X_{90}$ for the simulations with the maximum diameter and density. For the average

microsphere diameter and density, the microsphere simulations were within 1.0 % and 0.8 % of the points source simulations over the presented range and inside of $X_{90}$, respectively. These differences did not include the first radial distance investigated, which had a higher value due to the close proximity of this scoring region to the source distributed on the resin microsphere surface. Again, the difference from the point source simulations was greater for simulations with the maximum diameter and density than for those with average values, and there was good agreement between MCNP5 and EDKnrc in the magnitude of these differences.

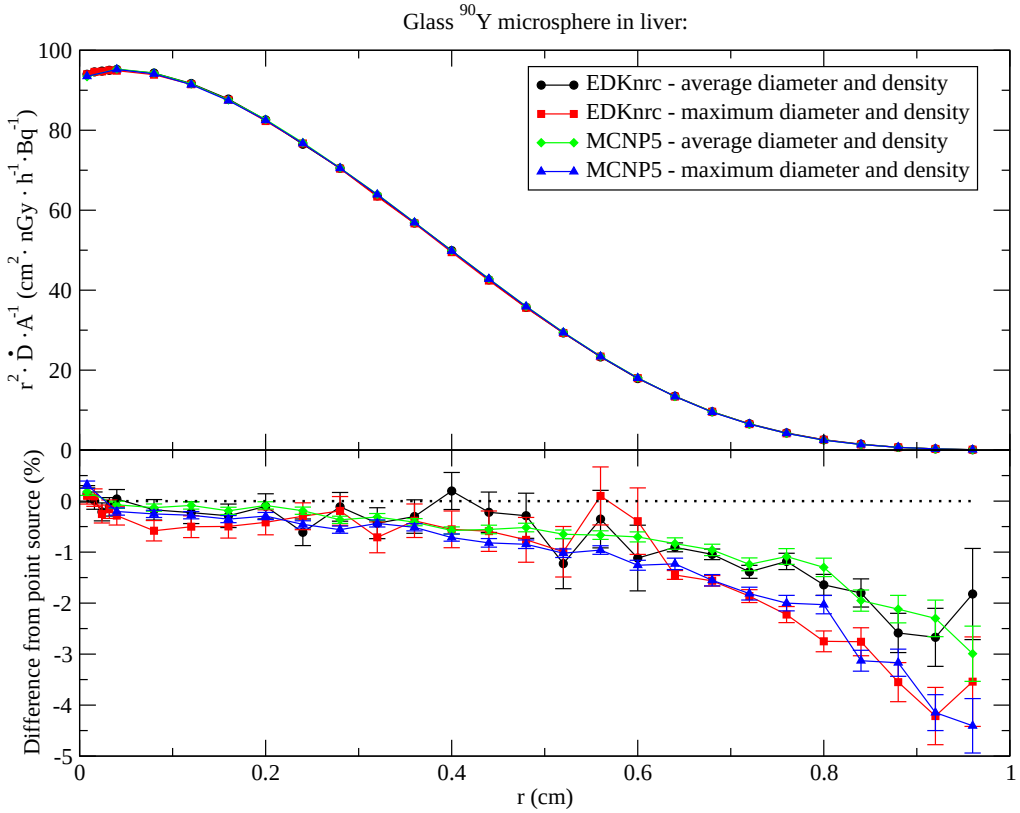


Figure 6.6: Radial dose-rate distributions around a $^{90}$Y glass microsphere in liver (top) (error bars are not displayed as they were contained within the symbols) and percent differences from point source simulations (bottom) from the respective transport codes.

Figures 6.6 and 6.7 show the results of simulations in liver for the glass and resin microspheres, respectively. Comparing the bottom portions of Figures 6.6 and 6.7 to the bottom

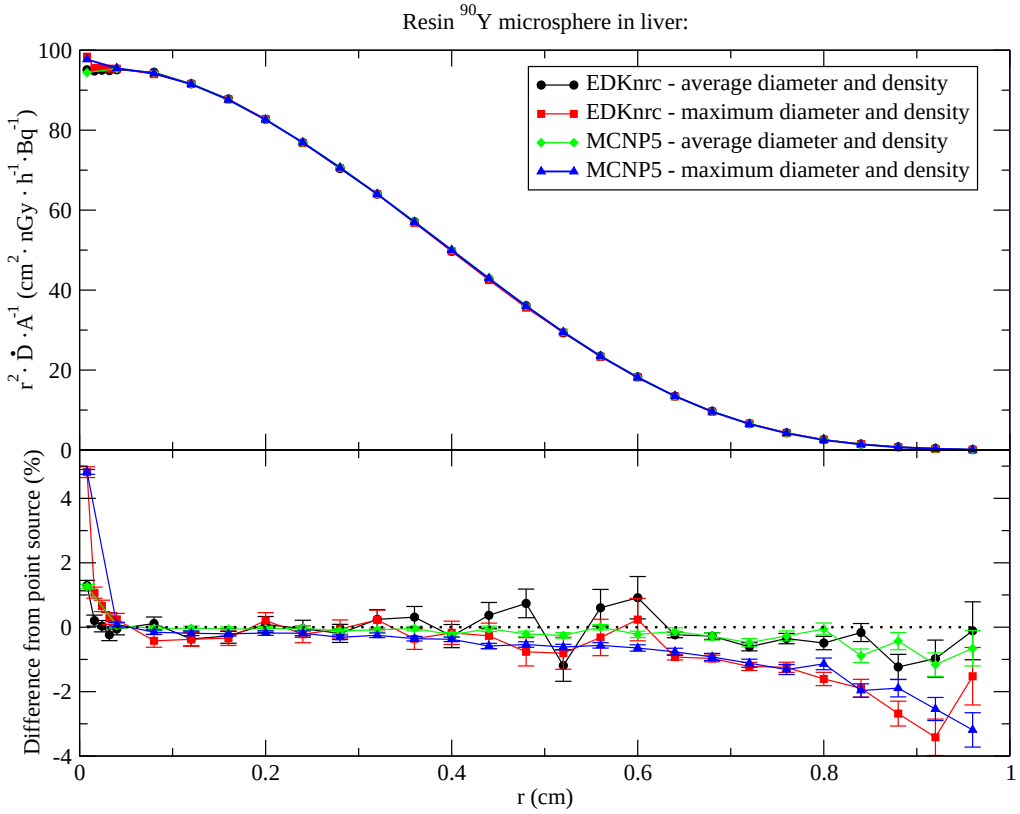


Figure 6.7: Radial dose-rate distributions around a $^{90}$Y resin microsphere in liver (top) (error bars are not displayed as they were contained within the symbols) and percent differences from point source simulations (bottom) from the respective transport codes.

portions of Figures 6.4 and 6.5, respectively, it can be seen that the magnitude of the difference from the point source results (i.e., the effect of the microsphere material) was similar for each of the microsphere types between the two surrounding materials (i.e., water and liver). The glass material again had a greater effect on the dose kernel than the polystyrene. Likewise, the simulations with the maximum values for the diameter and density of both microspheres showed greater differences from the point source results than simulations with the average values. There was good agreement in the magnitude of the difference from the point source simulations between the codes for the simulations in liver. However, as presented in Figure 6.3, the dose kernels calculated in liver were different from those in water. Also, the ICRU 44 definition of liver does not take into account individual variation or the

potential difference of diseased liver versus healthy liver. As suggested in Section 6.3.1, for the most accurate results, the density of an individual patient's liver should be considered.

## 6.4 Conclusions

Like Hughes [2005], this work showed that the new transport algorithm, $\text{MCNP}_{\text{Specific}}$, demonstrates improvement over the two previous electron transport algorithms available in MCNP5. For this work, using $\text{MCNP}_{\text{Specific}}$ and an ESTEP value of 10 were determined to be the optimal settings. These settings seemed to provide accurate results for this work based on their independence of the simulation geometry and their subsequent agreement with the results of EGSnrc user code EDKnrc. However, it was also found that the results trended with the ESTEP value. Thus, electron transport in MCNP5 should still be used with caution, and users should confirm they are using the optimal settings for their specific simulation geometry. A comprehensive evaluation of $\text{MCNP}_{\text{Specific}}$ and the other electron transport parameters in MCNP5 that could provide best practice settings for a particular geometry would be useful for future users.

The point source simulations in water completed with EDKnrc and MCNP5 both agree well with ICRU 72 reference data. There was also good agreement between the codes for point source simulations in liver (as defined by ICRU 44). However, the simulations in liver varied from the results in water by more than 60 % near the maximum range of $^{90}$Y. It was shown that these differences were largely due to the difference in density between liver and water ($1.06\,\text{g}\cdot\text{cm}^{-3}$ and $1.0\,\text{g}\cdot\text{cm}^{-3}$, respectively). For the most accurate calculation of the dose distribution, the density of the patient's liver should be taken into account.

The simulations used to calculate the $^{90}$Y dose kernel were not greatly affected by the presence of either the glass or resin microsphere material. Glass microspheres caused a larger decrease in the dose rate near the maximum range of $^{90}$Y compared to resin microspheres.

However, both glass and resin microsphere simulation results were within 1 % of the point source simulation results inside of $X_{90}$.

Further work could use various activity distributions to quantify the potential difference in the dose distributions calculated using dose kernels with different surrounding materials and densities or with microsphere materials present. This could provide an estimate of the uncertainty introduced in dose distribution calculations due to certain assumptions (such as substituting water for liver). Additional future work could investigate the effects of microsphere clustering and the resulting intersource attenuation. A number of authors have investigated the distribution and clustering patterns of microspheres in the liver following their infusion [Pillai et al., 1991, Fox et al., 1991, Campbell et al., 2000, Kennedy et al., 2004]. Campbell et al. [2000] found that cluster populations are skewed toward low numbers and determined a median cluster population of five microspheres in their work. However, due to the higher density of microspheres (particularly the glass spheres), this clustering may affect the dose distribution.

# Chapter 7

# Conclusions and future work

## 7.1 Conclusions

Treatment of liver malignancies with $^{90}$Y microspheres is largely considered palliative and typically only performed after other treatment options have been exhausted. However, results have shown that treatments with $^{90}$Y microspheres have the potential to downgrade the disease state to resectable, which is a curative state. The large uncertainties associated with this treatment hinder the ability to correlate outcome with the dose delivered, which has resulted in this treatment being largely unoptimized. This thesis work sought to reduce the uncertainties associated with the dosimetry of the $^{90}$Y microsphere treatment.

### 7.1.1 $^{90}$Y activity assay with the coincidence detection system

A coincidence detection system (CDS) was developed to assay the activity of a $^{90}$Y microsphere sample. A counting-losses correction method that utilized a series of pulse generators was implemented into the CDS and validated. The validation process concluded that the pulser method was accurate for counting losses less than 15 %. A geometric characterization of the response of the CDS was completed. The results provided the ability to select a source measurement position that was independent of the source size.

The accuracy of the CDS was validated by comparing the CDS-determined activity of a $^{90}$Y standard solution to the known activity. The difference between the CDS-determined activity and the known activity was 2.6 %, which was within the combined expanded uncertainty of the CDS-determined result of 4.50 %

The CDS was used to assay the activity of a SIR-Spheres sample in both a glass shipping vial and a polycarbonate v-vial. The determined activities were 3.72 GBq $\pm$ 1.84 % and 3.46 GBq $\pm$ 1.96 %, respectively. The decreased activity for the v-vial assay was expected since not all of the microspheres were transferred from the shipping vial to the v-vial. The manufacturer-stated activity for the shipping vial was 3 GBq $\pm$ 10 %. The CDS-determined activity was 24 % higher than the manufacturer-stated value. This is outside of the manufacturer's stated uncertainty and in agreement with results from Selwyn et al. [2008], who assayed the activity of a SIR-Spheres sample and determined a value 26 % higher than the manufacturer's stated activity. These results suggested that the manufacturer's methods for determining the SIR-Spheres activity are inaccurate.

The activity determined with the CDS could be used to calibrate well-type ionization chambers for the clinical determination of $^{90}$Y microsphere activity. However, the higher activity determined with the CDS than the activity given by the Sirtex Medical would need to be accounted for in the prescription activity of SIR-Spheres.

### 7.1.2 Well-type ionization chamber characterization

Both a Standard Imaging IVB 1000 well chamber and a Capintec 12 atm dose calibrator were characterized for their use as a clinical measurement device to determine that activity of a SIR-Spheres sample. Calibration coefficients were calculated from measurements of a $^{90}YCl_3$ standard activity solution at volumes ranging from 1 mL to 5 mL in a glass shipping vial and a polycarbonate v-vial for both chambers. The IVB 1000 well chamber was found to exhibit large volume dependencies in the $^{90}YCl_3$ solution measurements. An evaluation based on

the activity preparation methods used with SIR-Sphere was completed to determine how the volume dependencies affected the activity delivered to the patient. Due to the volume dependencies with the IVB 1000 well chamber, the actual activity could deviate from the prescription activity by as much as 45 %. With the 12 atm dose calibrator, the largest difference between the prescription and actual activity was more than 10 %. However, with the v-vial the largest difference was 1.2 %. Because of these results, it was concluded that the IVB 1000 well chamber would not be an ideal measurement device for the clinical determination of SIR-Spheres activity. Further Monte Carlo studies were completed with the Capintec 12 atm dose calibrator to investigate the effects of the microsphere material on the response of the chamber.

A MCNP5 model of the 12 atm dose calibrator was completed. The model was validated by comparing the relative response of the dose calibrator determined from simulations of the $^{90}YCl_3$ solution with measured values. Simulations were then completed with various assumed microsphere material definitions to investigate variations due to microsphere composition. Simulations were completed to analyze the effects of volume, vial wall thickness, and source position. Again, the effects of the volume dependencies on the actual activity delivered were analyzed. It was found that simulations with the v-vial had the least variation in the delivered activity due to volume and vial wall thickness effects. Because of these results, it was concluded that the v-vial would be the more optimal measurement vial over the presently used shipping vial in the Capintec 12 atm dose calibrator.

### 7.1.3 Microsphere-specific dose kernels

Dose distributions can be calculated by convolving radionuclide-specific dose kernels with activity distributions. The effects of both resin and glass microsphere material on the $^{90}Y$ dose kernel were evaluated by comparing Monte Carlo microsphere simulation results with $^{90}Y$ point source simulation results. These simulations were completed in both water and

liver as the surrounding material. The maximum variation of the microsphere simulation results from the point source simulations results occurred near the maximum range of $^{90}$Y in water ($\sim$ 11 mm). The largest differences were 4.2 % and 2.8 % for the glass and resin microspheres, respectively. Within the the radial distance in which 90 % of the emitted energy is absorbed, $X_{90}$, these differences were less than 1 %.

The simulations in liver resulted in similar differences between the microsphere and point source simulations. However, point source simulation results in liver were as much as 60 % less than point source simulation results in water near the maximum range of $^{90}$Y, and 12 % less within $X_{90}$. These differences were attributed to the difference in density between water and liver (1.0 g·cm$^{-3}$ versus 1.06 g·cm$^{-3}$, respectively). Accounting for the patient's liver density in the dose kernel determination would increase the accuracy of the calculated dose distribution.

Simulations were completed with MCNP5 and EGSnrc Monte Carlo transport codes. The accuracy of the transport codes was validated by comparing to reference data from the International Commission on Radiation Units and Measurements Report 72 [2004]. A new energy straggling algorithm in MCNP5 was evaluated. Electron transport parameters that were independent of the tally cell geometry and gave results that were in agreement with the reference data were determined for simulations with MCNP5. However, the MCNP5 simulation results were found to be dependent on the ESTEP parameter used for simulations. Because of these results it was recommended that electron transport with MCNP5 be used with caution.

## 7.2 Recommendations for future work

A number of future investigations could serve to continue to improve the $^{90}$Y microsphere treatment. Some suggestions for future work based on the findings of this work are listed below.

### 7.2.1 Improved counting-losses correction

An advantage of the CDS over a single HPGe detector is the speed in which an activity of a sample can be determined to a particular uncertainty level. This was demonstrated in Section 3.2.8. Additionally, Selwyn et al. [2008] used a single HPGe detector to determine the activity of a SIR-Spheres sample to an uncertainty of 1.8 % after 167 h of detection time. In comparison, this work determined the activity of SIR-Spheres sample to an uncertainty of 1.84 % after 68 h of detection time. The counting-losses correction of the CDS described in Chapter 3 was shown to be accurate for counting losses under 15 %; however, this 15 % counting loss cut-off limits the ability of the CDS to assay the activity of a clinical strength $^{90}$Y microsphere sample (i.e., a sample activity of approximately 3 GBq). Improving the counting-losses correction by increasing this cut-off level would enable the CDS the ability to determine the activity of a clinical strength source which could then be used for local studies. Alternatively (or in addition), the distance between the detectors in the CDS could be increased. This would reduce the 511 keV peak-of-interest count rate, but would also reduce the counting losses experienced by the CDS.

### 7.2.2 Determination of TheraSphere activity with the CDS

This thesis work focused on the SIR-Spheres product. The activity of a sample of SIR-Spheres was determined in both a shipping vial and a v-vial with the CDS (Chapter 4). These same methodologies could be extended to determine the activity of the TheraSphere product. These glass $^{90}$Y microspheres are provided by MDS Nordion in a shielded v-vial at a variety of activity levels. The attenuation corrections to the CDS measurements could be determined using the methods described in Section 4.5 to account for the difference in the attenuation between the TheraSphere shielded vial and the source used for the efficiency calibration of the CDS. Since TheraSphere is provided at multiple activity levels, the number of microspheres within the sample varies. The number of microspheres within

the sample would need to accounted for in the calculation of the attenuation correction. Additionally, a holder would need to be constructed that could accommodate the TheraSphere vial for measurements with the CDS. Establishing a common activity measurement standard between the two commercially available $^{90}$Y microsphere products would allow for meaningful, quantifiable comparisons of products.

### 7.2.3 Effects of glass microsphere material on well-type chamber response

TheraSphere do not use the same activity preparation methods as SIR-Spheres. Rather than preparing the desired activity, the TheraSphere product is ordered at a desired activity level based on the timing of the procedure. Because of this, the TheraSphere product is not subject to the effects on the actual activity delivered due to volume dependence of the well-type ionization chamber seen with the SIR-Spheres activity preparation methods. However, the glass microspheres being available at activity levels ranging from 3 GBq to 20 GBq means there is a proportional range in the number of microspheres contained within each sample. This difference in the number of microspheres contained in the TheraSphere vial could result in a well-type ionization chamber responding non-linearly with increase activity due to a greater self absorption with a higher number of microspheres. Future studies could investigate these potential effects. Useful information for completing these studies from MDS Nordion would include the size distribution of the microspheres, dimensional and material information of the vial, and the approximate number of microspheres contained in the vial for the various activity levels.

### 7.2.4 Implementing a well-type ionization chamber calibration service

To establish a calibration protocol using the CDS as a standard measurement device for determining the activity of $^{90}$Y microspheres, a hybrid of the radiation oncology and the nuclear medicine protocol would need to be implemented. This could involve a physicist

acquiring a microsphere sample from the manufacturer, making measurements in their dose calibrator, and then sending the sample to an ADCL. The activity of the sample could then be determined with the CDS or a reference well-type ionization chamber traceable to the CDS. The clinical physicist would have to ensure that the measurement geometry used in the initial measurement would continue to be used with future measurements. Implementing a calibration service for $^{90}$Y microspheres would require the cooperation of the manufacturers to provide sources for calibration.

### 7.2.5 Robust characterization of electron transport in MCNP5

MCNP5 has a user-friendly system of entering the simulation geometry and useful variation reduction techniques, but the electron transport with this Monte Carlo code can be inaccurate for some simulation geometries. This is particularly true for smaller geometries. As mentioned in Section 6.2.1.2, a new energy- and step-specific logic option was implemented into MCNP5 to attempt to resolve some of these issues. This work found that even with this new energy straggling option, results varied with the ESTEP transport parameter. Future work could complete a robust characterization of the MCNP5 electron transport that could provide users with best-practice methods would be useful. Future work utilizing MCNP5 could investigate the effects of the clustering of $^{90}$Y microspheres, and the resulting intersource absorption, to evaluate how this affects the resulting dose distributions.

### 7.2.6 Clinical studies

With the implementation of a well-type ionization chamber calibration service and a 3D image-based dosimetry, more accurate dosimetry can be achieved with the $^{90}$Y microsphere treatments. This will enable meaningful clinical studies investigating the outcomes and toxicities experienced by patients versus the dose distribution that was delivered. Based on these data, the radiobiological analyses could be completed to attempt to optimize the

treatment. Fractionation schemes could also be considered. Potentially a subset of patients could be identified for which $^{90}$Y microsphere treatments are particularly beneficial such that the treatment is able to consistently provide a downgrade in the disease state to resectable and become a step in the path to a curative result.

## 7.3 Closing remarks

The $^{90}$Y microsphere treatment has the potential to be improved. The work completed in this dissertation has shown the potential of the CDS to be a standard measurement device for the determination of $^{90}$Y microsphere activity, and has provided suggestions for more accurate measurement geometries in well-type ionization chambers. Implementing a calibration service based on these results would contribute toward the improvement of the $^{90}$Y microsphere treatment. The work completed in this thesis could be improved with information, such as material composition of the microspheres, that can only be provided by the manufacturer. Additional information from the manufacturer would provide the ability to complete more realistic Monte Carlo simulations investigating the attenuation correction for the spectra measurements completed for the CDS, simulations investigating the relative response of the Capintec 12 atm dose calibrator, and the simulations used the determine the dose rate of a single microsphere as a function of distance from the center of the microsphere.

This chapter has listed a number of other improvements that would also contribute toward improvements. Many of these future improvements would also be greatly aided by (if not be completely dependent on) the cooperation of the $^{90}$Y microsphere manufacturers. Obtaining this cooperation most likely would require strong recommendations by the American Association of Physicists in Medicine that these improvements be implemented or legal requirements implemented by government organizations, such as the Food and Drug Administration or the Nuclear Regulatory Commission.

# Appendix A

# NIM electronics settings

## A.1 NIM electronics settings used with the CDS

The various Nuclear Instrumentation Module (NIM) electronics settings used for the coincidence detection system (CDS) are provided in Table A.1. These settings are provided for reference only, and may not result in the correct operation of the CDS due to a number of factors, such as the use of different lengths of coaxial cables between the various modules. The methods described in Chapter 3 should be used for correctly configuring the various timing and energy pulses in order to reproduce the results presented in this dissertation.

Table A.1: Settings of the various NIM electronics used in the CDS.

| Module | Settings |
|---|---|
| Ortec model 113 preamplifier | 45 pF input capacity (0 + 45) |
| Canberra model 2101N preamplifier | No user-changeable settings |
| Ortec model 460 amplifier | Coarse gain: 200, Fine gain: 0.8, negative input, 0.1 $\mu$s integration time |
| Canberra model 2024 amplifier | Coarse gain: 300, Fine gain: 3.30, positive polarity, 1 $\mu$s shaping time |
| Ortec model 551 TSCA (NaI) | ULD: 3.36, LLD: 0.60, Delay: 4.08 (1-11 $\mu$s) |
| Ortec model 551 TSCA (HPGe) | ULD: 2.82, LLD: 0.46, Delay: 1.00 (0.1-1.1 $\mu$s) |
| Ortec model 425A delay | 60 ns delay in time |
| Ortec model 467 TPHC | Range: 0.8 $\mu$s (x1), ULD: 5.32, LLD:2.08 |
| Ortec model 416A gate and delay generator | Delay: 3.42 (11 $\mu$s), Amplitude: $\sim$6 V, Width: $\sim$4.5 $\mu$s |
| Ortec model 427A delay (x2) | 7 $\mu$s delay in time |
| BNC model DB-2 random pulse generator (trigger) | Random pulse output |
| BNC model BL-2 fast tail pulse generator (HPGe) | Amplitude: 5.95, Rise time: 3 ns, Fall time: 100 ns, Width: 500 ns, Delay: 100 ns |
| Ortec model 416A gate and delay generator | Delay: 5.14 (1.1 $\mu$s), Amplitude and width: as low as possible |
| BNC model DB-2 random pulse generator (NaI) | Amplitude: 1.75, Normalize: 2.32, Rise time: 0.1 $\mu$s, Fall time: 50 $\mu$s |
| Ortec model 974 quad counter | Set for maximum count time, controlled with computer program |

# Appendix B

# Programming code

## B.1 974 counter control program

```
Public Class FormControl
    Dim Interval As Integer
    Dim run As Integer


    Private Sub FormControl_Load(ByVal sender As System.Object, ByVal e As System.EventArgs) Handles MyBase.Load
        SerialPort1.Open() 'Establishes connection to 974 counter via serial port when form is loaded
    End Sub

    Private Sub ButtonStart_Click(ByVal sender As System.Object, ByVal e As System.EventArgs) Handles ButtonStart.Click
        Label1.Text = DateString + " " + TimeOfDay + Environment.NewLine + "Time(s)=" + TextBoxTime.Text
        Label1.Text = Label1.Text + " No. of intervals=" + TextBoxIntervals.Text + Environment.NewLine
        Interval = TextBoxIntervals.Text
        Timer1.Interval = TextBoxTime.Text * 1000 'Input the count time. Multiply by 1000 because computer timer is in milliseconds.
        run = 1
        SerialPort1.WriteLine("CLEAR_COUNTERS") 'Clears the counts on the 974
        SerialPort1.WriteLine("START") 'Starts counting
        Timer1.Start() 'Starts the computer timer
    End Sub

    Private Sub Timer1_Tick(ByVal sender As System.Object, ByVal e As System.EventArgs) Handles Timer1.Tick
        'When the timer ends...
        Timer1.Stop() ' Stop the computer timer
        SerialPort1.WriteLine("STOP") 'Stop the 974 counting
        SerialPort1.WriteLine("SHOW_COUNTS") 'Show the number of counts (requests this data to be put in data string)
        Threading.Thread.Sleep(1000) 'Pause for 1 second. This is the time Genie 2k pauses between measurements.
        ' This also allows the 974 counter time to reply after the "SHOW_COUNTS" request
        Label1.Text = Label1.Text + TimeOfDay + Environment.NewLine + SerialPort1.ReadExisting 'Write output to label
        ' SerialPort1.ReadExisting reads the data string present from the 974
        My.Computer.FileSystem.WriteAllText("C:\Documents and Settings\keith\Desktop\" + DateString + " 974counts.txt", Label1.Text, False)
        ' Creates a file and outputs the label to the file. The "False" setting means the file is re-written each time (i.e. it
        ' always matches the label and doesn't just add to the end of the file).
        If run < Interval Then
            'Restart everything if the desired number of intervals has not been reached
            SerialPort1.WriteLine("CLEAR_COUNTERS")
            SerialPort1.WriteLine("START")
            Timer1.Start()
            run = run + 1 'add one to the number of runs
        End If
    End Sub
End Class
```

Figure B.1: Visual Basic Express 2008 code for 974 counter controller program.

## B.2 Modifications to EGSnrc user code EDKnrc

Modifications were made to the edknrc.mortran file of the EGSnrc user code EDKnrc in order to accommodate simulations with spherical source distributions. The modifications to various lines in the edknrc.mortran file to accomplish this are shown in Figure B.2.

```
Lines 773-789

"select direction isotropically in 4 Pi"

REPLACE{$SELECT-4PI-DIRECTION} WITH {;
    $RANDOMSET COSTHE;   COSTHE=2.*COSTHE-1;
    SINTHE=SQRT(1.0-COSTHE**2);
    $RANDOMSET PHI;PHI=TWOPI*PHI;
    uin = SINTHE*COS(PHI); vin = SINTHE*SIN(PHI); win = COSTHE;
};

"select initial location within source sphere"
REPLACE{$SELECT-SOURCE-LOCATION} WITH {;
    $RANDOMSET COSTHE;   COSTHE=2.*COSTHE-1;
    SINTHE=SQRT(1.0-COSTHE**2);
    $RANDOMSET PHI;PHI=TWOPI*PHI;
    $RANDOMSET RAD; RAD=RAD**0.3333333; RAD=0.0015*RAD; "30um diam sphere"
    xin = RAD*SINTHE*COS(PHI); yin = RAD*SINTHE*SIN(PHI); zin = RAD*COSTHE;
};

Lines 1223-1224

$REAL     PHI;
$REAL     RAD;


Lines 1543-1551

   IF ( ISOURC = 1 )["select direction isotropically in 4 Pi"
      interact_now = .false.;"don't force original particle to interact"
      $SELECT-4PI-DIRECTION;
      $SELECT-SOURCE-LOCATION;
      irin = ibsearchrev(win,nc,cosalp)+1;"binary search"
      "OUTPUT irin, 180.0/PI*acos(win);('initial region : ',I5,' at ', f8.3);"
      "OUTPUT xin, yin, zin; (' ',1pe11.4,' , '1pe11.4,' , ',1pe11.4);"
      "OUTPUT xin;('xin : ',1pe11.4);"
      call shower(iqin, ei, xin, yin, zin, uin, vin, win, irin, wtin);

Lines 2335-2340

ELSEIF ( ISOURC = 1 )["isotropically radiating point source at origin"

 " /xin, yin, zin/ = 0.0; zin = 0.001; "
  irin = 2;
  wtin = 1.;
  OUTPUT;('isotropically radiating point source at origin what what'/);
```

Figure B.2: Lines in the file edknrc.mortran that were changed to enable spherical source distributions for simulations with EGSnrc user code EDKnrc.

# Bibliography

American Cancer Society. Cancer Facts & Figures 2012. Atlanta: American Cancer Society, 2012.

American Cancer Society. Liver cancer detailed guide. Atlanta: America Cancer Society, 2011.

Frank Herbert Attix. *Introduction to Radiological Physics and Radiation Dosimetry*. Wiley-VCH, Weinheim, Germany, 2004.

Miguel A. Avila-Rodriguez, Reed G. Selwyn, Joseph A. Hampel, Bruce R. Thomadsen, Onofre T. DeJesus, Alexander K. Converse, and Robert J. Nickles. Positron-emitting resin microspheres as surrogates of $^{90}$y sir-spheres: a radiolabeling and stability study. *Nucl. Med. Biol.*, 34:585–590, 2007.

M. J. Berger. *Methods in Computational Physics*, chapter Monte Carlo calculation of the penetration and diffusion of fast charged particles, pages 135–215. Academic, New York, 1963.

M. J. Berger, J. S. Coursey, M. A. Zucker, and J. Chang. ESTAR, PSTAR, and ASTAR: Computer Programs for Calculating Stopping-Power and Range Tables for Electrons, Protons, and Helium Ions (version 1.2.3). (online) Available: http://physics.nist.gov/Star [2008, July 9], National Institute of Standards and Technology, Gaithersburg, MD, 2005.

C. Breedis and G. Young. The blood supply of neoplasms in the liver. *Am. J. Pathol.*, 30: 969–985, 1954.

Andrew M. Campbell, Ian H. Bailey, and Mark A. Burton. Analysis of the distribution of intra-arterial microspheres in human liver following hepatic yttrium-90 microsphere therapy. *Phys. Med. Biol.*, 45:1023–1033, 2000.

Janice M. Campbell, C. Oliver Wong, Otto Muzik, Brian Marples, Michael Joiner, and Jay Burmeister. Early dose response to yttrium-90 microsphere treatment of metastatic liver cancer by a patient-specific method using single photon emission computed tomography and positron emission tomography. *Int. J. Radiat. Oncol. Biol. Phys.*, 74:313–320, 2009.

Canberra. *Genie$^{TM}$ 2000 Spectroscopy Software Customization Tools*. Canberra Industries, Inc., 2006.

S. R. Cherry, J. A. Sorenson, and M. E. Phelps. *Physics in Nuclear Medicine*. Saunders, Philadelphia, PA, third edition, 2003.

B.M. Coursey, W.B. Mann, A. Grau Molonda, E. Garcia-Torano, J.M. Los Arcos, J.A.B. Gibson, and D. Reher. Standardization of carbon-14 by $4\pi\beta$ liquid scintillation efficiency tracing with hydrogen-3. *Appl. Radiat. Isot.*, 37:403–408, 1986.

B.M. Coursey, J.M. Calhoun, and J.T. Cessna. Radioassays of yttrium-90 using in nuclear medicine. *Nucl. Med. Biol.*, 20:693–699, 1993.

Delbert E. Day and Gary J. Ehrhardt. Microspheres for radiation therapy, April U. S. Patent No. 5,302,369 (12 April 1994).

K. Debertin and R. G. Helmer. *Gamma- and X-ray spectrometry with semiconductor detectors*. Elsevier Science Pub. Co., Inc., New York, 1988.

L. DeWerd, S. Davis, L. Bartol, and F. Grenzow. Ionization chamber instrumentation, Proceedings of the AAPM Summer School, 2009a. 181-204.

L. A. DeWerd, S. D. Davis, L. J. Bartol, and F. Grenzow. *Clinical Dosimetry Measurements in Radiotherapy*, chapter Ionization chamber instrumentation, pages 181–204. Medical Physics Monograph No. 34, AAPM, 2009b.

Larry A. DeWerd, John A. Micka, Shannon M. Holmes, and Tim D. Bohm. Calibration of multiple ldr brachytherapy sources. *Med. Phys.*, 33:3804–3813, 2006.

W. A. Dezarn, J. T. Cessna, L. A. DeWerd, W. Feng, V. L. Gates, J. Halama, A. S. Kennedy, S. Nag, M. Sarfaraz, V. Sehgal, R. Selwyn, M. G. Stabin, B. R. Thomadsen, L. E. Williams, and R. Salem. Recommendations of the American Association of Physicists in Medicine on dosimetry, imaging, and quality assurance procedures for $^{90}$y microsphere brachytherapy in the treatment of hepatic malignancies. *Med. Phys.*, 38:4824–4845, 2011.

W.A. Dezarn. Quality assurance issues for the therapeutic application of radioactive microspheres. *Int. J. Radiat. Oncol. Biol. Phys.*, 71:S147–S151, 2008.

W.A. Dezarn and A.S. Kennedy. Resin $^{90}$y microsphere activity measurements for liver brachytherapy. *Med. Phys.*, 34:1896–1900, 2007.

B. Emami, J. Lyman, and A. Brown. Tolerance of normal tissue to therapeutic irradiation. *Int. J. Radiat. Oncol. Biol. Phys.*, 21:109–122, 1991.

E. M. Erbe and D. E. Day. Chemical durability of $y_2o_3$-$al_2o_3$-$sio_2$ glasses for the *in vivo* delivery of beta radiation. *J. Biomed. Mater. Res.*, 27:1301–1308, 1993.

A. K. Erdi, E. D. Yorke, M. H. Loew, Y. E. Erdi, M. Sarfaraz, and B. W. Wessels. Use of the fast hartley transform for three-dimensional dose calculation in radionuclide therapy. *Med. Phys.*, 25:2226–2233, 1998.

Y. Fong, A. M. Cohen, J. G. Fortner, W. E. Enker, A. D. Turnbull, D. G. Coit, A. M. Marrero, M. Prasad, L. H. Blumgart, and M. F. Brennan. Liver resection for colorectal metastases. *J. Clin. Oncol.*, 15:938–946, 1997.

R. A. Fox, D. Phil, P. F. Klemp, G. Egan, L. L. Mina, M. A. Burton, and B. N. Gray. Dose distribution following selective internal radiation therapy. *Int. J. Radiat. Oncol. Biol. Phys.*, 21:463–467, 1991.

V. L. Gates, A. A. H. Esmail, K. Marshall, S. Spies, and R. Salem. Internal pair production of $^{90}$y permits hepatic localization of microspheres using routine pet: proof of concept. *J. Nucl. Med.*, 52:72–76, 2011.

Gordon R. Gilmore. *Practical Gamma-ray Spectrometry.* John Wiley & Sons, Inc., West Sussex, England, second edition, 2008.

B. Gray, G. VanHazel, M. Hope, M. Burton, P. Moroz, J. Anderson, and V. Gebski. Randomised trial of sir-spheres® plus chemotherapy vs. chemotherapy alone for treating patients with liver metastases from primary large bowel cancer. *Ann. Oncol.*, 12:1711–1720, 2001.

Bruce N. Gray. Polymer base radionuclide containing particulate material, U. S. Patent Application Publication No. US 2010/0215571 A1 (26 August 2010).

C. C. Guimaraes, M. Moralles, F. F. Sene, and J. R. Martinelli. Dose-rate distribution of $^{32}$p-glass microspheres for intra-arterial brachytherapy. *Med. Phys.*, 37:532–539, 2010.

X. Guo, R. Chang, and M. A. Hussain. Ion-exchange resins as drug delivery carriers. *J. Pharm. Sci.*, 98:3886–3902, 2009.

D. P. Haughey and G. S. G. Beveridge. Structural properties of packed beds - a review. *Can. J. Chem. Eng.*, 47:130–140, 1969.

S. Ho, W.Y. Lau, T.W. Leung, M. Chan, K.W. Chan, W.Y. Lee, P.J. Johnson, and A.K.C. Li. Tumour-to-normal uptake ratio of $^{90}$y microspheres in hepatic cancer assessed with $^{99m}$tc macroaggregated albumin. *Br. J. Radiol.*, 70:823–828, 1997.

H. Houtermans, K. Scharf, and F. Reichel. International comparison of methods to test the validity of dead-time and pile-up corrections for high-precision $\gamma$-ray spectrometry. *Appl. Radiat. Isot.*, 34:487–489, 1983.

R. W. Howell, B. W. Wessels, and R. Loevinger. The mird perspective 1999. *J. Nucl. Med.*, 40:3S–10S, 1999.

H. G. Hughes. Improved logic for sampling Landau straggling in MCNP5. Memorandum LA-UR-05-4404, Los Alamos National Laboratory, Los Alamos, NM, 2005.

IAEA. Quality assurance for radioactivity measurement in nuclear medicine. Technical report, International Atomic Energy Agency Technical Report Series No. 454, 2006.

ICRU. Report 44, Tissue substitutes in radiation dosimetry and measurement. 1989. International Commission on Radiation Units and Measurements, Bethesda, MD.

ICRU. Report 72, Dosimetry of Beta Rays and Low-Energy Photons for Brachytherapy with Sealed Sources. *Journal of the International Commission on Radiation Units and Measurements*, Vol. 4(No. 2), 2004.

H. M. Jaeger and S. R. Nagel. Physics of the granular state. *Science*, 255:1523–1531, 1992.

R. Jeraj, P. J. Keall, and P. M. Ostwald. Comparisons between MCNP, EGS4 and experiment for clinical electron beams. *Phys. Med. Biol.*, 44:705–717, 1999.

P.J. Johnson. Why can't we cure primary liver cancer? *Eur. J. Cancer*, 31:1562–1564, 1995.

A.W. Katz, M. Carey-Sampson, A.G. Muhs, M.T. Milano, M.C. Schell, and P. Okunieff. Hypofractionated stereotactic body radiation therapy (sbrt) for limited hepatic metastases. *Int. J. Radiat. Oncol. Biol. Phys.*, 67:793–798, 2007.

I. Kawrakow. Accurate condensed history Monte Carlo simulation of electron transport. I. EGSnrc, the new EGS4 version. *Med. Phys.*, 27:485–498, 2000a.

I. Kawrakow. Accurate condensed history Monte Carlo simulation of electron transport. II. Application to ion chamber response simulations. *Med. Phys.*, 27:499–513, 2000b.

I. Kawrakow and D. W. O. Rogers. The EGSnrc code system: Monte Carlo simulation of electron and photon transport. Technical Report PIRS-701, National Research Council of Canada, Ottawa, Canada, 2006.

I. Kawrakow, E. Mainegra-Hing, D. W. O. Rogers, F. Tessier, and B.R.B. Walters. The EGSnrc code system: Monte Carlo simulation of electron and photon transport. Technical Report PIRS-701, National Research Council, Ottawa, Canada, 2010. URL `http://irs.inms.nrc.ca/software/egsnrc/egsnrc.html`. see http://irs.inms.nrc.ca/software/egsnrc/egsnrc.html.

Andrew Kennedy, Subir Nag, Riad Salem, Ravi Murphy, Alexander J. McEwan, Charles Nutting, Al Benson, Joseph Espat, Jose I. Bilbao, Ricky A. Sharma, James P. Thomas, and Douglas Coldwell. Recommendations for radioembolization of hepatic malignancies using yttrium-90 microsphere brachytherapy: A consensus panel report from the radioembolization brachytherapy oncology consortium. *Int. J. Radiat. Oncol. Biol. Phys.*, 68:13–23, 2007.

Andrew S. Kennedy, Clement Kleinstreuer, Christopher A. Basciano, and William A. Dezarn. Computer modeling of the yttrium-90-microsphere transport in the hepatic arterial tree to improve clinical outcomes. *Int. J. Radiat. Oncol. Biol. Phys.*, 76:631–637, 2010.

A.S. Kennedy, C. Nutting, D. Coldwell, J. Gaiser, and C. Drachenberg. Pathologic response and microdosimetry of $^{90}$y microspheres in man: review of four explanted whole livers. *Int. J. Radiat. Oncol. Biol. Phys.*, 60:1552–1563, 2004.

G. F. Knoll. *Radiation Detection and Measurement*. John Wiley & Sons, Inc., New York, third edition, 2000.

Katherine S. Kolbert, George Sgouros, Andrew M. Scott, James E. Bronstein, Rachel A. Malane, Jiaju Zhang, Hovanes Kalaigian, Stephen McNamara, Lawrence Schwartz, and Steven M. Larson. Implementation and evaluation of patient-specific three-dimensional internal dosimetry. *J. Nucl. Med.*, 38:301–308, 1997.

Markku J. Koskelo, Pertti A. Aarnio, and Jorma T. Routti. Sampo80: An accurate gamma spectrum analysis method for minicomputers. *Nucl. Instrum. Methods Phys.*, 190:89–99, 1981.

K. Kossert and H. Schrader. Activity standardization by liquid scintillation counting and half-life measurements of $^{90}$y. *Appl. Radiat. Isot.*, 60:741–749, 2004.

D. Kryeziu, M. Tschurlovits, M. Kreuziger, and F. J. Maringer. Calculation of calibration figures and volume correction factors for $^{90}$y, $^{125}$i, $^{131}$i and $^{177}$lu radionuclides base on monte-carlo ionization chamber simulation method. *Nucl. Instrum. Method Phys. Res. A*, 580:250–253, 2007.

J. Laedermann, J. Valley, S. Bulling, and F. O. Bochud. Monte Carlo calculation of the sensitivity of a commercial dose calibrator to gamma and beta radiation. *Med. Phys.*, 31: 1614–1622, 2004.

H. Langhoff and H. Hennies. Zum experimentellen nachweis von zweigquantenzerfall beim $0^+$-$0^+$-ubergang des zr$^{90}$. *Zeitschrift fur Physik*, 164:166–173, 1961.

W. Y. Lau, S. Ho, T. W. T. Leung, M. Chan, R. Ho, P. J. Johnson, and A. K. C. Li. Selective internal radiation therapy for nonresectable hepatocellular carcinoma with intraarterial infusion of $^{90}$yttrium microspheres. *Int. J. Radiat. Oncol. Biol. Phys.*, 40:583–592, 1998.

R. Lhommel, P. Goffette, M. Van den Eynde, F. Jamar, S. Pauwels, J.I. Bilbao, and S. Walrand. Yttrium-90 tof pet scan demonstrates high-resolution biodistribution after liver sirt. *Eur. J. Nucl. Med. Mol. Imaging*, 36:1696, 2009.

R. M. Lindstrom and R. F. Fleming. Dead time, pileup, and accurate gamma-ray spectrometry. *Radioactivity and Radiochemistry*, 4:20–27, 1995.

L. Liu, W. Zhang, and H. Jiang. Current treatment for liver metastases from colorectal cancer. *World J. Gastroenterol.*, 9:193–200, 2003.

J.M. Llovet and J. Bruix. Systematic review of randomized trials for unresectable hepatocellular carcinoma: Chemoembolization improves survival. *Hepatology*, 37:429–442, 2003.

N.J. Lygidakis, G. Sgourakis, G. Dedemadi, M.C. Safioleus, and J. Nestoridis. Regional chemoimmunotherapy for nonresectable metastatic liver disease of colorectal origin. *Hepatogastroenterology*, 48:1085–1087, 2001.

E. Mainegra-Hing, D. W. O. Rogers, and I. Kawrakow. Calculation of photon energy deposition kernels and electron dose point kernels in water. *Med. Phys.*, 32:685–699, 2005.

M.A. Mariscotti. A method for automatic identification of peaks in the presence of background and its application to spectrum analysis. *Nucl. Instrum. Methods Phys.*, 50: 309–320, 1967.

L. B. Marks, E. D. Yorke, A. Jackson, R. K. Ten Haken, L. S. Constine, A. Eisbruch, S. M. Bentzen, J. Nam, and J. O. Deasy. Use of normal tissue complication probability models in the clinic. *Int. J. Radiat. Oncol. Biol. Phys.*, 76:S10–S19, 2010.

MDS Nordion. Package insert therasphere® yttrium-90 glass microspheres, k120615-023 (rev. 10).

L. Mo, B. Avci, D. James, B. Simpson, W.M. Van Wyngaardt, J.T. Cessna, and C. Baldock. Development of activity standard for $^{90}$y microspheres. *Appl. Radiat. Isot.*, 63:193–199, 2005.

R. Murphy, A. Habbu, and R. Salem. Trans-arterial hepatic radioembolisation of yttrium-90 microspheres. *Biomed. Imaging Intervention J.*, 2006. **2**(3):e43.

R. J. Nickles, A. D. Roberts, J. A. Nye, A. K. Converse, T. E. Barnhart, M. A. Avila-Rodriguez, R. Sundaresan, D. W. Dick, R. J. Hammas, and B. R. Thomadsen. Assaying and pet imaging of yttrium-90: 1>>34ppm>0. *Nuclear Science Symposium Conference Record, IEEE*, 6:3412–3414, 2004.

G. Y. Onoda and E. G. Liniger. Random loose packing of uniform spheres and dilatancy onset. *Phys. Rev. Lett.*, 64:2727–2730, 1990.

A. M. Paans, R. J. Nickles, E. J. de Graaf, W. Vaalburg, S. Reiffers, A. Steenhoek, and M. G. Woldring. A dual head anger camera system for the imaging of positron-emitting radionuclides. *Int. J. Nucl. Med. Biol.*, 5:266–271, 1978.

A. Perez-Andujar and L. Pibida. Performance of cdte, hpge, and nai(tl) detectors for radioactivity measurements. *Appl. Radiat. Isot.*, 60:41–47, 2004.

M. E. Phelps. *PET: Molecular Imaging and Its Biological Applications*. Springer, New York, 2004.

Kamalesh A. Pillai, Paul E. McKeever, Conrad A. Knutsen, Patricia A. Terrio, Diane M. Prieskorn, and William D. Ensminger. Microscopic analysis of arterial microsphere distribution in rabbit liver and hepatic vx2 tumor. *Select. Cancer Ther.*, 7:39–48, 1991.

W. V. Prestwich, J. Nunes, and C. S. Kwok. Beta dose point kernels for radionuclides of potential use in radioimmunotherapy. *J. Nucl. Med.*, 30:1036–1046, 1989.

N. Reynaert, H. Palmans, and H. Thierens. Parameter dependence of the MCNP electron transport in determining dose distributions. *Med. Phys*, 29:2446–2454, 2002.

K.E. Rusthoven, B.D. Kavanagh, H. Cardenes, V.W. Stieber, S.H. Burri, S.J. Feigenberg, M.A. Chidel, T.J. Pugh, W. Franklin, M. Kane, L.E. Gaspar, and T.E. Schefter. Multi-institutional phase i/ii trial of stereotactic body radiation therapy for liver metastases. *J. Clin. Oncol.*, 27:1572–1578, 2009.

H. Ryde, P. Thieberger, and T. Alvager. Two-photon de-excitation of the 0+ level in $zr^{90}$. *Phys. Rev. Letters*, 6:475–477, 1961.

S. Agostinelli et al. Geant4 - a simulation toolkit. *Nucl. Instrum. Method Phys. Res. A*, 506:250–303, 2003.

M. Sarfaraz, A.S. Kennedy, Z.J. Cao, G.D. Sackett, C.X. Yu, M.A. Lodge, R. Murphy, B.R. Line, and D.A. Van Echo. Physical aspects of yttrium-90 microsphere therapy for nonresectable hepatic tumors. *Med. Phys*, 30:199–203, 2003.

M. Sarfaraz, A.S. Kennedy, M.A. Lodge, X. Allen Li, X. Wu, and C.X. Yu. Radiation absorbed dose distribution in a patient treated with yttrium-90 microspheres for hepatocellular carcinoma. *Med. Phys.*, 31:2449–2453, 2004.

K.T. Sato, R.J. Lewandowski, M.F. Mulcahy, B. Atassi, R.K. Ryu, V.L. Gates, A.A. Nemcek, O. Barakat, A. Benson, R. Mandal, M. Talamonti, C.O. Wong, F.H. Miller, S.B.

Newman, J.M. Shaw, K.G. Thurston, R.A. Omary, and R. Salem. Unresectable chemorefractory liver metastases: Radioembolization with $^{90}$y microspheres - safety, efficacy, and survival. *Radiology*, 247:507–515, 2008.

D. R. Schaart, J. T. M. Jansen, J. Zoetelief, and P. F. A. de Leege. A comparison of MCNP4C electron transport with ITS 3.0 and experiment at incident energies between 100 keV and 20 MeV : Influence of voxel size, substeps and energy indexing algorithm. *Phys. Med. Biol.*, 47:1459–1484, 2002.

G. D. Scott and D. M. Kilgour. The density of random close packing of spheres. *Brit. J. Appl. Phys. (J. Phys. D)*, 2:863–866, 1969.

S. M. Seltzer, P. J. Lamperti, R. Loevinger, M. G. Mitch, J. T. Weaver, and B. M. Coursey. New national air-kerma-strength standards for $^{125}$I and $^{103}$Pd brachytherapy seeds. *J. Res. Natl. Inst. Stand. Technol.*, 108:337–357, 2003.

R. Selwyn, J. Micka, L. DeWerd, R. Nickles, and B. Thomadsen. Technical note: The calibration of $^{90}$y-labeled sir-spheres® using a nondestructive spectroscopic assay. *Med. Phys.*, 35:1278–1279, 2008.

Reed Selwyn. *Image-Based Dosimetry for Selective Internal Radiation Therapy (SIRT) Using $^{90}Y$ Microspheres*. PhD thesis, University of Wisconsin - Madison, 2007.

Reed G Selwyn, Robert J Nickles, Bruce R Thomadsen, Larry A DeWerd, and John A Micka. A new internal pair production branching ratio of $^{90}$y. *Appl. Radiat. Isot.*, 65(3): 318–327, March 2007a.

R.G. Selwyn, M.A. Avila-Rodriguez, A.K. Converse, J.A. Hampel, C.J. Jaskowiak, J.C. McDermott, T.F. Warner, R.J. Nickles, and B.R. Thomadsen. $^{18}$f-labeled resin microspheres as surrogates for $^{90}$y resin microspheres used in the treatment of hepatic tumors: a radiolabeling and pet validation study. *Phys. Med. Biol.*, 52:7397–7408, 2007b.

George Sgouros, Shannon Squeri, Ase M. Ballangrud, Katherine S. Kolbert, Jerrold B. Teitcher, Katherine S. Panageas, Ronald D. Finn, Chaitanya R. Divgi, Steven M. Larson, and Andrew D. Zelenetz. Patient- specific, 3-dimentional dosimetry in non-hodgkin's lymphoma patients treated with $^{131}$i-anti-b1 antibody: assessment of tumor dose-response. *J. Nucl. Med.*, 44:260–268, 2003.

R. Sharma, G. VanHazel, B. Morgan, D. Berry, K. Blanshard, D. Price, G. Bower, J. Shannon, P. Gibbs, and W. Steward. Radioembolizatioin of liver metastases from colorectal cancer using yttrium-90 microspheres with concomitant systemic oxaliplatin, fluorouracil, and leucovorin chemotherapy. *J. Clin. Oncol.*, 25:1099–1106, 2007.

D. J. Simpkin and T. R. Mackie. Egs4 Monte Carlo determination of the beta dose kernel in water. *Med. Phys.*, 17:179–186, 1990.

Sirtex Medical. Personal communication, 2011.

Sirtex Medical. Sir-spheres® microspheres (yttrium-90 microspheres) [package insert], SSL-US-08 (November 2010).

J. Steel, A. Baum, and B. Carr. Quality of life in patients diagnosed with primary hepatocellular carcinoma: hepatic arterial infusion of cisplatin versus 90-yttrium microspheres (therasphere®). *Psycho-Oncology*, 13:73–79, 2004.

B. R. Thomadsen, H. T. Heaton II, S. K. Jani, J. P. Masten, M. E. Napolitano, Z. Ouhib, C. S. Reft, M. J. Rivard, T. T. Robin, M. Subramanian, and O. H. Suleiman. Off-label use of medical products in radiation therapy: Summary of the report of aapm task group no. 121. *Med. Phys.*, 37:2300–2311, 2010.

A.B.R. Thomson and E.A. Shaffer. *First Principles of Gastroenterology:The Basis of Disease and an Approach to Management.* The Medicine Group, Limited, Toronto, ON, 5th edition, 2005.

UWADCL. Uwadcl uncertainty summary i.3.7 document revision 3.40, Februrary 2006.

L. van Elmbt, S. Vandenberghe, S. Walrand, S. Pauwels, and F. Jamar. Comparison of yttrium-90 quantitative imaging by tof and non-tof pet in phantom of liver selective internal radiotherapy. *Phys. Med. Biol.*, 56:6759–6777, 2011.

C. Wastiel, J. Valley, A. B. Delaloye, M. Leresche, R. Linder, M. Sassowsky, and F.O. Bochud. Intercomparison of activity measurements for beta-emitters in swiss nuclear medicine laboratories. *J. Nucl. Med. Technol.*, 33:238–242, 2005.

James S. Welsh, Andrew S. Kennedy, and Bruce Thomadsen. Selective internal radiation therapy (sirt) for liver metastases secondary to colorectal adenocarcinoma. *Int. J. Radiat. Oncol. Biol. Phys.*, 66:S62–S73, 2006.

G. P. Westphal. Real-time correction of counting losses in nuclear pulse spectroscopy. *J. Radioanal. Chem.*, 70:387–410, 1982.

M. Wiernik. Normal and random pulse generators for the correction of dead-time losses in nuclear spectrometry. *Nucl. Instrum. Method*, 96:325–329, 1971.

Lawrence E. Williams, Gerald L. DeNardo, and Ruby F. Meredith. Targeted radionuclide therapy. *Med. Phys*, 35:3062–3068, 2008.

X-5 Monte Carlo Team. *MCNP — A General Monte Carlo N-Particle Transport Code, Version 5, Report LA-UR-03-1987.* Los Alamos National Laboratory, Los Alamos, NM, 2005.

H. Zaidi. Relevance of accurate monte carlo modeling in nuclear medical imaging. *Med. Phys.*, 26:574–608, 1999.

B. E. Zimmerman and J. T. Cessna. Experimental determinations of commercial 'dose calibrator' settings for nuclides used in nuclear medicine. *Appl. Radiat. Isot.*, 52:615–619, 2000.

B.E. Zimmerman, J.T. Cessna, and M.A. Millican. Experimental determination of calibration settings for plastic syringes containing solutions of $^{90}$y using commercial radionuclide calibrators. *Appl. Radiat. Isot.*, 60:511–517, 2004.